Diss. ETH No 14479

Dimuon production in e^+e^- collisions with the L3 experiment at LEP2 up to the highest energies.

A dissertation submitted to the
SWISS FEDERAL INSTITUTE OF TECHNOLOGY ZURICH

for the degree of
Doctor of Natural Sciences

presented by
Alessandro De Salvo

Dipl.–Phys. University of Rome "La Sapienza"

born January 3rd, 1971
citizen of Italy

accepted on the recommendation of

Prof. Dr. A. Rubbia,	examiner
Prof. Dr. H. Hofer,	co-examiner
Prof. Dr. C. Dionisi,	co-examiner
P.D. Dr. K. Freudenreich	co-examiner

2001

Abstract

In this thesis the results and the experimental techniques on the measurements of the interaction $e^+e^- \rightarrow \mu^+\mu^-(\gamma)$ with the L3 detector at LEP are presented, for center-of-mass energies from 189 GeV to $\sim$ 208 GeV. In this range of energy a total integrated luminosity of 608 pb^{-1} has been analyzed and 2868 muon pairs have been selected. The results on the cross section and asymmetry measurements are all in good agreement with the Standard Model expectations. The measurements from 130 GeV upwards have been also used to search for new physics, in the framework of the contact interactions theory. No evidence for new physics have been found and limits on the corresponding parameters have been set.
Presentations of the Central Error Analyzer and the muon barrel calibration techniques, other projects in which the candidate has been directly involved, are also given in the appendices.

Riassunto

In questa tesi sono presentati i risultati e le tecniche sperimentali delle misure dell'interazione $e^+e^- \rightarrow \mu^+\mu^-(\gamma)$ con il rivelatore L3 a LEP, per energie nel centro di massa da 189 GeV a $\sim$ 208 GeV. In questo range di energie sono stati analizzati $\sim$ 608 pb^{-1} di luminosità integrata e sono stati selezionati 2868 coppie di muoni. I risultati delle misure di sezioni d'urto e asimmetria sono in buon accordo con le previsioni del Modello Standard. I risultati da 130 GeV in poi sono stati utilizzati per ricercare nuova fisica, nell'ambito della teoria delle contact interactions. Nessuna evidenza di nuova fisica è stata trovata e sono stati calcolati limiti sui parametri corrispondenti.
Nelle appendici sono presentati anche il Central Error Analyzer e la calibrazione del barrel delle camere a muoni, altri progetti in cui il candidato è stato direttamente coinvolto.

Contents

List of Figures

List of Tables

Chapter 1

Introduction

Particle physics tries to describe the universe with the help of a few building blocks or *elementary particles* (leptons and quarks), and their interactions (strong, weak, electromagnetic and gravitational interactions). The strong, weak and electromagnetic interactions are well described by the Standard Model.
After the experimental discovery of the intermediate vector bosons Z and W at the SPS collider [1, 2] at CERN (European center for the Nuclear Research) in 1983, new accelerators with increasing energies have been built, with the aim to probe the structure of the matter as deeper as possible. In particular in 1989 the LEP accelerator was put into operation, together with its four experiments ALEPH [3], DELPHI [4], L3 [5] and OPAL [6].
From 1989 to 1995 LEP has operated at a centre-of-mass energy of $\sim$ 91 GeV, corresponding to the mass of the Z boson (*Z peak*), thus allowing for precise measurements of the Z boson properties, which are very important parameters of the Standard Model. Since 1995 the machine has been upgraded to reach higher energies, spanning in several steps from 130 GeV to $\sim$ 208 GeV at the very end. This has permitted a more detailed study of the Standard Model parameters far from the Z resonance and the experimental measurements on W and Z pairs, whose production thresholds are respectively at 161 GeV and 182 GeV.
In this thesis the results and the experimental techniques on the measurements of the interaction $\mathrm{e^+e^-} \rightarrow \mu^+\mu^-(\gamma)$ are presented, for center-of-mass energies from 189 GeV up to the highest LEP energies ($\sim$ 208 GeV). At first an overview of the Standard Model theory is given, with particular emphasis on the $\mathrm{e^+e^-} \rightarrow \mu^+\mu^-(\gamma)$ interaction physics. A description of the L3 experimental apparatus is then given, with particular attention to the muon spectrometer, responsible for the very precise momentum measurements of muons. Detailed studies on the detector as well as trigger efficiencies are also discussed. In the final part the results on cross sections and forward/backward asymmetry measurements are presented for 8 energy points, spanning from 189 to 208 GeV in the center-of-mass energy. The cross section and asymmetry measurements from 130 GeV upward are then used to search for new physics, within the framework of the contact interaction model.

The results presented here are in good agreement with the Standard Model predictions and no evidence for new physics have been observed.

Chapter 2

The Standard Model

The Standard Model [7] describes the electromagnetic, weak and strong interactions. The electromagnetic and weak interactions are combined together into the electroweak theory while the strong interaction are described by QCD (Quantum Chromo Dynamics).
The Standard Model is based on the symmetry groups $SU(3) \times SU(2)_L \times U(1)_Y$, describing the strong (SU(3)) and electroweak interactions ($SU(2)_L \times U(1)_Y$). This theory assumes that the matter consists of elementary fermions and that all their interactions are described by gauge theories, and they are mediated by elementary particles called *gauge bosons*.
The elementary particles are divided into three generations, each made out of two *leptons* and two *quarks* and the correspondent anti-particles. The strong interactions only affect quarks. The strong interaction gauge bosons, called *gluons*, form an SU(3) octect, while the gauge bosons of the electroweak interactions (γ, Z, $W^{\pm}$) form an isospin triplet of the SU(2) group and a U(1) singlet.
The Standard Model does not predict the particle masses.

2.1 The Electroweak theory

The Electroweak theory is based on the symmetry group $SU(2)_L \times U(1)_Y$. The $SU(2)_L$ part describes transformations in the space of the weak isospin, T, taking into account that the weak isospin current only couples to the left-handed fermions. The $U(1)_Y$ part corresponds to a rotation in the space of the weak hypercharge Y, defined by the electric charge Q and the third component of the isospin T_3:

$$Q = T_3 + \frac{Y}{2} \tag{2.1}$$

An isotriplet of vector fields (W^i_μ) couples with strength g to the weak isospin current (J^i_μ), while a single vector field (B_μ) couples with strength $g'/2$ to the weak hypercharge current (j^Y_μ). This correspond to four observable fields, two of them charged, $W^\pm_\mu = (W^1_\mu \mp W^2_\mu)/\sqrt{2}$, and two neutral which correspond to the photon, $A_\mu = B_\mu cos\theta_W + W^3_\mu sin\theta_W$, and to the Z boson, $Z_\mu = -B_\mu sin\theta_W + W^3_\mu cos\theta_W$, where θ_W is the weak mixing angle, defined as

$$tan\theta_W = \frac{g'}{g} \tag{2.2}$$

The coupling constant of fermions with charge Q_f to the photon field, by means of the electromagnetic current J^{em}_μ, is the elementary charge e:

$$eJ^{em}_\mu = e\left(J_{\mu,3} + \frac{1}{2}j^Y_\mu\right) \tag{2.3}$$

being the elementary charge e related to the coupling constants g and g' by means of the relation

$$e = g sin\theta_W = g' cos\theta_W. \tag{2.4}$$

The fermion coupling to the weak charged field has a pure V-A structure, while the coupling to the neutral field has different vector and axial-vector couplings, g_V and g_A, whose values are:

$$\begin{aligned} g^f_V &= T_{f,3} - 2Q_f sin^2\theta_W \\ g^f_A &= T_{f,3} \end{aligned} \tag{2.5}$$

The Feynman graphs for the electromagnetic, charged current and neutral current interactions are shown in figure 2.1. The respective vertex factors are shown in table 2.1.

Since in the electroweak interactions the parity is not conserved while the currents associated to the gauge fields are conserved, the fermions and the gauge bosons are introduced as massless. The fermions have independent left-handed

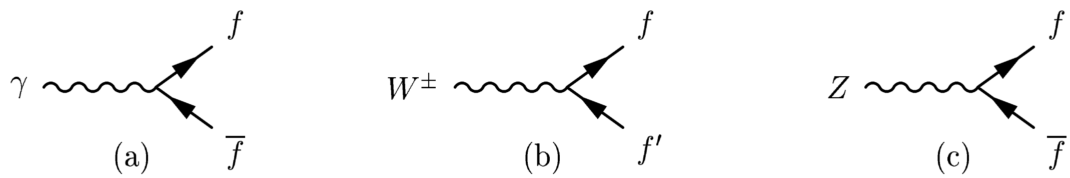

Figure 2.1: Feynman diagrams for (a) electromagnetic, (b) charged current and (c) neutral current interactions

vertex type	**vertex factor**
electromagnetic (γ)	$-ieQ_f\gamma^\mu$
charged current ($W^\pm$)	$-i\frac{g}{\sqrt{2}}\gamma^\mu\frac{1}{2}(1-\gamma^5)$
neutral current (Z)	$-i\frac{g}{cos\theta_W}\gamma^\mu\frac{1}{2}(g_V^f - g_A^f\gamma^5)$

Table 2.1: Electroweak vertex factors for Feynman diagrams

and right-handed components: the first form isospin doublets while the latter form isospin singlets, so that only the left-handed components may couple to the $W^\pm$ bosons because they have non-zero isospin. A possible way to explain the particle masses is the introduction of an isotopic doublet of scalar fields ϕ, called *Higgs doublet*

$$\phi = \begin{pmatrix} \phi^+ \\ \phi_0 \end{pmatrix}$$

together with his anti-doublet, for a total of four fields (ϕ^+, ϕ^0, ϕ^-, $\overline{\phi}^0$). Choosing a non-zero expectation value for the vacuum (*spontaneous symmetry breaking* mechanism) only the scalar part of this doublet survives, $(\phi^0 + \overline{\phi}^0)/2$, which is the physical Higgs boson H. The remaining three degrees of freedom are used to give masses to the Z and W bosons, while the photon remains massless. Fermions acquire masses through the coupling to the H boson, with strength

$$g_{Hff} = \frac{gm_f}{2M_W} \tag{2.6}$$

where m_f is a generic fermion mass and M_W is the W boson mass. The model predicts that the ratio between the W boson mass M_W and the Z boson mass M_Z is:

$$cos\theta_W = \frac{M_W}{M_Z} \tag{2.7}$$

2.2 The e$^+$e$^-$→ $\mu^+\mu^-$ process at the Born level

At the lowest level of the perturbation theory (*Born level*) the contributions to the process e$^+$e$^-$→ $\mu^+\mu^-$ are both coming from the exchange of γ and Z. The Feynman diagram for this process is shown in figure 2.2.

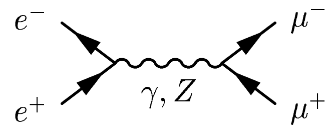

Figure 2.2: Feynman diagram for the e$^+$e$^-\rightarrow \mu^+\mu^-$process

The differential cross section, assuming $\sqrt{s} \gg m_\mu$, is then given by:

$$\frac{d\sigma}{d\Omega} = \frac{\alpha^2}{4s}\left[G_1(s)\cdot(1+cos^2\theta) + G_3(s)\cdot cos\theta\right] \tag{2.8}$$

where the G_i functions are:

$$\begin{aligned} G_1(s) &= Q_f^2 - 2g_V^e g_V^\mu Q_f \Re\chi_0(s) + (g_V^{e^2} + g_A^{e^2})(g_V^{\mu^2} + g_A^{\mu^2})|\chi_0(s)|^2 \\ G_3(s) &= -4g_A^e g_A^\mu Q_f \Re\chi_0(s) + 8g_V^e g_A^e g_V^\mu g_A^\mu |\chi_0(s)|^2 \end{aligned} \tag{2.9}$$

and the θ angle is defined as the scattering angle between the incoming electron e^- and the scattered muon μ^-.
The term $\chi_0(s)$ contains the Z mass, M_Z, and its width, Γ_Z and can be expressed as:

$$\chi_0(s) = \frac{s}{s - M_Z^2 + i\Gamma_Z M_Z} \tag{2.10}$$

The differential cross section can be also expressed as:

$$\frac{d\sigma}{d\Omega} = \frac{\alpha^2\pi}{2s}\left[I_\gamma + I_{interference} + I_Z\right] \tag{2.11}$$

where I_γ is the photon contribution, I_Z is the Z contribution and $I_{interference}$ is the $Z-\gamma$ interference term of the process. The terms have the following form:

$$\begin{aligned} &I_\gamma = Q_f^2(1+cos^2\theta) \\ &I_Z = |\chi|^2\left[g_V^{e^2} g_V^{\mu^2} g_A^{e^2} g_A^{\mu^2}(1+cos\theta) + 8g_V^e g_A^e g_V^\mu g_A^\mu cos\theta\right] \\ &I_{interference} = -Q_f^2 \Re\chi\left[2g_V^{e^2} g_V^{\mu^2}(1+cos^2\theta) + 4g_A^e g_A^\mu cos\theta\right] \\ &\chi = \tfrac{1}{4sin^2\theta_W cos^2\theta_W}\cdot\chi_0 = \tfrac{s}{4sin^2\theta_W cos^2\theta_W(s-M_Z^2+i\Gamma_Z M_Z)} \end{aligned} \tag{2.12}$$

2.2.1 Cross section

Integrating the formula 2.8 one obtains the total cross section σ_{tot}^0:

$$\sigma_{tot}^0 = \frac{4\pi\alpha^2}{3s}G_1(s) \tag{2.13}$$

For $\sqrt{s}$ close to the Z mass the photon exchange term I_γ in formula 2.11 is much smaller than the Z exchange term, I_Z, and can be neglected, as well as the interference term $I_{interference}$. Therefore we can express the total cross section for $\sqrt{s} \simeq M_Z$, assuming $\sqrt{s} \gg m_\mu$ as:

$$\sigma(\sqrt{s} \simeq M_Z) = \frac{12\pi}{M_Z^2} \cdot \frac{\Gamma_e \Gamma_\mu}{M_Z^2 \Gamma_Z^2} \tag{2.14}$$

where the Γ_l ($l = e,\ \mu$) are the lepton widths:

$$\Gamma_l = \frac{\alpha M_Z}{12 sin^2\theta_W cos^2\theta_W} \left(g_V^{l^2} + g_A^{l^2} \right) \tag{2.15}$$

2.2.2 Forward backward asymmetry

The differential cross section (equation 2.8) has a symmetric ($\propto (1 + cos^2\theta)$) and an asymmetric part ($\propto cos\theta$)

$$\frac{d\sigma}{d\Omega} = \frac{\alpha^2}{4s} \left[\underbrace{G_1(s) \cdot (1 + cos^2\theta)}_{\text{Symmetric term}} + \underbrace{G_3(s) \cdot cos\theta}_{\text{Asymmetric term}} \right]$$

The parameter that measures the deviation from a symmetric distribution is called *forward-backward charge asymmetry* and is given by:

$$A_f b(s) = \frac{\sigma_f - \sigma_b}{\sigma_f + \sigma_b} \tag{2.16}$$

with

$$\begin{aligned} \sigma_f &= 2\pi \int_0^1 \tfrac{d\sigma}{d\Omega}\ dcos\theta \\ \sigma_b &= 2\pi \int_{-1}^0 \tfrac{d\sigma}{d\Omega}\ dcos\theta \end{aligned} \tag{2.17}$$

This gives in lowest order an asymmetry of

$$A_{fb}^0 = \frac{3 \cdot G_3(s)}{8 \cdot G_1(s)} \tag{2.18}$$

For $\sqrt{s} \simeq M_Z$ one can neglect the $\gamma - Z$ interference and the photon exchange, thus considering only the Z exchange. Since the coupling of the Z boson is dominated by the axial-vector part ($g_V^{l^2} \ll g_A^{l^2}$) and taking into account the lepton universality, equation 2.18 at the Z peak reduces to

$$A_{fb}(\sqrt{s} \simeq M_Z) = 3 \cdot \frac{g_V^{l^2} g_A^{l^2}}{(g_V^{l^2} + g_A^{l^2})^2} \sim 3 \frac{g_V^{l^2}}{g_A^{l^2}} \tag{2.19}$$

Using the definition of forward-backward asymmetry from equation 2.16 the differential cross section may be expressed as

$$\frac{d\sigma}{dcos\theta} = 2\pi \frac{d\sigma}{d\Omega} = \sigma_t ot(s) \left[\frac{3}{8} \cdot (1 + cos^2\theta) + A_f b(s) \cdot cos\theta \right] \tag{2.20}$$

2.3 Corrections to the $e^+e^- \to \mu^+\mu^-$ process

For precision measurements the Born level $e^+e^- \to \mu^+\mu^-$ process must be corrected using higher order terms, in particular the important corrections are:

1. Electroweak corrections;
2. QED corrections.

2.3.1 Electroweak corrections

The processes leading to the electroweak corrections, shown in figure 2.3, are of three different types: vertex, propagator corrections and box diagrams. The corrections to the propagator include contribution from all the particles, including virtual top quarks and Higgs particle, thus depending on their masses. The box diagrams include corrections from γ, Z and W exchange and become important when the energy is above the Z peak, especially when the centre-of-mass energy is about twice the mass of the Z/W.

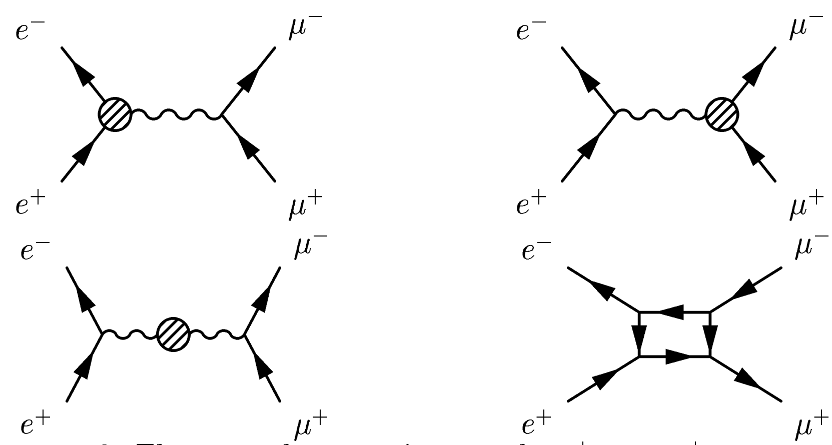

Figure 2.3: Electroweak corrections to the $e^+e^- \to \mu^+\mu^-$ process

2.3.2 QED corrections

The QED corrections to the cross section and asymmetry of the $e^+e^- \to \mu^+\mu^-$ process are much larger than the electroweak ones and are characterized by the emission of an initial or final state radiation.

Initial state radiation

The emission of an initial state radiation photon (*ISR*, see figure 2.4) reduces the centre-of-mass energy $\sqrt{s}$ at which the collision takes place.

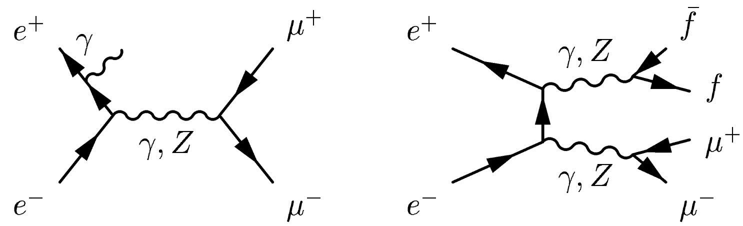

Figure 2.4: Initial state radiation diagrams for the $e^+e^- \to \mu^+\mu^-$ process

The effective centre-of-mass energy $\sqrt{s'}$, i.e. the centre-of-mass energy after the emission of the photon, is defined as the propagator energy:

$$s' = s - 2E_\gamma\sqrt{s} \tag{2.21}$$

where E_γ is the energy of the initial state radiation photon.
The QED-corrected cross section $\sigma(s)$ can be expressed by means of the Born level cross section $\sigma_B(s)$, convoluted with a radiator function $R(s,z)$, with $z = s'/s$.

$$\sigma(s) = \int_{4m_{ff}^2/s}^{1} R(z,s)\sigma_B(zs)dz \tag{2.22}$$

The radiator function $R(s,z)$ can be interpreted as the probability to radiate a fraction $x = 1 - z$ of the centre-of-mass energy, thus reducing it from $\sqrt{s}$ to $\sqrt{s'}$. The convolution with the radiator function, together with the presence of the strong Z resonance gives a double-peak structure in the effective centre-of-mass energy distribution, in which one peak corresponds to $\sqrt{s}$ and the other to the Z peak (*Z-return peak*, see figure 4.4). The variable $\sqrt{s'}$ is therefore used to define two samples:

1. **non-radiative or high energy sample:** $\sqrt{s'} > 0.85\sqrt{s}$
2. **inclusive or total sample:** $\sqrt{s'} > 75GeV$

The high energy sample does not contain radiative events and is the most interesting sample because it is the most sensitive to changes in cross section and asymmetry due to new physics phenomena. The total sample is defined enlarging the $\sqrt{s'}$ cut up to 75 GeV, thus including the radiative events; this sample has increased statistics and is important for studies of selection cuts and systematic effects.

Interference between initial and final state radiation

In the cross section and the asymmetry calculation there are two squared matrix elements of the fermion pairs representing the initial and final state radiation, as well as an interference term between them, but out of them only the initial state radiation and the interference terms are important, while the final state radiation term can be safely neglected. In the presence of the interference term the variable $\sqrt{s'}$ is no longer well defined, but since the interference contribution is small one can correct for this effect.
The corrected cross section σ_{nointf} is given by the subtraction of the interference contribution σ_{intf} from the measured cross section σ_{meas}:

$$\sigma_{nointf} = \sigma_{meas} - \sigma_{intf} \tag{2.23}$$

Assuming that the interference contribution is a function of θ and $\sqrt{s'}$ only, σ_{intf} is given by:

$$\sigma_{intf} = \int_{-1}^{1} \int_{\sqrt{s'}}^{\sqrt{s}} \frac{d^2\sigma_{intf}}{dcos\theta \; d\sqrt{s'}} \, dcos\theta \; d\sqrt{s'} \tag{2.24}$$

The cross section interference at LEP II energies is about 2% for the high energy sample and less than 0.5% for the total sample.
The asymmetry may be corrected correcting the differential cross section:

$$\frac{d\sigma_{nointf}}{dcos\theta} = \frac{d\sigma_{meas}}{dcos\theta} - \int_{z}^{1} \frac{d\sigma_{intf}}{dcos\theta \; dz} \, dz \tag{2.25}$$

Pair correction

The definition of $\sqrt{s'}$ does not distinguish between the sources of the radiation, all soft and hard photons, as well as real and virtual pair, are thus included. There exist, however, other types of diagrams, different from the initial state radiation ones, which may contribute to the creation of additional fermion pairs. In particular in figure 2.5 the first level diagrams are shown. Only the diagrams of type 2.5c are considered as initial state radiation by the theory prediction program ZFITTER [8], and only the exchange of a photon in the additional fermion pair

in taken into account in the calculation. Therefore, to have a consistent signal definition and to be able to compare measured data with theory prediction, we include in the signal definition only the conversion diagrams (2.5c).
The pair correction is applied to the inclusive sample only. In particular the low energy cut of $\sqrt{s'}$, which defines the total sample, has been placed at 75 GeV to reject most of the contribution coming from the multiperipheral diagrams (figure 2.5a) without rejecting the Z-return data, thus reducing the correction to apply to the sample.

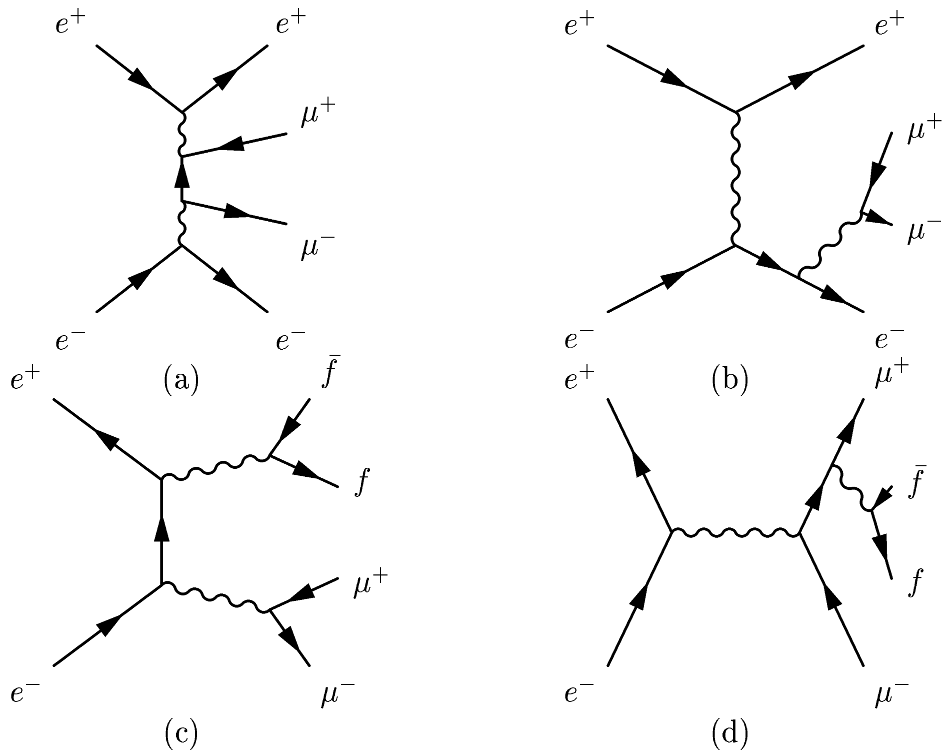

Figure 2.5: Pair correction Feynman diagrams for the $e^+e^- \rightarrow \mu^+\mu^-$ process. In the multiperipheral (a) and bremsstrahlung (b) diagrams the second pair is always an e^+e^- pair, while in the conversion (c) and annihilation (d) the second pair can be any fermion. To have a consistent signal definition only the conversion diagrams (c) are considered as signal.

2.4 New physics

Any significant deviation from the Standard Model predictions in the process $e^+e^- \to \mu^+\mu^-$ can be the evidence for new physics phenomena. One possible representation of physics beyond the Standard Model is the four-fermion contact interactions theory.

2.4.1 Contact interactions

Contact interactions are characterized by a coupling strength, g, and by an energy scale, Λ, which may be regarded as the typical mass of a new heavy particle being exchanged in the process.
For $\sqrt{s} \ll \Lambda$ new interactions can be described by the diagrams in figure 2.6, where the exchange of the virtual particle is described by an effective lagrangian $\mathcal{L}$ [9]:

$$\mathcal{L} = \sum_{i,j=L,R} \eta_{ij} \frac{g^2}{\Lambda_{ij}^2} (\bar{e}_i \gamma^\mu e_i)(\bar{\mu}_j \gamma^\mu \mu_j) \tag{2.26}$$

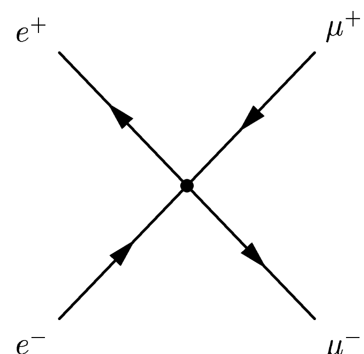

Figure 2.6: Contact interaction Feynman diagrams for the $e^+e^- \to \mu^+\mu^-$ process.

The parameter η_{ij} defines the contact interaction model by defining the helicity amplitudes contributing to the reaction and the value of g/Λ defines the size of the effect. By convention the following values are assumed:

$$g^2/4\pi = 1$$
$$|\eta_{ij}| = 1 \text{ or } |\eta_{ij}| = 0$$

The resulting differential cross section, as a function of the final-state polar angle θ, is:

$$\frac{1}{N_c}\frac{2s}{\pi\alpha^2}\frac{d\sigma}{d\ cos\theta} = \left[|A^{e\mu}_{LR}(s)|^2 + |A^{e\mu}_{RL}(s)|^2\right]\left(\frac{t}{s}\right)^2 + \left[|A^{e\mu}_{LL}(s)|^2 + |A^{e\mu}_{RR}(s)|^2\right]\left(\frac{u}{s}\right)^2 \tag{2.27}$$

where u, t, s are the Mandelstam variables, α the fine structure constant, N_c the colour factor and the helicity amplitudes A_{ij} are given by:

$$\begin{array}{ll} A^{e\mu}_{ij}(y) = Q_e Q_\mu + g^e_i g^\mu_j \chi(y) + \eta_{ij}\frac{y}{\alpha}\frac{1}{\Lambda^2} & (i \neq j) \\ A^{e\mu}_{ij}(s) = Q_e Q_\mu + g^e_i g^\mu_j \chi(s) + \eta_{ij}\frac{s}{\alpha}\frac{1}{\Lambda^2} & (i = j) \end{array} \tag{2.28}$$

$Q_{e,\mu}$ denote the electric charges of the particles, χ is the Z propagator, y is either s or t and the coupling constants g_i are defined by:

$$\begin{array}{l} g^f_L = \frac{1}{sin\theta_W cos\theta_W}(T_{3,f} - Q_f sin^2\theta_W) \\ g^f_R = \frac{1}{sin\theta_W cos\theta_W}(-Q_f sin^2\theta_W) \end{array} \tag{2.29}$$

θ_W being the weak mixing angle and T_3 the third component of the weak isospin. The differential cross section 2.27 can then be rewritten as

$$\frac{d\sigma}{d\ cos\theta} = \frac{d\sigma^{SM}}{d\ cos\theta} + c_2(s, cos\theta)\frac{1}{\Lambda^2} + c_4(s, cos\theta)\frac{1}{\Lambda^4} \tag{2.30}$$

In the formula 2.30 the constants c_i denote the deviation from the Standard Model cross section σ^{SM} and depend on the contact interaction model; in particular the term with c_2 is pure contact interaction amplitude and the term with c_4 is the interference between the Standard Model and the new physics. In table 2.2 a summary of the models considered is shown.

Model	LL	RR	LR	RL	VV	AA	V0	A0	LL-RR
η_{LL}	±1	0	0	0	±1	±1	±1	0	±1
η_{RR}	0	±1	0	0	±1	±1	±1	0	±1
η_{LR}	0	0	±1	0	±1	∓1	0	±1	0
η_{RL}	0	0	0	±1	±1	∓1	0	±1	0

Table 2.2: Contact interaction models. The helicity amplitudes A_{ij} $(i, j =$ L,R) contribution is defined by the parameter η_{ij}.

Chapter 3

The L3 detector

The L3 detector [5] (figure 3.1) has been designed to study the e^+e^- interactions up to 200 GeV in the center-of-mass and it has been used successfully up to 208 GeV during the last year of data taking. It has been built to measure with particular accuracy muons, electrons, photons and jets.
The detector is placed inside a solenoidal magnet of 16 m(H)x14 m(L) and 7800 tons of weight which provides a 0.51 T magnetic field along the beam axis (z-axis). The choice of a big magnet has been driven by the idea to measure with high accuracy the muon momentum, whose resolution increases quadratically with respect to the track length and linearly to the magnetic field. For this reason it has been chosen to build a bigger standard magnet instead of a smaller superconducting one, which would have been more powerful but very expensive.
On both sides of the experiment two magnetic doors returning the flux of the solenoidal field are placed. Coils are wrapped around the doors giving a toroidal field of 1.2 T.
The magnets and the forward muon spectrometer are anchored to the ground while the rest of the detector is placed onto a stainless steel support tube of 32 m length and of 4.45 m diameter, coaxial to the LEP tube. The support tube may be moved by the operators in the LEP control room to adjust the optics of the beam.
The axis reference frame conventionally used has the z-axis in the same direction as the electrons, the x-axis pointing to the LEP ring center and the y-axis pointing up to complete the right-handed set. A cylindrical coordinate reference system is also used, having the z-axis like above, such that θ is the polar and ϕ the azimuthal angle.

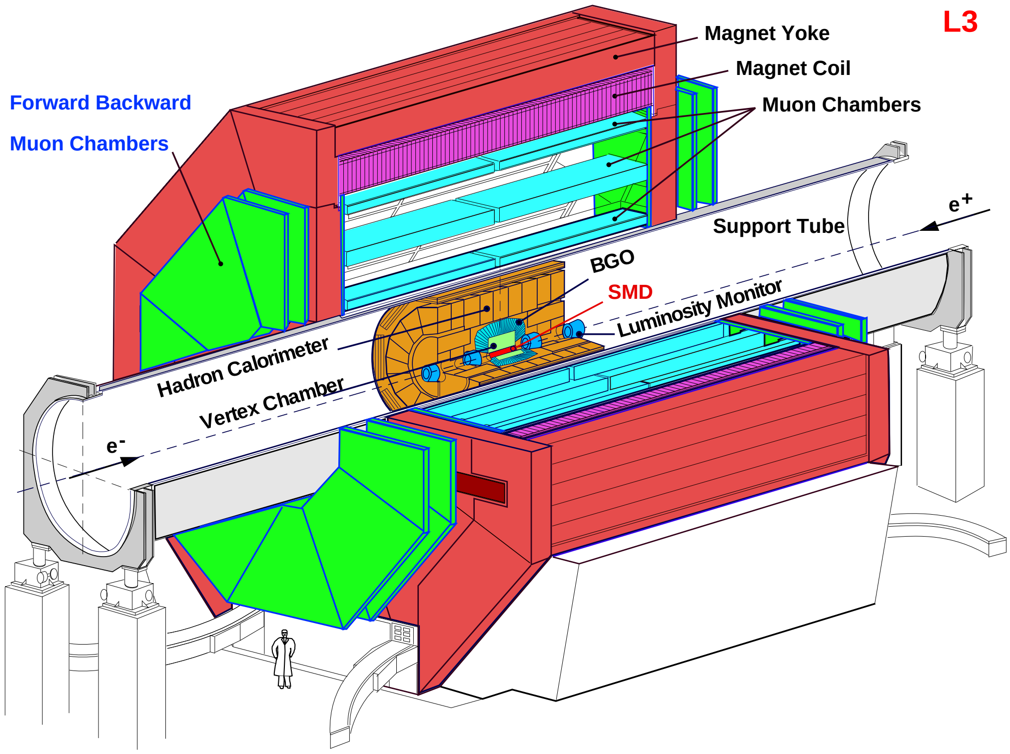

Figure 3.1: The L3 detector, perspective view.

The L3 detector is build up of 7 main subdetectors:

1. *micro vertex detector;*
2. *central tracking chamber;*
3. *electromagnetic calorimeter;*
4. *scintillation counters;*
5. *hadronic calorimeter;*
6. *muon spectrometer;*
7. *luminosity monitor.*

Furthermore, close to the beam pipe on both ends of the experiment, there is a very small angle tagger (VSAT) and a lead ring covered with plastic scintillators (ALR), used by the trigger system.

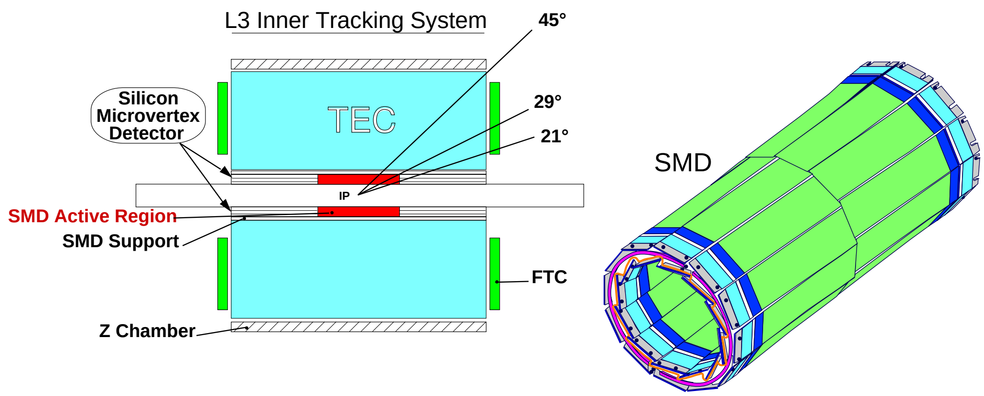

Figure 3.2: The L3 Silicon Microvertex Detector (**SMD**) and the central track detector (**TEC**).

3.1 Micro vertex detector

The *Silicon Microvertex Detector* [10] (**SMD**, figure 3.2) has been built to measure with high precision charged tracks very close to the primary interaction vertex and to identify secondary vertices.
The detector is mounted directly on the outside of the beam pipe and has a cylindrical structure made out of carbon fiber, on top of which two layers of *n-type*, double sided silicon modules (*strips*) are mounted on. Each module has a length of 70 mm, a width of 40 mm and a thickness of 300 μm.
The detector is placed along the beam axis and its material corresponds to 1.2 radiation lengths. The angular coverage is 360° in ϕ and between 21° and 159° in θ.
Using the high resolution strips it is possible to measure the charged tracks position up to 7 μm in ϕ and 14 μm in θ.

3.2 Central tracking chamber

The central tracking chamber [11] is made out of two coaxial drift chambers, with an inner radius of 9 cm, an outer radius of 45 cm, a length of 106.8 cm and a maximum lever arm of 31.7 cm in the radial direction. The angular coverage of the detector is 360° in ϕ and between 25° and 175° in θ. To achieve a single wire resolution of about 50 μm, given the small dimensions of the detector, the chamber works in a time-expansion mode, from which the name *Time Expansion CHamber* (**TECH**). In this mode (figure 3.3) the charges produced by a transversing particle are collected in a wide area with high electric potential and low drift velocity (6 $\mu m/ns$), separated from the narrow amplification zone close to the anode wires, by means of a grid at ground. potential. In the narrow zone the signal is amplified and the necessary measurement precision is reached determining the center-of-gravity of the charged distribution as function of time. The gas used is a mixture of 80% of CO_2 and 20% of C_4H_{10} at a pressure of 1.2 atm.

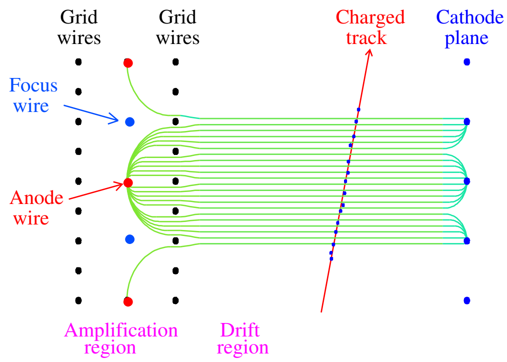

Figure 3.3: Working scheme of a time expansion system.

The detector is divided in two parts, called *inner TEC* and *outer TEC*. The inner TEC is split in 12 sectors with 8 anode wires each, while the outer has 24 sectors with 54 anode wires each. The outer sectors are placed such that two of them cover one inner sector, to solve the ambiguities in the position determination originating from the two halves of each sector. All wires (figure 3.4) are placed parallel to the beam axis and are used for measurements in the r-ϕ plane.

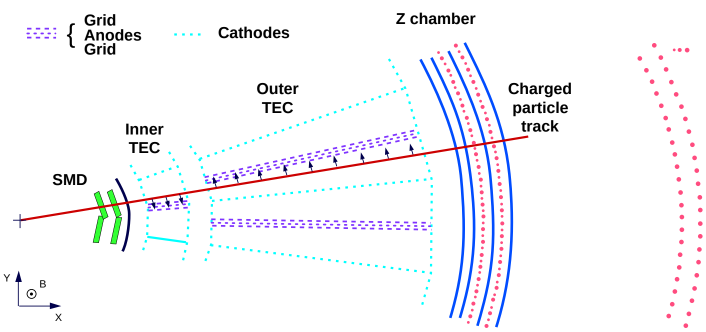

Figure 3.4: Schematic view of the TEC wire position. The cathods are manteined at ~ -8 kV, the anodes at $\sim +3$ kV and the grid at 0.

To measure the z coordinate, two layers of proportional chambers, called *Z chambers* (figure 3.5), are placed on the outer part of the detector. They are made out of four cathode strip planes each, for a total of 920 strips, with an inclination of 69°, 90°, −69° and −90°. Each chamber has a length of 106.8 cm and a thickness of 2.15 cm. In addition, 9 special impedance anode wires of the outer TEC are read from both sides to measure the z coordinate.

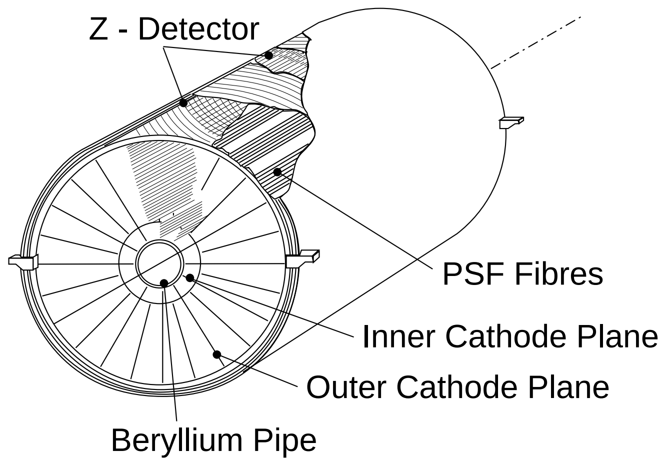

Figure 3.5: Schematic view of TEC and Z chambers.

In the low angle regions there are the *Forward Tracking Chambers* (**FTC**), used for monitoring purposes. The FTCs consist of two layers of 4.5 cm thick drift tubes, one placed orthogonally to the beam axis and one perpendicularly with respect to the other.
The TEC resolution on the measurement of the *Distance of Closest Approach* (**DCA**) is 57.7 μm. Combined with the position determination coming from the SMD a resolution on the transverse momentum $1/p_\perp$ of 0.0147 GeV^{-1} is achieved.

3.3 Electromagnetic calorimeter

The Electromagnetic CALorimeter (**ECAL**) has been build to measure with high resolution electrons and photons at energies between 100 MeV and 100 GeV.
Since the space available was limited and the detector was to be resistant to the radiation, but also non-hygroscopic and very sensible to very low energies *BGO* crystals (*Bismuth Germanium Oxide crystals*, $Bi_4Ge_3O_{12}$) have been chosen. Such crystals have a radiation length of 1.12 cm, an absorption length for hadronic particles of 22 cm, a Moliére radius of 2.3 cm, a good intrinsic resolution

and are not hygroscopic. Moreover the high gain of BGO crystals makes it possible to avoid the use of photomultipliers, in favour of less magnetically sensible photodiodes.
The detector structure, shown in figure 3.6, is 24 cm thick and is able to contain almost totally electromagnetic showers up to 50 GeV. The central part of the detector (barrel) covers the angular region $42.3° < \theta < 137.7°$. Two endcaps, on both sides, are placed in the regions $5.0° < \theta < 42.3°$ and $137.7° < \theta < 185.07°$. The coverage in ϕ is 360° for both the barrel and the endcaps, giving an overall solid angle coverage of more than 90%.

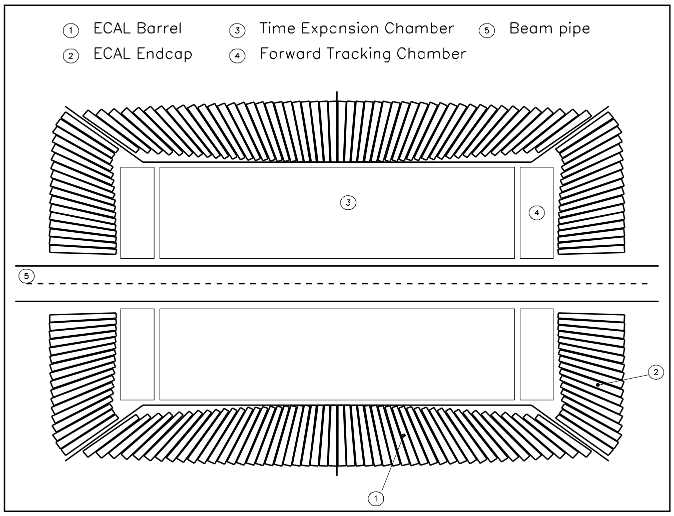

Figure 3.6: Schematic side view of the L3 ECAL detector.

The ECAL barrel is made out of two half cylinders, each made out of a matrix of 160 crystals in ϕ and 24 in θ, yielding a total of 7680 crystals. The endcaps are made out of 1536 crystals each. Each crystal (figure 3.7) is 24 cm long and has a pyramidal section with a base of 3 cm $\times$ 3 cm, on which a photodiode, used to collect the produced light, is attached. Each crystal covers an angle of about 2° from the interaction point.
All the crystals are mounted on a carbon fiber support with cell walls of 0.2 mm, to reduce the amount of the inactive material of the detector to 1.75%.

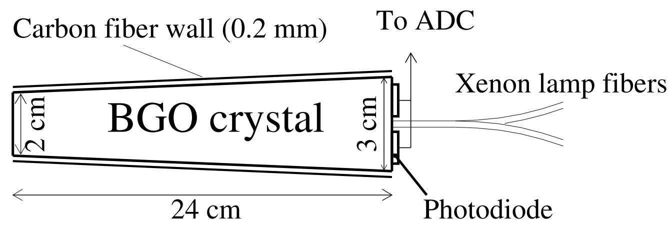

Figure 3.7: Schematic view of a BGO crystal.

The resolution on the impact point is less than 2 mm for energies greater than 4 GeV and the energy resolution ranges from 5% at E=100 MeV to 1.4% at E=45 GeV.

3.4 Scintillation counters

Outside of the electromagnetic calorimeter there is a set of plastic scintillators. They measure the time between the e^+e^-interaction and the moment the particles hit the counters, providing a way to distinguish between muons originating from a e^+e^-interaction and cosmic muons.
In the barrel region there are 30 counters covering the angular region where $|cos\theta| < 0.83$ while in ϕ the coverage is about 93%, given the fact that at $\phi \sim 185.6°$ and $\phi \sim 354.4°$ the correspondent counters are not present to permit the passage of the connection cables. The time resolution for the barrel counters is 0.8 ns.
In the small polar angle region two sets of 16 plastic scintillators are installed, one per side (*MASTER side*, in the direction of the electrons, and *SLAVE side*, in the other direction). The time resolution for the endcap counters is 1.9 ns.

3.5 Hadronic calorimeter

The hadronic calorimeter [12] has been designed to measure with high precision the energy of the hadrons coming from the e^+e^-interactions and to identify the direction of hadronic jets.
The detector (figure 3.8) is a *sampling* detector made out of depleted uranium, used as absorber, and multiwire proportional chambers to measure the deposited

energy. It covers the angular range of $5.5° < \theta < 174.5°$.

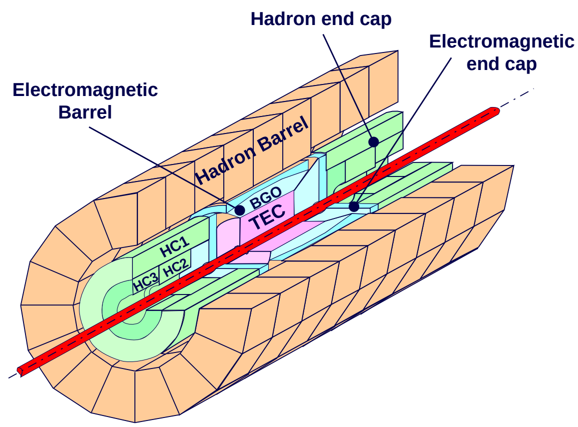

Figure 3.8: Perspective view of L3 hadronic calorimeter.

The barrel consists of 9 modules (*rings*), each made out of 16 modules. To allow the passage of the TEC and ECAL signal cables to the external electronics, the 3 outermost rings have been built shorter. Each long module is made out of 60 layers of proportional chambers, while each short module has 53. Each module is made out of proportional chambers, alternating with chambers oriented in the z and in the ϕ direction. 5 mm uranium layers are placed between the chamber planes, except for the layers closest to the electromagnetic calorimeter, in which the uranium is replaced by stainless steel.
The endcaps consist of three independent rings: one external (*HC1*) and two internal (*HC2* and *HC3*). Each of them is vertically divided in two sections to ease their removal during detector maintenance periods. As for the barrel these modules are made out of multiwire proportional chambers alternating with uranium absorbers.
The detector material represents about eight absorption length and thus is able to contain most of the particles subject to strong interaction. The angular resolution is of the order of $0.5°$ and the angular deflection, caused by multiple scattering, has an RMS of $0.2°$. On the outside of the hadronic calorimeter a layer of brass absorber plates, interleaved with proportional tubes, called *muon filter*, is installed. It is used to track the muons before they reach the muon spectrometer and to reduce the punch-through. The detector is directly anchored to the support tube.

3.6 Muon spectrometer

The muon spectrometer (figure 3.9) is used to detect muons with energy greater than 2 GeV, passing through the inner detector, measuring with high precision their momenta. It is build up of two components:

1. the central region or **barrel** ($44° < \theta < 136°$);
2. the small angle region or **forward/backward** [13] ($\theta > 136°$ and $\theta < 44°$).

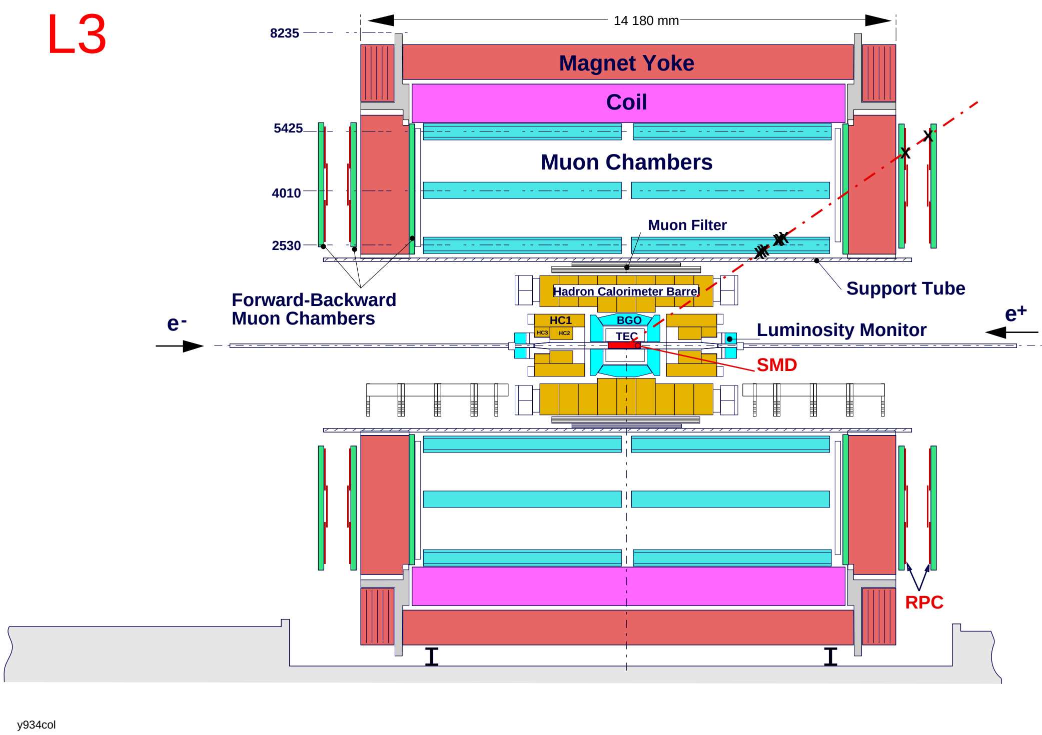

Figure 3.9: Schematic side view of the L3 muon system.

3.6.1 The barrel muon chambers

The barrel (figure 3.10) covers the angular region $44° < \theta < 136°$ and is placed inside the solenoidal magnet of 0.51 T, whose flux is returned via the two magnetic doors placed at both ends. It has been designed to measure the deviation of the muons along the trajectory in the r-ϕ projection with a resolution of $\Delta p/p \simeq 2.5\%$ at 50 GeV, using the big lever arm ($B \times l^2 = 5.9\ T \times m^2$).

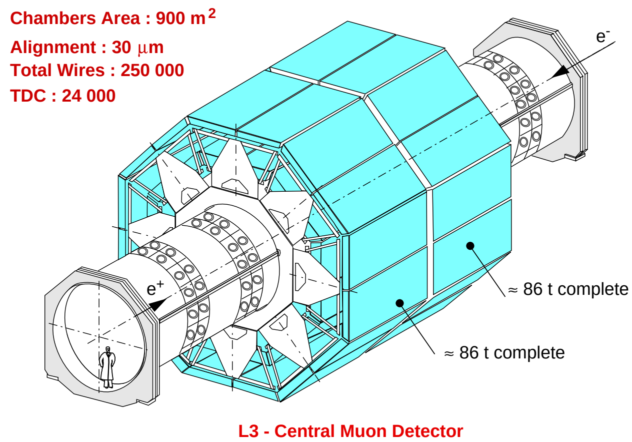

Figure 3.10: Perspective view of the L3 muon barrel.

The detector has an octagonal section, divided in two independent wheels (master side: $44° < \theta < 90°$, slave side: $90° < \theta < 136°$). Each side of the octagonal wheels is called octant and is made out of three layers of drift chambers with the wires oriented in the $r-\phi$ projection (*p-chambers*), i.e. parallel to the beam axis, and four layers of drift chambers with the wires oriented in the z projection (*z-chambers*), i.e. perpendicular to the beam axis.
The three p-chambers (figure 3.11) are called MI, MM and MO. The innermost chamber (MI) is made out of one layer of drift chambers divided into 19 electrostatically independent cells of 16 wires each; the medium chamber (MM) and the outermost chamber (MO) are both made out of two adjacent layers of drift chambers and divided into 30 (MM) and 44 (MO) cells, 101.5 mm wide. Each MM cell (figure 3.11) has 24 anode wires, while the MO and MI cells contain 16 wires each. Between two adjacent anodes there are wires used to modify the electrical field close to the anodes, called *field* wires. The cathode plane is made out of wires called *mesh wires*. The single wire resolution of the p-chambers is $\simeq 220\mu m$.
The hits of the wires within one cell or two adjacent cells are combined to segments. Tracks with segments in all the three p-chambers are called *triplets*, while tracks with segments in two chambers only are referred to as *doublets*.
The z-chambers are placed above and below the MI and MO chambers, two per side. They are build up of 109 mm drift cells, displaced by half a cell, one from each other, to solve the left-right ambiguity. In each cell there is an anode sense wire and a I-shaped aluminium profile which works as cathode. Such chambers have a single wire resolution of 500 μm but taking advantage of the cell displacement it is possible to measure the z coordinate with a precision of 200 μm.
To minimize the multiple scattering the MM layer has been built in aluminium with an honeycomb structure and it has no z-chambers.

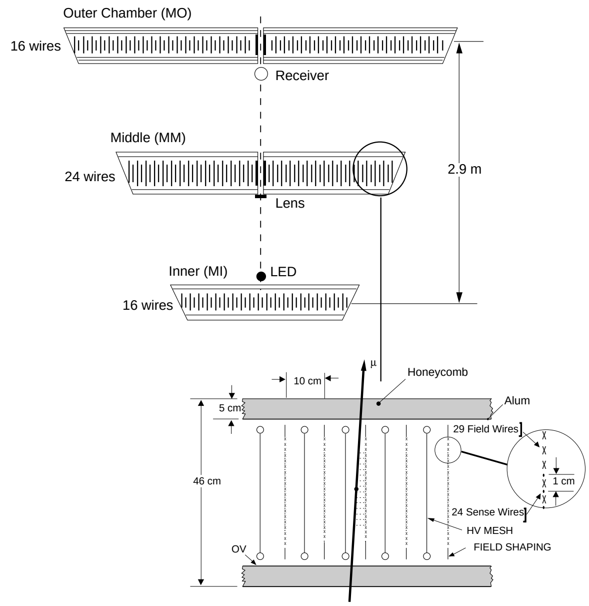

Figure 3.11: Muon barrel p-chambers structure.

The bending of the muon trajectory in the barrel, caused by the solenoidal magnet, is used to calculate the transverse momentum $p_\perp$ of the muon:

$$p_\perp = \frac{Bl^2}{8S} \tag{3.1}$$

where l is the lever arm, B the magnetic field and S the deviation or *sagitta*. The latter is the deviation of the trajectory from a straight line, measured from the coordinates of the track in the three layers of the p-chambers (figure 3.12):

$$S = \frac{S_1 + S_3}{2} + S_2 \tag{3.2}$$

where S_1, S_2 and S_3 are defined as in figure 3.12.

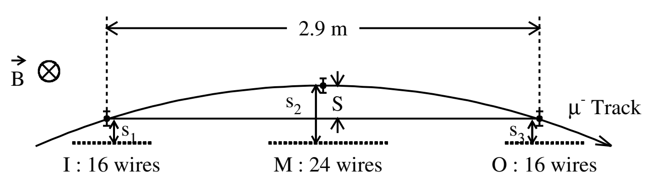

Figure 3.12: Sagitta measurement principle.

Since the contribution of the term S_2 (MM chamber) to the sagitta measurement is higher than for the other terms, it has been chosen to improve the position mesaurement resolution in that layer. This has been done increasing the number of wires in the MM layer with respect to MI and MO, since the position measurement resolution, ϵ is proportional to $1/\sqrt{n_{MM}}$, where n_{MM} is the number of wires in a cell. In case only two points are available, the trajectory can be measured from the slope of the p-segments but the momentum resolution worsens from 2.5% to 21.3%.

3.6.2 The forward/backward muon chambers

The forward/backward muon chambers (figure 3.13) consist of three layers of drift chambers and two RPCs (*Resistive Plate Chambers*) per side, divided into 16 modules in ϕ. The innermost layer (FI chamber) is placed inside the magnet, while the middle (FM chamber) and outer chambers (FO chamber) are outside, at a relative distance of 80 cm to each other. Since the space available between the barrel and the magnetic door was very limited, the chamber structure has been made out of aluminium, yielding to a total thickness of 18.2 cm per chamber.

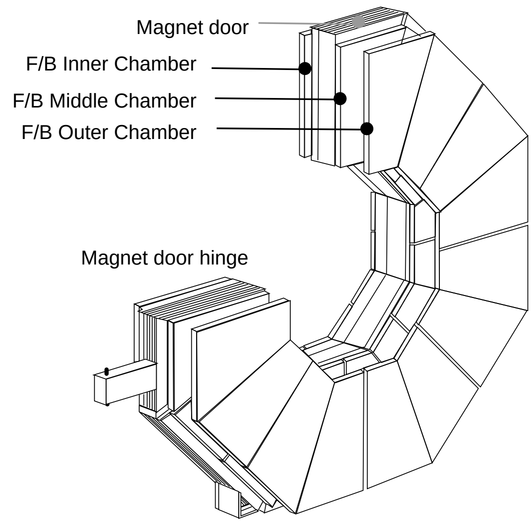

Figure 3.13: Perspective view of the forward muon drift chambers.

Each chamber is made out of three layers (X, Y and W, see figure 3.14). The X and W layers are used to measure the r-ϕ coordinate and contain respectively 18 and 19 cells of 8 wires each, displaced by half a cell to solve the left-right ambiguity. The Y layer contains 27 cells of 4 wires each and is used to measure the polar angle.

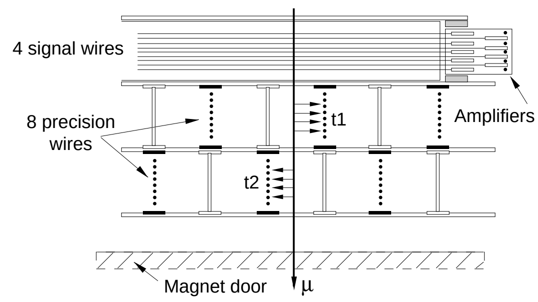

Figure 3.14: Schematic view of the forward muon drift chambers cells.

Between the FM and the FO chambers two layers of double gap RPCs are placed, reducing the gap between FM and FO to 46 cm. Each RPC is made out of three modules of different sizes (small, medium and large). Each module has 96 aluminium strips disposed orthogonally to the beam axis to measure the polar angle. The RPC system is mainly used by the trigger system.
The whole system consists of two complementary regions (figure 3.15): the *S-region* ($36° < \theta < 44°$) and the *T-region* ($24° < \theta < 36°$). In the S-region muons are analyzed by measuring the bending of the solenoidal magnet with the barrel chambers MI, MM and the forward chamber FI. The momentum resolution achievable ranges from 4% to 23%, depending on the polar angle. In the T-region the muon momentum is measured using the deflection of the 1.2 T toroidal magnet on the magnetic doors, which bends the trajectory in θ. Here the momentum resolution is limited by the multiple scattering in the magnetic doors to about 30%.

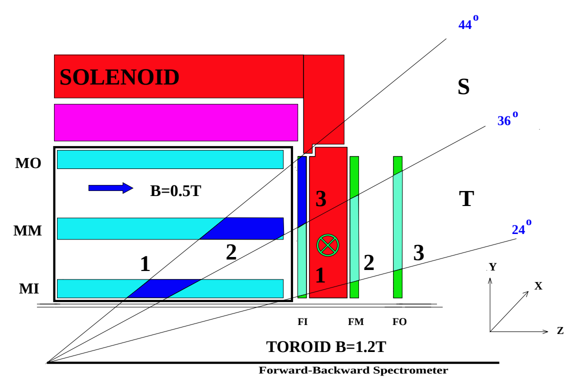

Figure 3.15: Forward/backward muon system side view with S and T region description.

3.6.3 The aligment system

Inside each barrel chamber the wires are supported by three precision ladders, two at the end and one in the middle (see figure 3.16), made out of Pyrex glass pieces. The two ladders at the ends are positioned with respect to an external reference in such a way that only movements in the x directions are allowed. The middle layer is equipped with precision actuators which permit movements in the x and y directions.

Three calibrated RASNIK straightness monitors are also mounted on the three

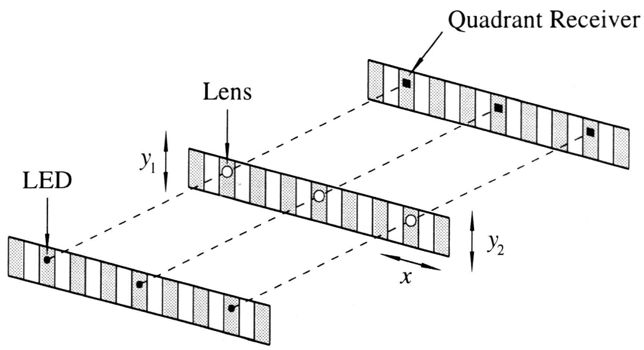

Figure 3.16: Schematic view of the ladders which support the wires in the muon barrel. The straightness monitor (LEDs, lenses and photodiodes) is also shown.

ladders. Each system consists of a LED, a lens and a 4-quadrant photodiode (*receiver*), as shown in figure 3.16. The light emitted by the LED is imaged by the lens onto the receiver, making possible a measurement of the displacement of the middle layer. During the data taking the position of the middle layer is continuously monitored and the information is written on the database. This information is then used by the offline reconstruction program to correct the wire position with an accuracy of $\sim 10\ \mu m$ in x and $40\ \mu m$ in y.

The barrel chambers in a single octant are aligned by using an opto-mechanical system. In figure 3.17 a schematic view of the system is shown. A LED is positioned in the middle of each end frame of the MI chamber,while at each end of the MM and MO chambers a gauge block holds respectively a lens and a photodiode. The light emitted by the LED is focused to the photodiode through the lens, permitting a precise measurement of the displacement of the MM layer with respect to the others. With this method the mechanical alignment is measured with an accuracy of $\sim 30\ \mu m$.

The forward/backward alignment system is shown in figure 3.18). Precise sensors (*proximity sensors*) are attached directly onto the surface of the inner forward chamber, FI. They are used to measure the distance between the forward/backward system and a reference surface, anchored to the muon barrel system. The proximity sensors allow the measurement of the alignment up to an

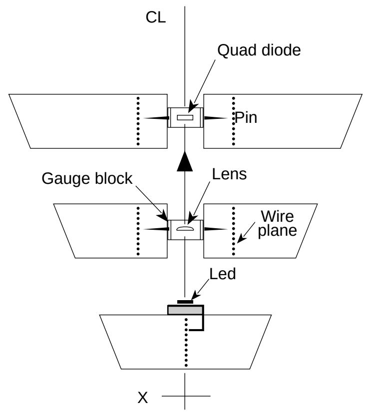

Figure 3.17: Schematic view of the opto-mechanical alignment system in the muon barrel.

accuracy of $\sim 70\ \mu m$ in x, $\sim 150\ \mu m$ in y and $\sim 580\ \mu m$ in z. The FI, FM and FO chambers are then aligned one respect to each other by means of a RASNIK system (*FBRASNIK*), which allows a measurement of the displacements up to a resolution of $\sim 50\ \mu m$ in x and y and $\sim 2000\ \mu m$ in z.

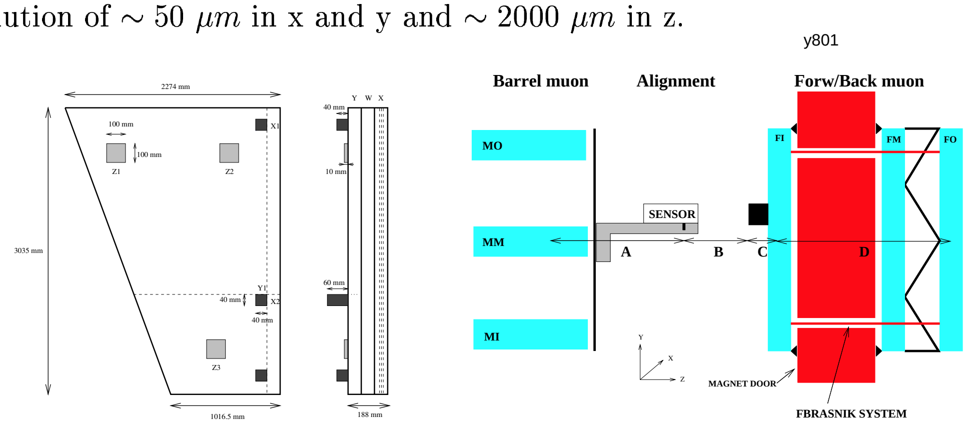

Figure 3.18: Schematic view of the forward/backward muon chambers alignment system. Proximity sensors, attached to the FI chamber (a), are used to measure the distance of the forward/backward system from the barrel, while RASNIK systems (b) allows the measurement of the relative alignment among the forward chambers FI, FM and FO.

3.7 Luminosity monitor

The luminosity monitor (figure 3.19) has been built to count the $e^+e^- \rightarrow e^+e^-(\gamma)$ events in the very small angle region.
The detector consists of two electromagnetic calorimeters and two silicon detectors (*SLUM*), located symmetrically at z=±2.7 m from the interaction point. The electromagnetic calorimeters are made out of a cylindrical matrix of 403 BGO crystals, with an inner radius of 68.2 mm and an outer radius of 191.4 mm. The angular resolution is 0.4 mrad in θ and 0.5 mrad in ϕ.

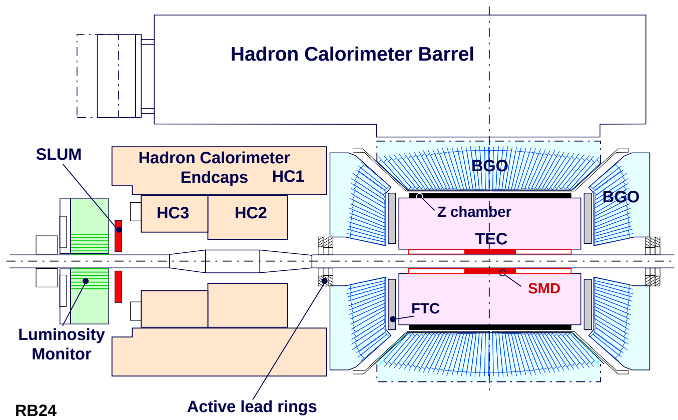

Figure 3.19: Schematic view of L3 luminosity monitor.

3.8 Trigger system

After each bunch crossing the trigger system has the task to decide if an event is interesting from a physics point of view and must be accepted. Since a beam crossing takes place each 22 μs, the trigger must decide in a very small amount of time, in order not to introduce dead time in the acquisition system. The trigger may reduce the incoming event data rate from the beam crossing rate ($\sim$ 45 kHz) up to $\sim 2-3$ Hz: this is important in order to reduce the dead time resulting from the detector readout and data writing on disk.
The system is made out of three separated levels, with increasing complexity.

3.8.1 The level-1 trigger

It is an hardware trigger, with access to coarse data coming from the various subdetectors. It is made out of five different subtriggers:

1. **TEC trigger**: the TEC trigger selects events with at least two tracks in the TEC and has a rate of $\sim 1-4$ Hz.
2. **Energy trigger**: it selects events with energy deposits in the calorimeters. It contributes to the overall rate with $\sim 1-2$ Hz.
3. **Scintillator trigger**: it is used to select high multiplicity events and to reject cosmic muons. The typical rate is ~ 0.1 Hz.
4. **Muon trigger**: the muon trigger selects events with at least one muon in the muon chambers. This trigger requires also that a scintillator counter has its time in a window of 30 ns around the beam crossing time, to reject cosmic muons. The muon trigger rate is $\sim 1-2$ Hz.
5. **Luminosity trigger**: the luminosity trigger has been built to select bhabha events in the luminosity monitors. Its rate is ~ 1.5 Hz.

The overall decision is the logical OR of all the subtrigger decisions. The output rate from the level-1 is of the order of 10-15 Hz.

3.8.2 The level-2 trigger

In case of a positive decision of the level-1 trigger the event is passed to the level-2 [14]. The level-2 is a software trigger, based on a Sun cluster, which has access to the coarse data stream from the detector. Since it has more time to decide on the event it may preform a more accurate analysis, applying rather sophisticated algorithms.
It has been built to reduce the noise and to reject beam-gas and beam-wall interactions. The output rate of the level-2 trigger is about 10 Hz.

3.8.3 The level-3 trigger

The level-3 [15] is the only trigger that has access to the fully digitized data, and therefore it is the only one that can take advantage of the finest granularity and high resolution data, as in the offline analysis. It is software-based, running on two alpha-VAX workstations, and uses sophisticated algorithms, very similar to the ones used in the offline reconstruction. The output rate of the level-3 trigger is of the order of 2-3 Hz.

3.9 Data reconstruction

The raw data are reconstructed by means of the reconstruction program (*REL3*). The drift times, the energy deposits in the calorimeters and the scintillation counter times are extracted from the digital signals recorded from the detector, using calibration constants. The TEC drift times are converted to position measurement to reconstruct the tracks. Adjacent energy deposits in the calorimeters are grouped together to form clusters, representing the energy losses of the observed particles. Finally the full tracks are recontructed using the informations coming from all the different subdetectors.

3.10 Detector simulation

The detector response is simulated using Monte Carlo techniques, according to the prediction of the Standard Model. The particle interactions with the detector materials are simulated using GEANT3 [16]. The simulation includes the detector acceptance, efficiency and time-dependant conditions, like detector failures. The differences between the simulated events and the experimental data are used to estimate systematic errors.

Chapter 4

Event selection

A muon passing through the detector produces signals in almost all of the sub-detectors, in particular:

1. hits in the SMD;
2. up to 8 hits in the inner TEC and up to 54 hits in the outer TEC (depending on the polar angle θ);
3. a peak energy deposit of $\sim 250MeV$ in the electromagnetic calorimeter (*Minimum Ionizing Particle*, MIP);
4. a peak energy deposit of $\sim 2GeV$ in the hadron calorimeter (*Minimum Ionizing Particle*, MIP);
5. one hit in the scintillation couters;
6. hits in the muon spectrometer, usually hitting three layers in the region $|cos\theta| < 0.8$ and four layers in the region $0.8 < |cos\theta| < 0.9$.

Putting together these informations it is then possible to identify a muon in the apparatus.

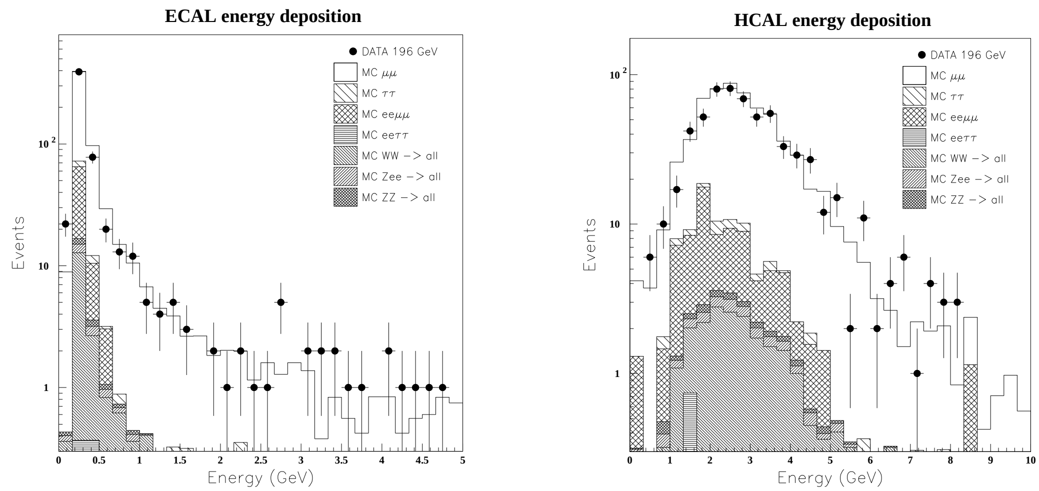

(a) (b)

Figure 4.1: Energies deposited by a muon in the electromagnetic (a) and hadron (b) calorimeter. In the plots only the events with two muons reconstructed by the muon chambers are included.

4.1 Muon identification

A muon can be identified using the muon spectrometer and/or the combination of the tracker and the calorimeters of the L3 experiment.
In the muon spectrometer a muon can be identified only if at least two track segments are found and matched in two different layers of chambers. Using these information it is then possible to measure the directions and momentum of incoming muons.
The muon spectrometer extends up to $|cos\theta| < 0.9$ and has a gap at about 90°, which represents $\sim 7\%$ of the solid angle, reducing the efficiency to $\sim 98\%$ due to geometry. This adds to the fact that $\sim 9\%$ of the events are not detected by the spectrometer whithin the fiducial volume, due to the presence of the support structure and to the inefficiency of the detector. To recover these effects it is possible to use the identified tracks in the central tracking chamber.
In addition, a muon can be identified as a *Minimum Ionizing Particle* in the calorimeters. In this case a TEC track is required and single muon segments in the muon chambers, if present, are also used. A MIP is seen as an isolated cluster in the calorimeters and is said to be a muon if the energy depositions around a cone of 12° with respect to the direction of the TEC track is $E_{ECAL} < 2\ GeV$ in the electromagnetic calorimeter and $E_{HCAL} < 7\ GeV$ in the hadronic calorimeter (see figure 4.1).

The identified muons can thus be divided in two different categories:

1. **MM sample**: two reconstructed muons in the muon chambers ($\sim$ 85% of the total identified muons);

2. **MX sample**: one recontructed muon in the muon chambers and a MIP ($\sim$ 15%).

The category in which two MIPs are reconstructed is not taken into account because is negligible.
The fiducial volume in the analysis has been restricted to the region in which the muon spectrometer is present ($|cos\theta| < 0.9$). In figure 4.2 the $cos\theta$ and ϕ distributions for the sample at a center-of-mass energy of 196 GeV are shown.

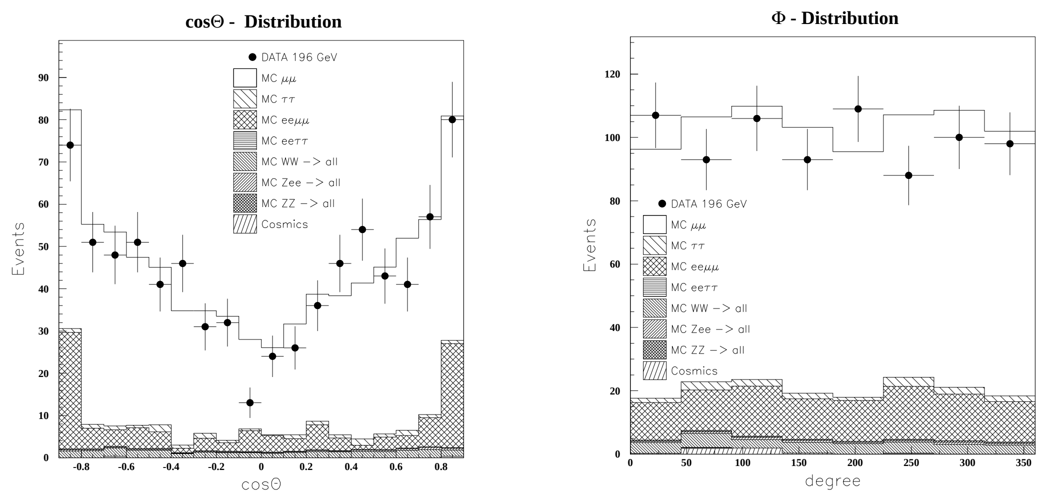

(a) (b)

Figure 4.2: Angular distributions for a center-of-mass energy of 196 GeV. The $cos\theta$ (a) and ϕ (b) distributions are shown.

4.2 Muon pair selection

Not all identified muons are coming from the process $e^+e^- \to \mu^+\mu^-(\gamma)$ because other processes with muons in the final state can contribute as background. For center-of-mass energies above the Z peak the most offending background processes are (see also figure 4.3):

1. $e^+e^- \to \tau^+\tau^-(\gamma)$;
2. $e^+e^- \to e^+e^-\mu^+\mu^-(\gamma)$;
3. $e^+e^- \to W^+W^-(\gamma)$;
4. $e^+e^- \to Ze^+e^-(\gamma)$;
5. $e^+e^- \to ZZ(\gamma)$;
6. $e^+e^- \to e^+e^-\tau^+\tau^-(\gamma)$;
7. cosmic muons;

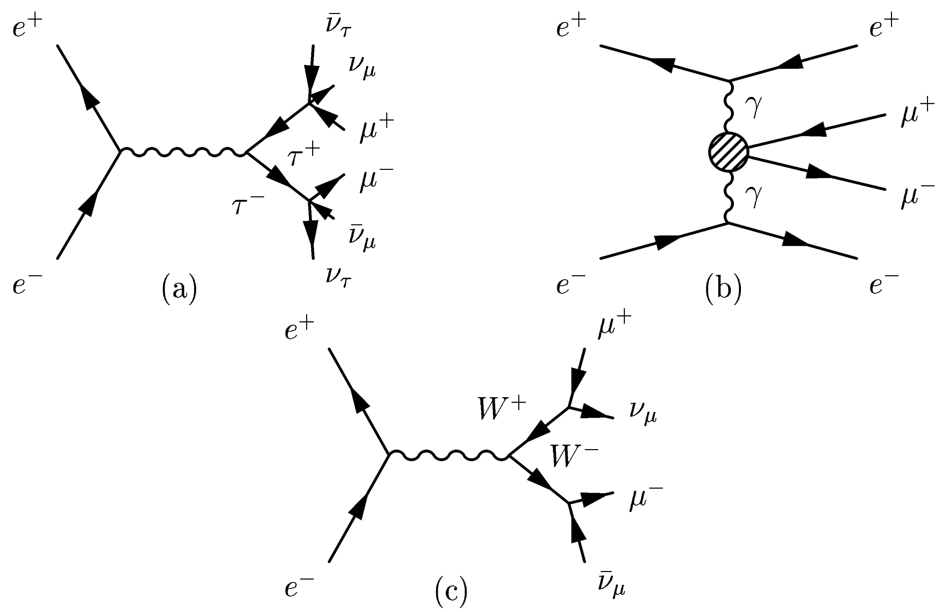

Figure 4.3: Feynman diagrams for the main background contributions to the $e^+e^- \to \mu^+\mu^-(\gamma)$ process. The $e^+e^- \to \tau^+\tau^-(\gamma)$ [a], $e^+e^- \to e^+e^-\mu^+\mu^-(\gamma)$ [b] and $e^+e^- \to W^+W^-(\gamma)$ [c] processes are shown.

As shown later most of the background has been removed applying cuts on suitable measured quantities of the identified muons. The remaining percentage of

background after all the cuts, estimated by using Monte Carlo simulations, represents $\sim 19\%$ of the selected sample.
A summary of such quantities, with the corresponding cut values and the affected background, is given in table 4.1.

Quantity	**Cut**	**Background**
Acollinearity	$\xi < 90°$	All background
Momentum of the most energetic muon	$P_{max}/E_{beam} > 0.4$	All background
Cluster multiplicity	number of clusters < 12	$e^+e^- \rightarrow W^+W^-(\gamma)$
$r - \phi$ DCA	one $d_\perp < 1\ mm$	Cosmic muons
z DCA	one $d_\| < 25\ mm$	Cosmic muons
Scintillator times	one $t_scin < 3.5\ ns$	Cosmic muons

Table 4.1: Di-muon selection cuts and their associated background

4.2.1 Effective center-of-mass energy reconstruction

The electrons and positrons may radiate an initial state radiation photon, thus reducing the effective center-of-mass energy (see chapter 2.3.2). The effective center-of mass energy $\sqrt{s'}$ is reconstructed using the momenta of the muons and the energy of the radiated photons, if detected.
The procedure is done in the following way:

1. if one or more photons with an angular separation to the closest muon of more than 20° and with energies greater than 15 GeV are detected, they are assumed to be originated by an initial state radiation: in this case the $\sqrt{s'}$ is calculated by using the formula

$$s' = s - 2E_\gamma\sqrt{s} \tag{4.1}$$

   where E_γ and P_γ are respectively the sum of the energies and of the momenta of the emitted photons;

2. if no photons with energies greater than 15 GeV are detected it is assumed that a single ISR photon has been emitted along the beam pipe, thus going undetected: in this case the energy of the γ_{ISR} is calculated using the angles θ_1 and θ_2 of the muons with respect to the beam pipe and imposing energy and momentum conservation:

$$E_\gamma = \sqrt{s}\,\frac{|sin(\theta_1 + \theta_2)|}{sin\theta_1 + sin\theta_2 + |sin(\theta_1 + \theta_2)|} \tag{4.2}$$

   the $\sqrt{s'}$ is then calculated using formula 4.1.

In figure 4.4 the $\sqrt{s'}$ distributions for center-of-mass energies in the range $189 - 205\ GeV$ are shown.
Using the variable $\sqrt{s'}$ we define two event samples (see chapter 2.3.2):

1. **high energy sample:** $\sqrt{s'} > 0.85\sqrt{s}$
2. **inclusive or total sample:** $\sqrt{s'} > 75GeV$

The high energy sample represents $\approx 45\%$ of the total sample. The inclusive sample contains the Z-return events too, as shown in figure 4.4.

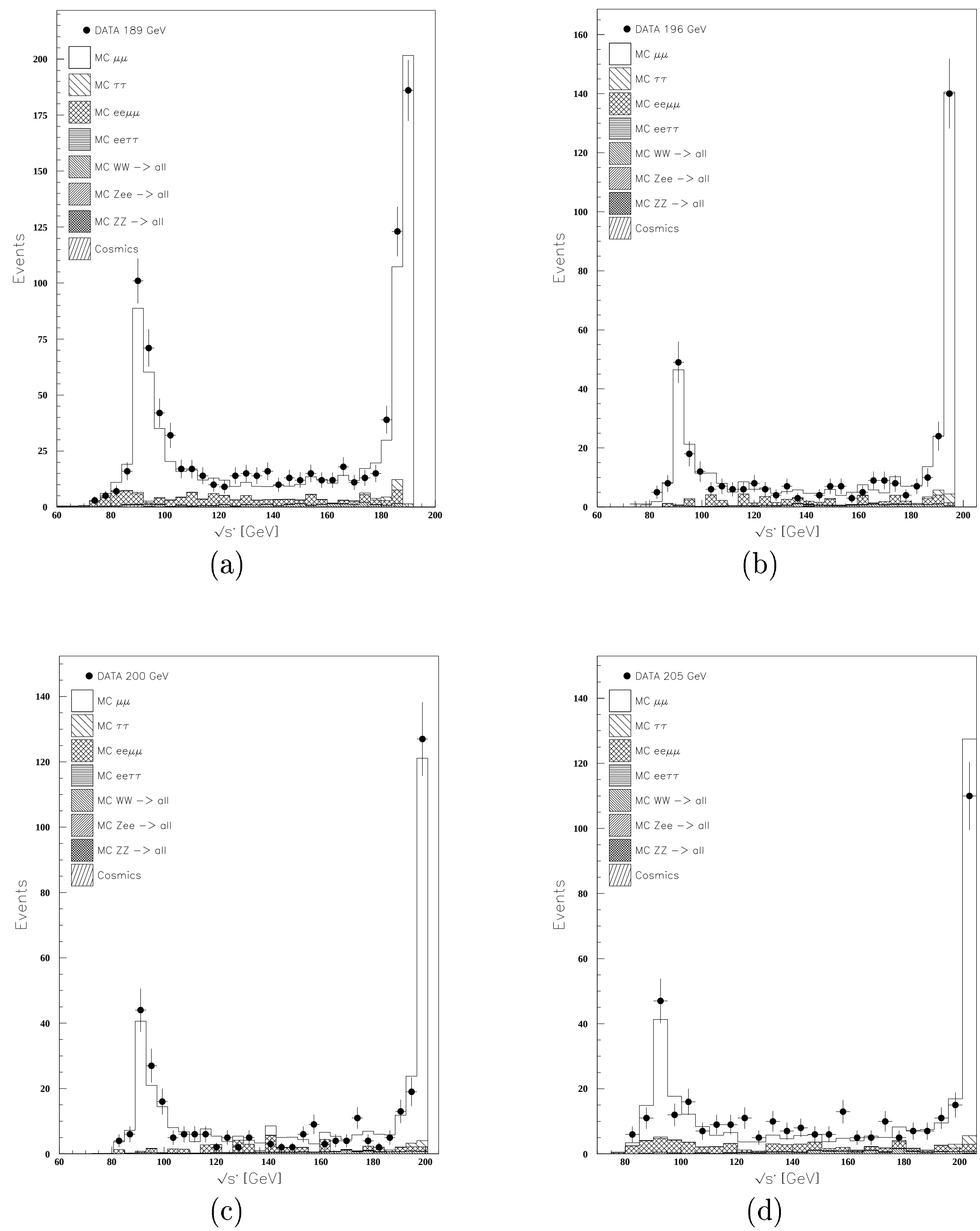

Figure 4.4: $\sqrt{s'}$ distributions for data taken at center-of-mass energies of 189 GeV (a), 196 GeV (b), 200 GeV (c) and 205 GeV (d). The peak at ~ 90 GeV in the distributions is given by the Z-return effect, in which a muon, radiating an ISR, reduces the effective center-of-mass energy to $\approx m_Z$.

4.2.2 Background rejection

In the following paragraphs the different selection cuts for background rejection are explained. The corresponding plots show the data and Monte Carlo distributions of the given variable, where all the cuts are applied but the one in discussion (*n-1 plots*).

Muon momentum cut

Muons coming from the background processes $e^+e^- \rightarrow \tau^+\tau^-(\gamma)$, $e^+e^- \rightarrow e^+e^-\mu^+\mu^-(\gamma)$, and $e^+e^- \rightarrow e^+e^-\tau^+\tau^-(\gamma)$ are expected to have lower momenta with respect to the muons coming from $e^+e^- \rightarrow \mu^+\mu^-(\gamma)$. This is due to the fact that in the process $e^+e^- \rightarrow \tau^+\tau^-(\gamma)$a large fraction of the energy is carried away by the neutrinos, thus undetected, while in the two-photon processes most of the energy is carried away by the e^+e^- pair production

To reject most of the background coming from these processes a cut on the most energetic muon momentum is applied, requiring that $P_{max}/E_{beam} > 0.4$, where P_{max} is the momentum of the most energetic muon and E_{beam} is the beam energy. In figure 4.5 the P_{max}/E_{beam} distributions for the inclusive sample and for the non-radiative sample are shown.

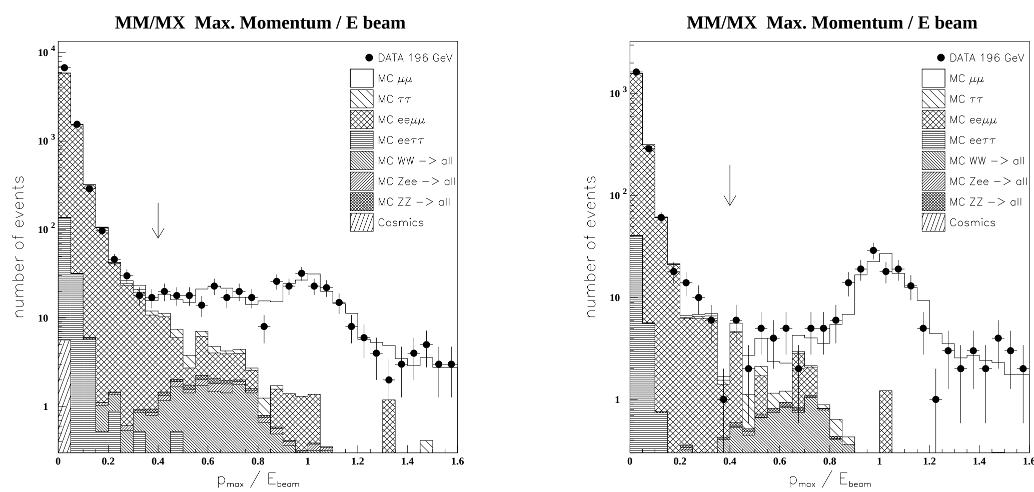

(a) (b)

Figure 4.5: P_{max}/E_{beam} distributions for the inclusive (a) and non-radiative (b) samples. The cut is placed at $P_{max}/E_{beam} > 0.4$ and it is indicated by the arrow. The cut has been placed in that region to insure high acceptance for events with hard ISR photons while being not too close to the region where the background raise is too fast, to avoid too big systematic errors.

The momentum cut has been placed in a conservative way to insure high acceptance for events with hard ISR photons.

Acollinearity cut

To reject additional two-photon background an acollinearity cut is applied, requiring that $\xi_{MM,MX} < 90°$. The acollinearity is defined to be 0 for a perfect back-to-back muonpair.

In figure 4.6 the acollinearity plots for the MM and MX samples for both inclusive and non-radiative samples are shown.

The cut has been placed at 90° to be sure to include all the events with radiative return to the Z peak.

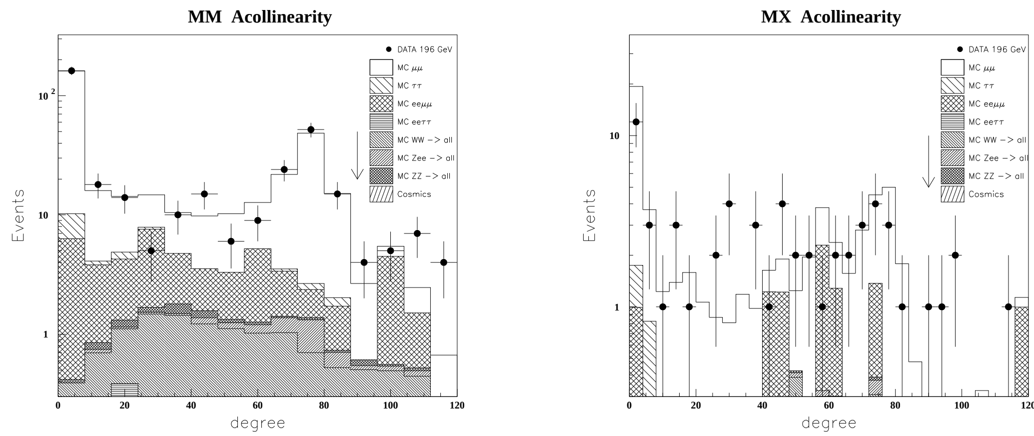

(a) (b)

Figure 4.6: Acollinearity plots for the Muon-Muon (a) and Muon-MIP (b) categories. The cut is placed at 90° to be sure to include all the events with radiative return to the Z peak.

Cluster multiplicity cut

The background rejection can be enhanced by cutting on the number of reconstructed clusters in the calorimeters (multiplicity cut). This cut is important for all the processes in which at least one of the particle can decay hadronically, in particular $e^+e^- \rightarrow W^+W^-(\gamma)$, $e^+e^- \rightarrow ZZ(\gamma)$ and $e^+e^- \rightarrow \tau^+\tau^-(\gamma)$. The requirements for the selection is to have a number of reconstructed clusters less than 12 (see figure 4.7).

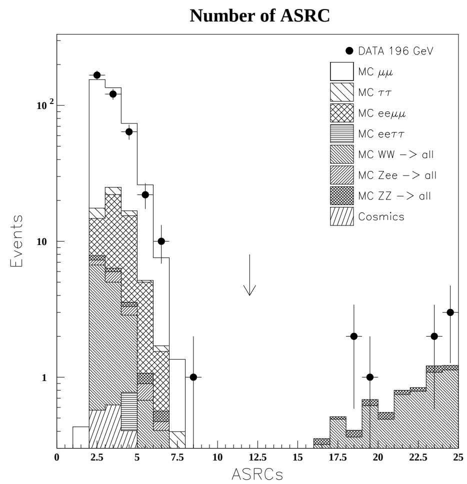

Figure 4.7: Number of clusters in the calorimeters (ASRCs) for events with two muons in the final state. The maximum number of allowed clusters for the selection is 12, thus rejecting the background processes decaying hadronically.

4.2.3 Cosmic muons rejection

Cosmic muons may be selected as normal muon pairs. They have a constant distribution in time and space and are uncorrelated with the beam crossing interactions. To reject such events two cuts are applied:

1. **Spatial cuts (DCA)**: at least one muon is required to have a distance of closest approach to the interaction vertex $d_{\perp} < 1\ mm$ in the $r-\phi$ projection and $d_{||} < 25\ mm$ in the z plane.

2. **Time cuts (scintillators)**: at least one muon is required to have one geometrically correspondent scintillator hit in a window of 3.5 ns around the beam crossing time. In addition, when two muons have two opposite scintillators in time, the difference between their times $t_{up} - t_{down}$ is calculated, together with the expected time-of-flight of the cosmic muon from one scintillator to the other, t_{cosm}, from the geometrical position of the hit counters. For two perfectly back-to-back counters t_{cosm} is $\sim 6\ ns$. If the difference $t_{up} - t_{down}$ and t_{cosm} agree within 2 ns the muon is tagged as cosmic and thus rejected ($t_{up} - t_{down} + t_{cosm} < 2\ ns$, see figure 4.10).

The DCA plots are shown in figure 4.8, while the minimum scintillator time plots are shown in figure 4.9. In both plots the tails represent the constant rate of cosmics.
Starting from the 205 GeV data onwards, the noise in the forward scintillation counters had increased. Therefore it had been decided to remove the cut on the forward scintillator times in the region $0.8 < |cos\theta| < 0.9$, applying instead more stringent cuts on the DCA ($d_\perp < 0.7\ mm$ in the $r-\phi$ projection and $d_{||} < 15\ mm$). As a Monte Carlo substitute for the cosmic muons, a control sample from the data has been built, selecting the events with an $r-\phi$ DCA in the range $5\ mm < d_\perp < 50\ mm$ and a minimum scintillator time in the range $5\ ns < |t_{scin}| < 50\ ns$. This control sample will is used instead of simulated data in all plots, except for the DCA and scintillator ones.

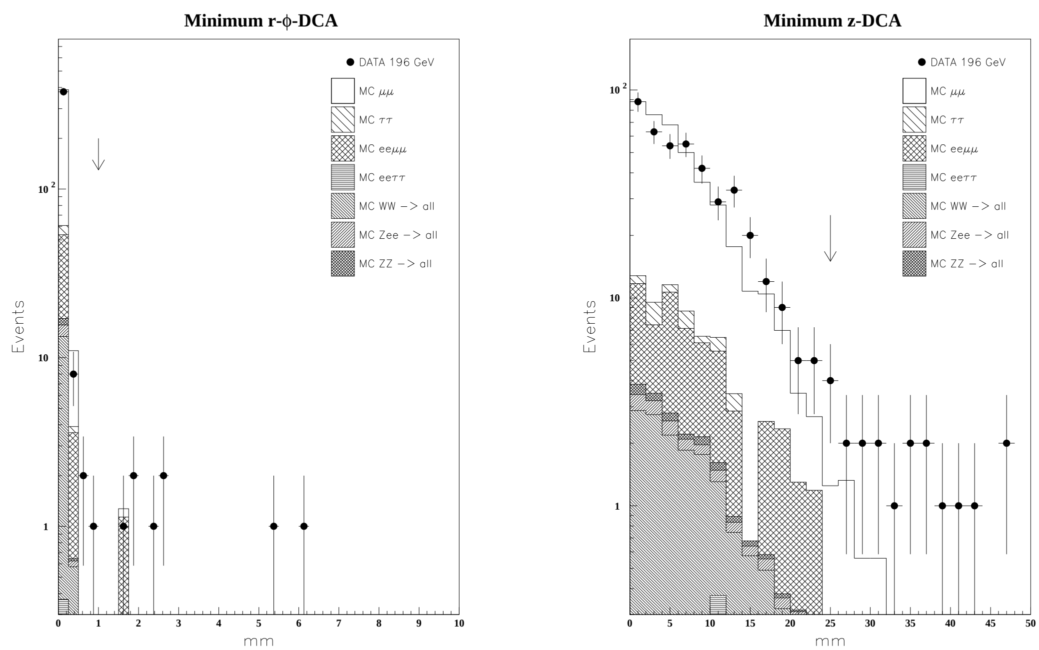

(a) (b)

Figure 4.8: Minimum Distance of Closest Approach distributions in the $r-\phi$ (a) and $r-z$ (b) projection. The visible tail on the right of the plots in the constant cosmic muon rate. In these plots it is required that $d_\perp < 1\ mm$ and $d_{||} < 25\ mm$ in the region where $|cos\theta| < 0.8$; in the remaining region, $0.8 < |cos\theta| < 0.9$, it is instead required that $d_\perp < 0.7\ mm$ and $d_{||} < 15\ mm$.

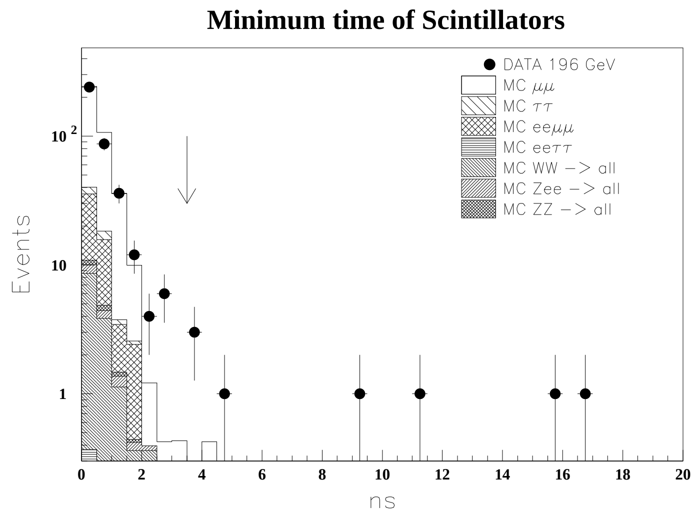

Figure 4.9: Minimum scintillator counter times distribution. In this plot only the scintillation counters in the angular region $|cos\theta| < 0.8$ are shown. The right tail of the plot is due to the constant cosmic muon rate.

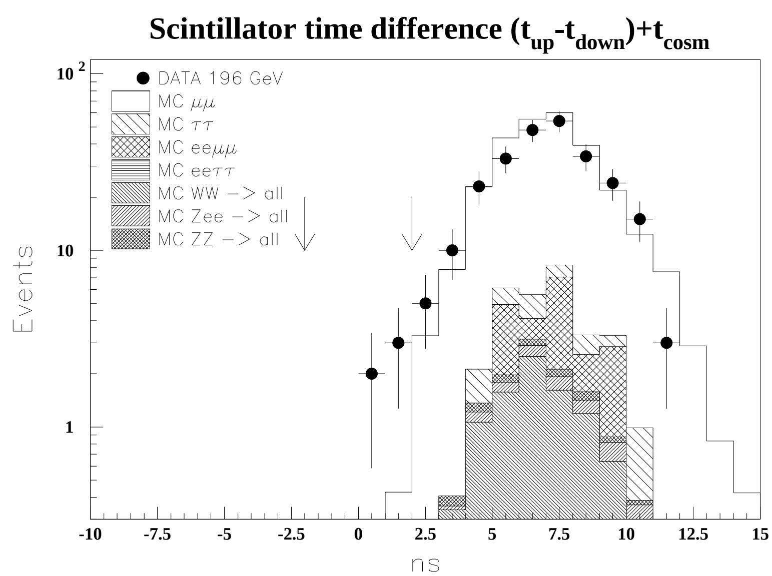

Figure 4.10: Difference between the upper and lower scintillator times added to the cosmic expected time-of-flight $(t_{up} - t_{down}) + t_{cosm}$. If $(t_{up} - t_{down})$ and t_{cosm} agree withing 2 ns the event is tagged as cosmic muon and rejected.

Chapter 5

Efficiencies

The detector and trigger efficiencies are central quantities in any experimental analysis. A correct reproduction of the behaviour of the whole apparatus, via a real-detector simulation which takes into account detector inefficiencies, allows this together with an accurate study of the systematic uncertainties.
In this chapter the efficiencies of the various parts of the L3 detector which are used for the dimuon analysis are calculated and compared to the Monte Carlo simulation. In particular the muon chamber efficiencies, the scintillation counters, RPC, MIP reconstruction, and central tracking chamber efficiencies will be treated in detail. A study of the trigger efficiencies will also be presented.

5.1 Muon chamber efficiencies

All selected events must have at least one track reconstructed in the muon spectrometer. Therefore, the correct simulation of the muon chamber behaviour is critical for the dimuon selection.
Possible inefficiencies may come from cells which were disconnected from the HV system during the data taking period. This effect is taken into account in the Monte Carlo simulation, using the HV values recorded in the online muon database, in which these events are recorded all along the data taking period.
A muon passing through the spectrometer ideally hits three planes of P-chambers (triplets). If a cell in a P-layer is inefficient the muon may be identified anyway by means of the other two layers (doublet), but if another cell is inefficient the track is not reconstructed. In this case the muon may be identified as a MIP (see section 5.3).
The muon chamber efficiencies have been calculated using a subsample of selected events, independent from the muon chambers, where two MIPs have been reconstructed and TEC trigger is required. From the angles of the muon identified as a MIP, the cells that should have been hit by the muon are identified, taking into account the geometry of the detector: if no segments are reconstructed in

one or more layers the interested cells are identified by means of the ϕ angle and considered as inefficient. In figure 5.1 the average efficiencies of all the octants of the muon chamber P-layers, with their statistical errors, are shown for the master ($z > 0$) and slave ($z < 0$) sides. For the two outermost P-layers (MM and MO) the separation in ϕ of the two half octants is clearly visible. The efficiencies, calculated separately for the 1998, 1999 and 2000 data taking periods, are in good agreement with the Monte Carlo simulation.

The overall acceptance, ϵ, is calculated from the number of reconstructed segments, N_{rec}, and the number of missing segments that should have been reconstructed, according to geometry, N_{miss}.

$$\epsilon = \frac{N_{rec}}{N_{rec} + N_{miss}} \tag{5.1}$$

Since only reconstructed segments are in the control sample, ϵ includes the muon chambers reconstruction efficiency too. The acceptance calculation is performed separately for all the muon chambers layers and the single efficiencies are listed in table 5.1, comparing them to the Monte Carlo simulation. All P-layers have an efficiency above 90% and a good agreement between data and simulation is observed. The efficiency of the Z-chambers is higher in the simulation than in the real data but this does not affect the analysis. In fact the Z-chambers are used to determine the θ angle of the muon track with high precision, but in case of inefficiency the polar angle still may be obtained from the inner detector. The discrepancies in the efficiency of the forward/backward layers between data and Monte Carlo are small enough to have a negligible effect on the selection.
All efficiencies have been stable during the three years of data taking and they have been of the same order like in previous years, showing that no apparent aging of the apparatus was present.
To check the correct simulation of the forward/backward muon chambers the number segments reconstructed in each single layer of FI, FM and FO (*occupancy*) has been computed, both for the master and the slave side. The results are shown in figure 5.2 for the year 1999. A good agreement between data and Monte Carlo is observed.

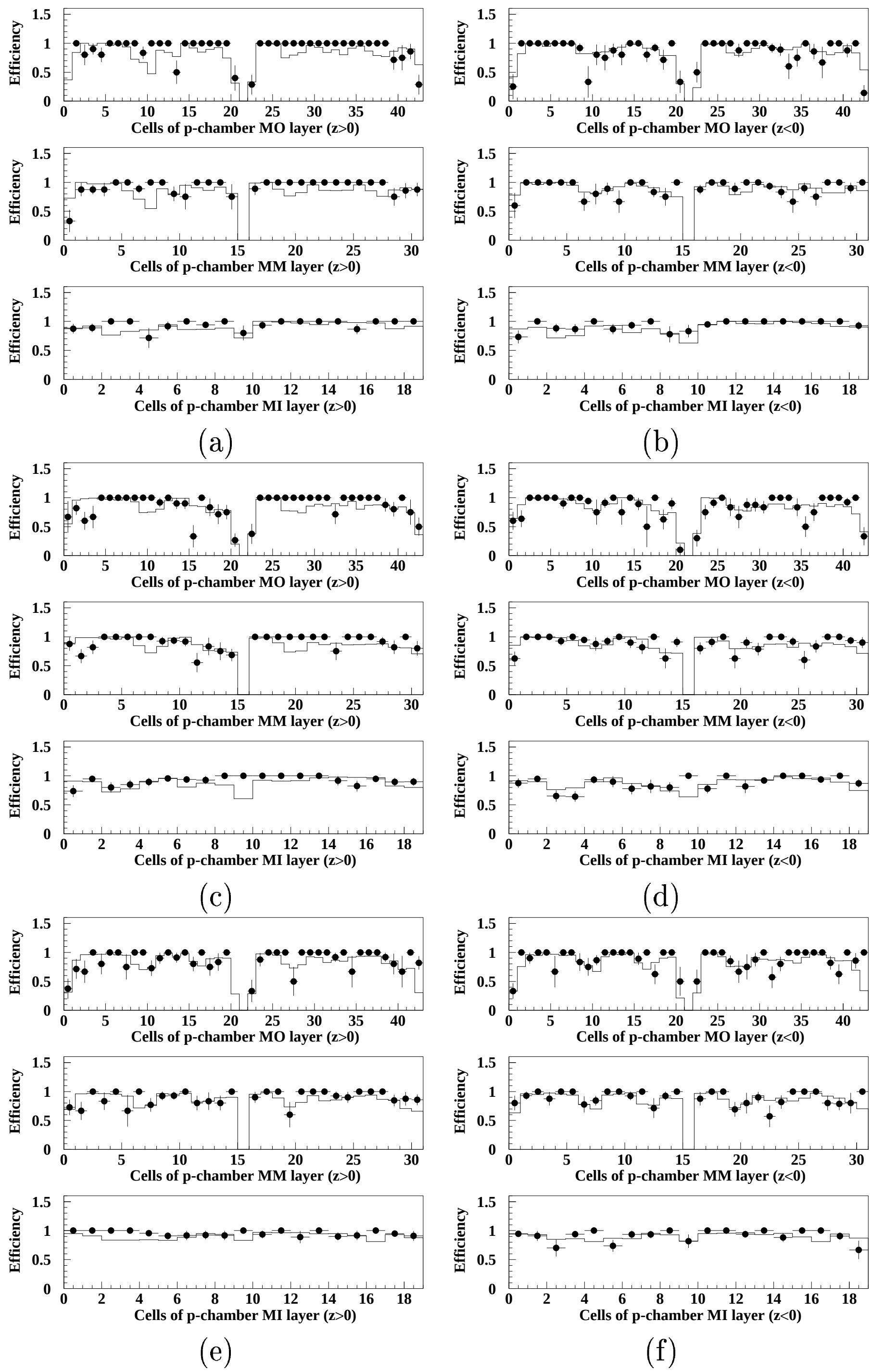

Figure 5.1: Muon chamber P-layer efficiencies for 1998 master side (a), 1998 slave side (b), 1999 master side (c), 1999 slave side (d), 2000 master side (e) and 2000 slave side (f). For each cell in the different layers the efficiency is shown. The efficiencies shown in the plots are the average of the efficiencies of all of the octants in the master ($z > 0$) and slave side ($z < 0$).

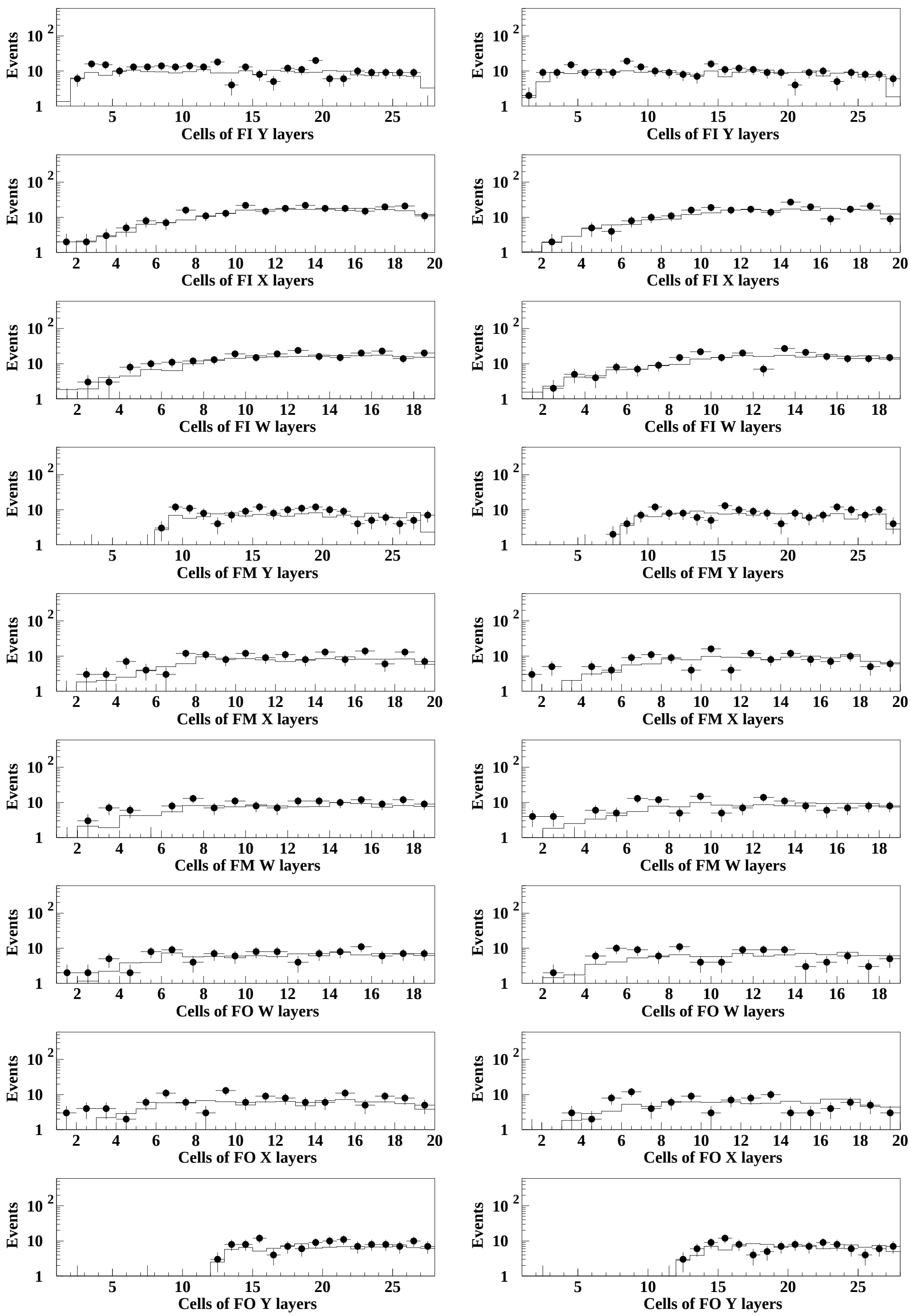

Figure 5.2: Forward/backward muon chambers occupancy for the different layers in the master ($z > 0$, left plots) and slave side ($z < 0$, right plots). The plots shown refer to the 1999 data taking period. A good agreement between data and MC is observed.

Layer	Data 1998 [%]	MC 1998 [%]	Data 1999 [%]	MC 1999 [%]	Data 2000 [%]	MC 2000 [%]
MI	94.7 ± 0.7	93.1 ± 1.4	91.3 ± 0.9	90.7 ± 3.0	94.4 ± 0.8	94.6 ± 2.0
MM	93.2 ± 0.9	89.5 ± 1.8	91.5 ± 1.0	89.5 ± 3.5	90.7 ± 1.1	91.7 ± 2.7
MO	96.2 ± 0.7	95.5 ± 1.4	96.2 ± 0.7	94.6 ± 2.9	95.4 ± 0.8	95.7 ± 2.2
ZI	77.0 ± 1.3	88.1 ± 1.4	76.1 ± 1.3	88.0 ± 3.4	72.9 ± 1.5	87.8 ± 2.9
ZO	71.2 ± 1.7	83.4 ± 2.5	70.2 ± 1.7	82.3 ± 4.8	69.9 ± 1.8	81.6 ± 4.2
FIY	92.0 ± 1.6	96.8 ± 1.9	94.6 ± 1.3	96.8 ± 3.5	85.2 ± 2.2	96.7 ± 3.0
FIX	84.3 ± 2.2	90.6 ± 3.1	84.4 ± 2.2	90.7 ± 5.8	79.2 ± 2.6	89.8 ± 5.0
FIW	83.2 ± 2.3	90.1 ± 3.2	84.1 ± 2.2	90.2 ± 5.9	74.0 ± 2.8	90.1 ± 5.0
FMY	85.0 ± 3.3	92.9 ± 4.1	82.5 ± 3.4	91.5 ± 8.4	72.1 ± 4.4	95.2 ± 5.3
FMX	75.8 ± 3.9	83.2 ± 6.0	74.6 ± 3.9	81.4 ± 11.8	69.2 ± 4.5	85.8 ± 8.8
FMW	78.3 ± 3.8	84.7 ± 5.8	73.0 ± 4.0	81.8 ± 11.7	74.0 ± 4.3	86.7 ± 8.5
FOY	78.3 ± 3.8	84.7 ± 5.8	73.0 ± 4.0	81.8 ± 11.7	74.0 ± 4.3	86.7 ± 8.5
FOX	75.8 ± 3.9	83.2 ± 6.0	74.6 ± 3.9	81.4 ± 11.8	69.2 ± 4.5	85.7 ± 8.8
FOW	85.0 ± 3.3	92.9 ± 4.1	82.5 ± 3.4	91.5 ± 8.4	72.1 ± 4.4	95.2 ± 5.4

Table 5.1: Muon chamber efficiencies for each layer and for the 1998, 1999 and 2000 data taking periods. All values are stable during the three years of data taking analyzed.

5.2 Scintillation counters and RPC efficiency

As already seen in section 4.2.3, a muon pair is required to have at least a scintillator time, $|t_{scin}|$, within 3.5 ns around the beam crossing time to be selected (see section 4.2), so that most of the cosmic background is rejected. Moreover in the forward region the RPCs are also used as a backup for the forward scintillation counters. Then, again, the scintillator and RPC efficiency calculations are crucial for this measurement.

These efficiencies are calculated using a scintillator-independent subsample of dimuon events, requiring two MIPs and a TEC trigger to be present. If we call N_{data}^{sig} the number of times when a scintillator and/or RPC, associated with a muon track, has a timing within the limits, and N_{miss} the number of times in which the timing is out of the limits, the efficiency is:

$$\epsilon = \frac{N_{data}^{sig}}{N_{data}^{sig} + N_{miss}} \tag{5.2}$$

The results of the calculation are listed in table 5.2, separately for the barrel and endcap scintillators and RPCs, on both sides of the detector. The measurements for the 1998, 1999 and 2000 show an overall efficiency of about 80%. The Monte Carlo simulation is in sufficient agreement with data, except in the case of the year 2000, where the high noise on the forward scintillators/RPCs leaded to a reduced performance, not well simulated. For this reason in the analysis of the year 2000 the cut on the endcap scintillator/RPC systems has been removed from

the analysis, exchanging it with a tighter cut on the DCA (see section 4.2.3).
In figure 5.3 the efficiencies of the scintillation counters and RPCs for the year 1999 are shown. The gaps in the barrel scintillators at 0° and 180° are clearly visible, corresponding to the missing counters, showing that the detector acceptance is well simulated.

Type	Scintillators				RPCs	
	Barrel		Endcap			
	Data [%]	MC [%]	Data [%]	MC [%]	Data [%]	MC [%]
1998 all	84.1 ± 1.0	87.3 ± 1.1	85.1 ± 2.3	87.5 ± 0.3	80.5 ± 2.6	67.8 ± 0.4
1998 $z > 0$	-	-	83.5 ± 3.4	88.0 ± 0.4	76.9 ± 3.9	69.9 ± 0.5
1998 $z < 0$	-	-	86.7 ± 3.0	86.9 ± 0.4	84.0 ± 3.4	65.8 ± 0.5
1999 all	82.5 ± 1.0	87.1 ± 0.2	87.6 ± 1.9	87.7 ± 0.4	78.5 ± 2.5	68.9 ± 0.7
1999 $z > 0$	-	-	87.3 ± 2.7	88.9 ± 0.6	74.7 ± 3.6	70.5 ± 0.9
1999 $z < 0$	-	-	88.1 ± 2.8	86.5 ± 0.7	82.7 ± 3.3	67.2 ± 1.0
2000 all	77.6 ± 1.2	86.9 ± 0.2	74.3 ± 2.6	88.0 ± 0.4	56.7 ± 3.0	66.6 ± 0.6
2000 $z > 0$	-	-	77.6 ± 3.4	88.7 ± 0.5	58.0 ± 4.1	67.8 ± 0.7
2000 $z < 0$	-	-	71.0 ± 3.8	87.2 ± 0.6	55.2 ± 4.3	65.3 ± 0.8

Table 5.2: Scintillation counters and RPC efficiencies. Separate values are given for the master ($z > 0$) and slave sides ($z < 0$) as well as the full fiducial volume for the 1998, 1999 and 2000.

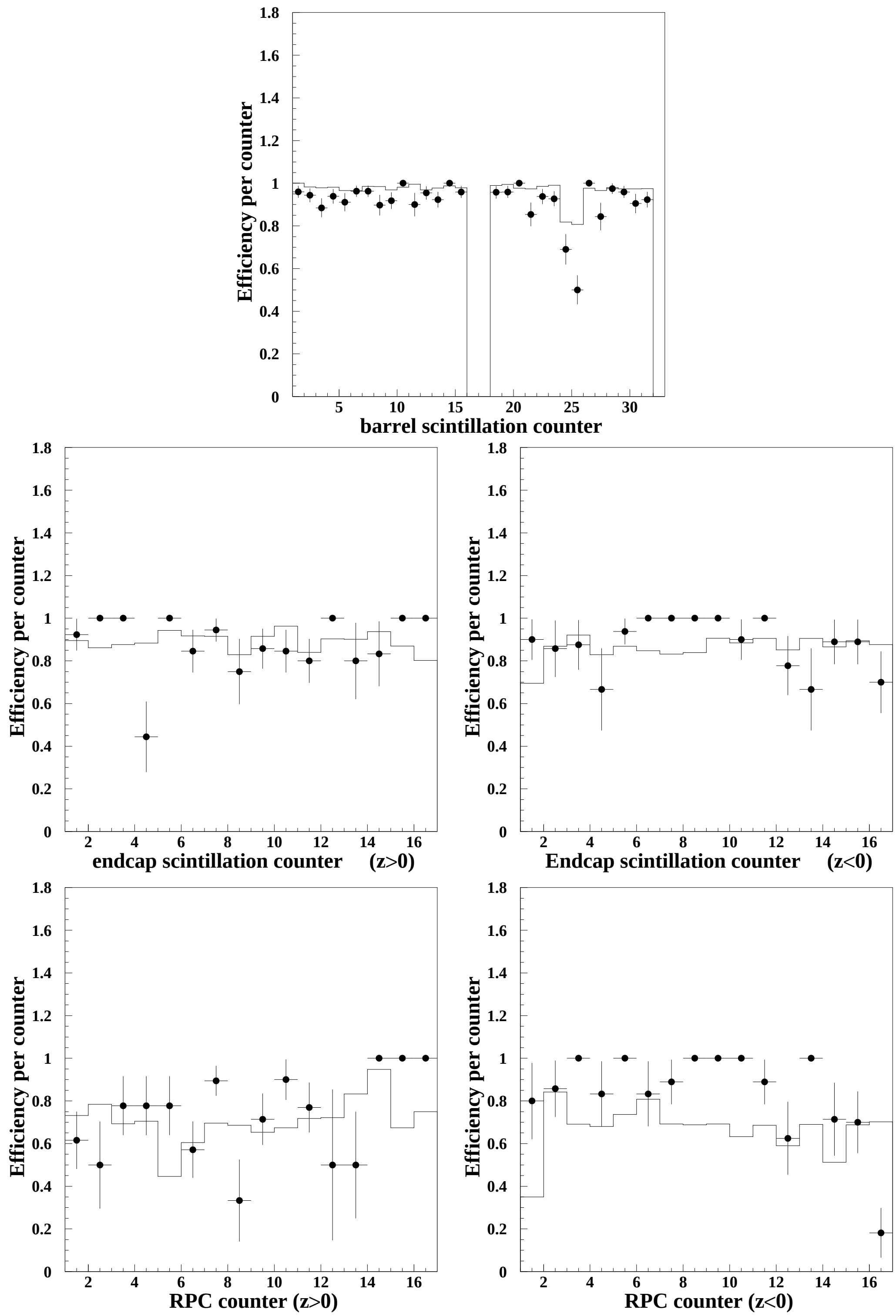

Figure 5.3: Scintillation counters and RPC efficiencies, calculated from the 1999 data (dots) and compared with the Monte Carlo (solid line). The efficiencies for the master ($z > 0$) and slave sides ($z < 0$) are shown, separately for the endcap scintillation and RPC counters.

5.3 MIP reconstruction efficiency

Muons may be identified in the calorimeters as MIPs (isolated clusters). To check the MIP reconstruction efficiency the MM sample has been used, that is a data subsample whose selection is independent from the calorimetric informations.
For each reconstructed track in the muon spectrometer it was checked whether a MIP was reconstructed by tracking back the muon. The efficiency is thus obtained from the number of reconstructed MIPs, N_{rec}, and the number of missing MIPs that should have been reconstructed, N_{miss}, as in section 5.1. The result of the calculation is shown in table 5.3, distinguishing between the barrel, the endcaps and the overall efficiency for the 1998, 1999 and 2000 data taking periods. Data and Monte Carlo agree within the error, with an average efficiencies of more than 94%. The discrepancy between the data and simulated efficiencies in the endcap region for the year 2000 data has a negligible effect on the analysis.
The small discrepancies between data and simulation has a negligible impact on the selection and on the systematic errors since a further check shows that most of the events in the MX sample are already identified by means of muon singlets (one segment in the P-chambers). Moreover the fraction of events of the MX type is of the order of $\sim 15\%$.
In figure 5.4 the MIP reconstruction efficiency versus $|cos\theta|$ and the average efficiency per muon sector in ϕ are shown. A good agreement between data and MC is found.

Year	All		Barrel		Endcap	
	Data [%]	MC [%]	Data [%]	MC [%]	Data [%]	MC [%]
1998	95.2 ± 0.6	97.9 ± 0.1	96.8 ± 0.6	98.3 ± 0.1	91.5 ± 1.4	96.8 ± 0.3
1999	94.7 ± 0.5	97.9 ± 0.1	95.9 ± 0.6	98.4 ± 0.1	91.8 ± 1.2	96.7 ± 0.2
2000	92.6 ± 0.7	97.7 ± 0.1	95.5 ± 0.7	98.2 ± 0.1	87.1 ± 1.5	96.6 ± 0.1

Table 5.3: MIP reconstruction efficiencies for barrel, endcap and the full fiducial volume. Data and Monte Carlo are compared for the year 1998, 1999 and 2000. The average efficiency is $\sim 94\%$.

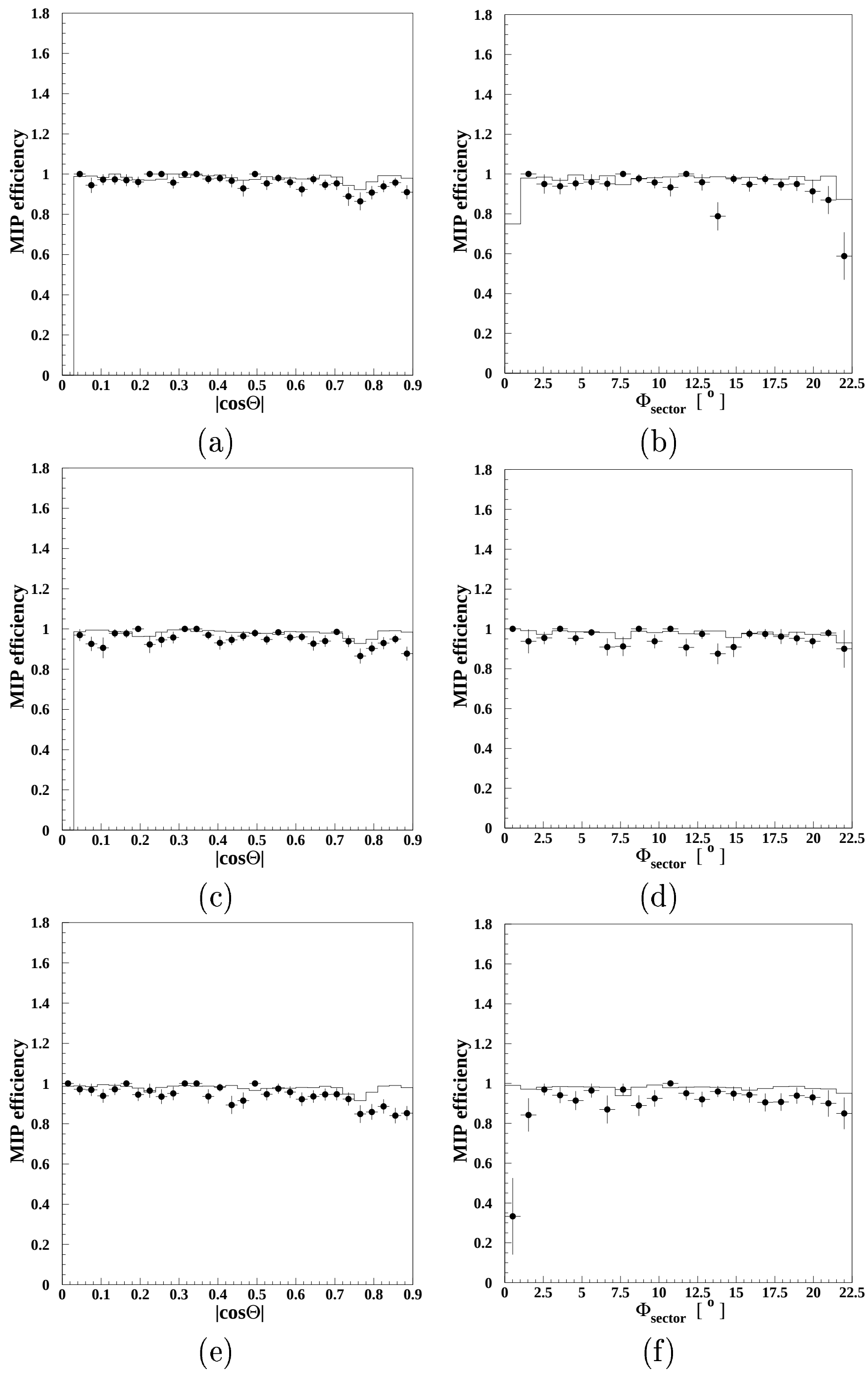

Figure 5.4: MIP efficiency as a function of $|cos\theta|$ (a,c,e) and ϕ (b,d,f). Plots (a), (b) refer to the year 1998, while plots (c), (d) refer to 1999 and (e), (f) to 2000. The efficiency shown in plots (b,d,f) are the average efficiency of a muon sector. A good agreement between data and MC is observed.

5.4 Central tracking chamber efficiency

Selected dimuons must have at least one track reconstructed in TEC and a distance of closest approach (DCA) of less than 1 mm in the $r-\phi$ projection and 25 mm in the z plane (see section 4.2). Possible problems in the High Voltage system in the TEC may cause inefficiencies and could lead to missing reconstruction of tracks. HV problems are simulated in the Monte Carlo, by means of the online database where the time-dependant informations on the detector are stored.
The determination of the TEC efficiency has been done using the MM sample, counting the number of times when one or two tracks are reconstructed in the central tracking chamber and comparing them to the total size of the sample. The results, listed in table 5.4, show that the average efficiency on finding two tracks in the full fiducial volume is more than 98%, in good agreement between data and Monte Carlo simulation.

Type	All		$\|cos\theta\| < 0.7$		$\|cos\theta\| > 0.7$	
	Data [%]	MC [%]	Data [%]	MC [%]	Data [%]	MC [%]
1998 2-tracks	99.4 ± 0.6	99.5 ± 0.5	> 99.9	99.5 ± 0.5	98.0 ± 2.0	99.4 ± 0.6
1999 2-tracks	99.2 ± 0.6	99.3 ± 0.5	> 99.9	99.3 ± 0.6	96.1 ± 2.7	99.2 ± 0.8
2000 2-tracks	98.3 ± 1.0	99.1 ± 0.6	98.5 ± 1.0	99.1 ± 0.7	97.7 ± 2.3	99.0 ± 1.0
1998 1-track	0.6 ± 0.6	0.5 ± 0.4	< 0.1	0.5 ± 0.4	2.0 ± 2.0	0.7 ± 0.7
1999 1-track	0.8 ± 0.6	0.7 ± 0.5	< 0.1	0.7 ± 0.6	3.9 ± 2.7	0.7 ± 0.7
2000 1-track	1.7 ± 1.0	0.9 ± 0.6	1.5 ± 1.0	0.9 ± 0.7	2.3 ± 2.3	1.0 ± 1.0

Table 5.4: Central tracking chamber efficiencies for the regions where $|cos\theta| < 0.7$ (barrel), $|cos\theta| > 0.7$ (endcap) and the full fiducial volume. The probability of finding one or two TEC tracks is compared between data and Monte Carlo for the year 1998, 1999 and 2000. The results show good agreement between data and simulation, with an efficiency of more than 97% on finding two tracks in the full fiducial volume. For 1998 and 1999 in the region where $|cos\theta| < 0.7$ all the events had two tracks and therefore the numbers quoted are upper limits.

5.5 Trigger efficiency

In this section an analysis of the efficiencies of the three trigger levels (level-1, level-2 and level-3) in the L3 experiment is described.

5.5.1 Level-1 trigger efficiency

A muon pair may be triggered by the TEC trigger, the energy trigger (when the photon is present), the muon trigger or any combination of them. The muon

trigger comprehends the barrel and forward muon trigger, depending on the polar angle. The level-1 efficiency for the dimuon selection reduces to the efficiency of these subtriggers. The calculation is performed on the full data sample, in the region with $|cos\theta| < 0.9$.
Two methods for the determination are used:

1. The efficiency for each subtrigger i, ϵ_i, is obtained from the number of events selected by that trigger, N_i, and the number of events selected by at least one of the other triggers $(j,\ k)$, N_{jk}:

$$\epsilon_i = \frac{N_i}{N_{jk}} \tag{5.3}$$

   where i, j and k represent the level-1 subtriggers in any combination. The overall level-1 efficiency, ϵ_{lvl-1}, is then obtained from:

$$\epsilon_{lvl-1} = 1 - (1 - \epsilon_i)(1 - \epsilon_j)(1 - \epsilon_k) \tag{5.4}$$

   where in this case $i = 1, 2, 3$ represents the i-th subtrigger.

2. Since the triggers have two possible state, corresponding to the selection or rejection of the event, an approach based on the Poisson statistics may be used. The data sample is split into different classes, corresponding to the possible subtrigger combinations, for a total of $2^3 = 8$ classes (3 subtriggers with 2 possible states each). The number of expected events for the class i, μ_i, assuming no correlation between the events, is then calculated as:

$$\mu_i = N^{all} \cdot \prod_j \epsilon_j \prod_k (1 - \epsilon_k) \tag{5.5}$$

   where N^{all} is the total number of selected events, j loops over the subtriggers which selected the event and k over the others. The probability to find N_i events when μ_i are expected, $P(N_i,\mu_i)$, is obtained from the Poisson statistics and used to build a likelihood function, $\mathcal{L}$:

$$\begin{aligned} P(N_i,\mu_i) &= \frac{e^{-\mu_i} {\mu_i}^{N_i}}{N_i!} \\ \mathcal{L} &= \prod_i P(N_i,\mu_i) \\ \ln \mathcal{L} &= \sum_i \ln\ P(N_i,\mu_i) \end{aligned} \tag{5.6}$$

   The trigger efficiencies are thus obtained maximizing the logarithm of the likelihood function. The total level-1 efficiency is then obtained in the same way as described in equation 5.4.

The two methods of calculation are compared in table 5.5 for the year 1998, 1999 and 2000. A very good agreement between the two methods is found.

Year	ϵ_{lvl-1}calc [%]	ϵ_{lvl-1}fit [%]
1998	99.8 ± 0.1	99.8 ± 0.1
1999	99.7 ± 0.2	99.7 ± 0.2
2000	98.9 ± 0.4	98.8 ± 0.4

Table 5.5: Level-1 trigger efficiencies, ϵ_{lvl-1}, obtained from the calculation (calc) and from the fit (fit) for the inclusive sample. A very good agreement between the two different methods is observed for all of the three years of data taking.

The efficiencies of the level-1 subtriggers obtained from the calculation method, as well as the combined level-1 efficiency, are listed in table 5.6 for the different energy points and data samples. From the table we observe that the average efficiency of the muon trigger is about 96%, the TEC trigger efficiency is of the order of 85% and the average energy trigger efficiency is $\sim$ 45%. Since all the subtriggers are uncorrelated and at least two of them (TEC and muon) have an high efficiency, the level-1 combined efficiency is always of the order of 99%.

In figure 5.5 the $cos\theta$ angular dependance of the level-1 subtriggers inefficiencies is plotted for the year 1998, 1999 and 2000, together with the combined level-1 trigger inefficiency. The highest inefficiency comes from the TEC and muon triggers, in particular in the region close to the edges ($|cos\theta| \sim 0$ and $|cos\theta| \sim 0.9$), while the energy trigger inefficiency is flat in $cos\theta$.

5.5.2 Level-2 and level-3 trigger efficiencies

Level-2 and level-3 triggers get data from the level-1 trigger and apply more sophisticated criteria to the data, reducing the rate of incoming events. To check the efficiency the so-called *prescaled events* are used. This mechanism is based on the fact that a certain number of events that would have been rejected by the algorythms are neverthless kept. The prescaling factors, f_{ps}, are 10 for the level-2 and 20 for the level-3. If in the dimuon selected sample one or more prescaled event is found, the trigger which tagged the event as prescaled is considered inefficient.
In the analysis from 1998 till the end of LEP in 2000 no prescaled event was found in the selected dimuon data samples, meaning that level-2 and level-3 triggers are 100% efficient on $e^+e^- \to \mu^+\mu^-(\gamma)$ events.

Sample	ϵ_{TEC}[%]	ϵ_{energy}[%]	ϵ_{muon}[%]	ϵ_{lvl-1}[%]
188.6 incl.	86.2 ± 1.3	46.5 ± 3.0	99.8 ± 0.1	99.8 ± 0.1
188.6 non-rad.	92.1 ± 1.4	45.0 ± 4.5	97.3 ± 0.8	99.9 ± 0.1
191.6 incl.	85.4 ± 3.6	54.1 ± 7.1	99.9 ± 0.1	99.9 ± 0.1
191.6 non-rad.	85.3 ± 3.6	54.1 ± 10.5	96.3 ± 2.7	99.9 ± 0.1
195.5 incl.	84.3 ± 2.2	50.9 ± 4.3	96.7 ± 0.9	99.5 ± 0.4
195.5 non-rad.	88.3 ± 2.5	48.5 ± 6.2	97.4 ± 1.2	99.8 ± 0.2
199.6 incl.	71.9 ± 3.2	50.0 ± 4.6	98.0 ± 0.8	99.7 ± 0.3
199.6 non-rad.	74.3 ± 4.2	49.2 ± 6.4	98.1 ± 1.1	99.8 ± 0.2
201.9 incl.	84.9 ± 3.2	50.6 ± 6.5	98.8 ± 0.9	99.8 ± 0.2
201.9 non-rad.	91.8 ± 3.0	51.5 ± 8.5	98.9 ± 1.1	> 99.9
205.0 incl.	88.9 ± 1.9	39.9 ± 5.2	88.9 ± 1.9	97.8 ± 0.8
205.0 non-rad.	93.3 ± 2.2	43.9 ± 7.5	94.7 ± 1.9	98.9 ± 0.8
206.5 incl.	82.7 ± 2.0	46.7 ± 4.0	94.7 ± 1.0	99.1 ± 0.4
206.5 non-rad.	86.2 ± 2.5	46.9 ± 5.6	96.5 ± 1.2	99.0 ± 0.6
208.0 incl.	86.4 ± 5.9	45.5 ± 13.8	97.5 ± 2.5	> 99.9
208.0 non-rad.	94.1 ± 6.1	52.9 ± 20.2	> 99.9	> 99.9

Table 5.6: Level-1 combined trigger efficiencies, ϵ_{lvl-1}, obtained from the fit method. The level-1 subtrigger efficiencies are also shown for the different center-of-mass energies and for both inclusive and non-radiative samples.

5.5.3 Combined trigger efficiency

The combined trigger efficiency, ϵ_{trig}, is calculated as the product of the single trigger efficiencies:

$$\begin{aligned} \epsilon_{trig} &= \epsilon_{lvl-1} \times \epsilon_{lvl-2} \times \epsilon_{lvl-3} \\ \Delta\epsilon_{trig} &= \sqrt{\epsilon^2_{lvl-1} + \epsilon^2_{lvl-2} + \epsilon^2_{lvl-3}} \end{aligned} \tag{5.7}$$

Since level-1 and level-2 triggers are 100% efficient (see section 5.5.2) ϵ_{trig} actually coincides with the level-1 trigger efficiency.

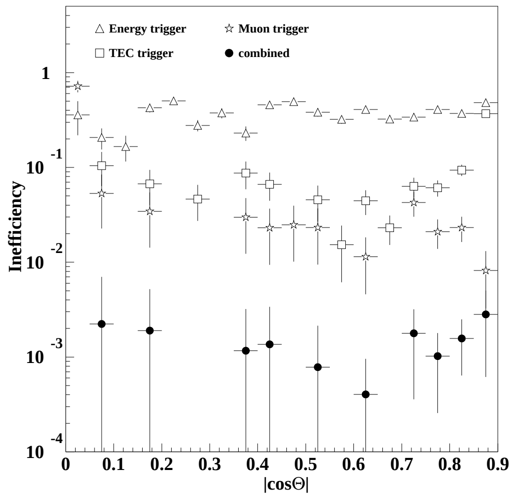

(a)

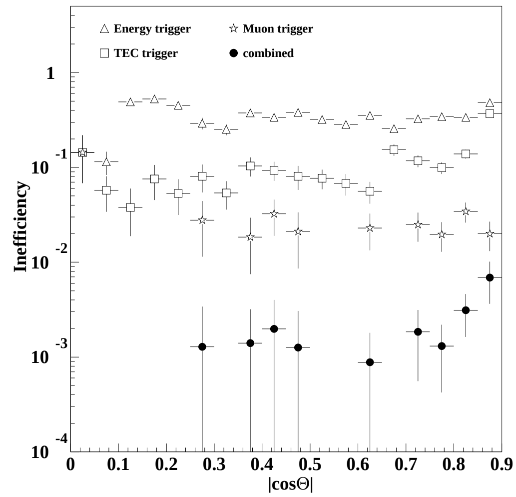

(b)

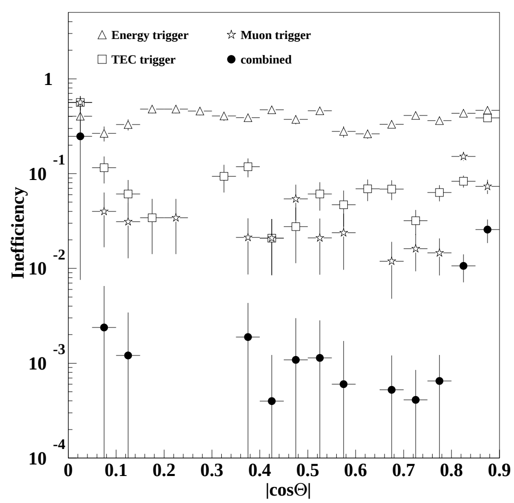

(c)

Figure 5.5: Level-1 trigger inefficiencies as a function of $|cos\theta|$. Plots (a), (b) and (c) show respectively the 1998, 1999 and 2000 level-1 trigger inefficiencies. The inefficiencies contributions of the TEC, energy and muon trigger are shown together with the combined level-1 inefficiency.

Chapter 6

Cross section

The total cross section is calculated, for a given centre-of-mass energy, from the number of data selected events, N_{data}^{sel}, the corresponding integrated luminosity, $\mathcal{L}$, the number of background events expected from Monte Carlo, N^{bkg}, the selection efficiency estimated from the simulation, ϵ_{MC}, and the trigger efficiency, ϵ_{trig}, calculated as in section 5.

$$\sigma_{tot} = \frac{\frac{N_{data}^{sel}}{\epsilon_{trig}} - N^{bkg}}{\mathcal{L}\epsilon_{MC}} \tag{6.1}$$

The differential cross section, $d\sigma/dcos\theta$, is also measured in bins of $cos\theta$ in the region $-0.9 < cos\theta < 0.9$, each bin having an integrated cross section, σ_i, of

$$\sigma_i = \frac{\frac{N_i^{sel}}{\epsilon_i^{trig}} - N_i^{bkg}}{\mathcal{L}\epsilon_i^{MC}} \tag{6.2}$$

where i denotes the bin number in $cos\theta$ and N_i^{sel}, N_i^{bkg}, ϵ_i^{MC}, ϵ_i^{trig}, are respectively the number of data selected events, background events from MC, selection efficiency and trigger efficiency calculated for the bin i.
The number of background events, N^{bkg}, includes the contributions from non-$\mu^+\mu^-$ processes, $N^{non-\mu^+\mu^-}$, ISR contamination, N^{ISR}, and ISR-FSR interference, N^{IFSR}.

$$N^{bkg} = N^{non-\mu^+\mu^-} + N^{ISR} + N^{IFSR} \tag{6.3}$$

6.1 Luminosity determination

The luminosity is determined from the measurement of Bhabha events, $e^+e^- \rightarrow e^+e^-(\gamma)$, at small angle [17]. In that region the theoretical cross section is known at the

0.1 % level. It does not depend on the Z parameters because the photon exchange contribution is dominant at small angles ($|cos\theta| > 0.99$).

In table 6.1 the luminosity collected during the 1998-2000 data taking periods together with the number of dimuon data selected events for each centre-of-mass energy are shown.

Year	$\sqrt{s}$ (GeV)	$\mathcal{L}$ (pb^{-1})	N^{Tot}	N^{HE}
1998	188.6	167.3 ± 0.3	893	420
1999	191.6	28.0 ± 0.1	131	61
1999	195.5	82.1 ± 0.2	397	207
1999/2000	199.6	80.4 ± 0.2	349	185
1999/2000	201.9	38.1 ± 0.1	175	99
2000	205.0	73.5 ± 0.2	358	157
2000	206.5	126.8 ± 0.3	521	260
2000	208.0	8.1 ± 0.1	44	17

Table 6.1: Luminosity collected during the 1998-2000 data taking periods for different centre-of-mass energies. The number of selected data events of each cms energy is shown, both for the inclusive sample (N^{Tot}) and non-radiative sample (N^{HE}).

6.2 Selection efficiency

For each energy point the selection efficiency, ϵ_{MC} is calculated using muon pair Monte Carlo simulated events. The efficiency is defined as the ratio of all the events passing the selection criteria, N^{sel}_{MC}, with the generated $\sqrt{s'}_{gen}$ greater than the $\sqrt{s'}$ cutoff, and the total number of generated events, N^{gen}_{MC}, with a generated $\sqrt{s'}_{gen}$ above the cutoff:

$$\epsilon_{MC} = \frac{N^{sel}_{MC}}{N^{gen}_{MC}} \tag{6.4}$$

$$\Delta\epsilon_{MC} = \sqrt{\frac{\epsilon_{MC}(1-\epsilon_{MC})}{N^{gen}_{MC}}}$$

$$N^{sel}_{MC} = \begin{cases} N^{sel}_{MC}(\sqrt{s'}_{gen} > 75\ GeV) & \text{inclusive sample} \\ N^{sel}_{MC}(\sqrt{s'}_{gen} > 0.85\sqrt{s}) & \text{non}-\text{radiative sample} \end{cases}$$

$$N^{gen}_{MC} = \begin{cases} N^{gen}_{MC}(\sqrt{s'}_{gen} > 75\ GeV) & \text{inclusive sample} \\ N^{gen}_{MC}(\sqrt{s'}_{gen} > 0.85\sqrt{s}) & \text{non}-\text{radiative sample} \end{cases}$$

where the error on the efficiency, $\Delta\epsilon_{MC}$, is estimated according to a binomial distribution.
In table 6.2 a summary of the selection efficiencies in the different data taking periods is shown, both for the inclusive and the non-radiative samples. In figure 6.1 the efficiency as a function of $\sqrt{s'}$ and $cos\theta$ is also plotted. The error quoted is a statistical error derived from the finite size of the MC samples available; the small contribution of this error to the cross section calculation is taken into account as a systematic error. It may be seen from table 6.2 that the selection efficiency of events with hard initial state radiation is lower than for events with no radiation. This is due to the fact that the muons recoil against the emitted photon, resulting in a boost of the muons in the forward direction, close to the beam axis, where the probability to escape detection is higher. The inclusive sample contains about 45% of events with hard radiation and its selection efficiency is always about 10% lower than the selection efficiency of the non-radiative sample.

$\sqrt{s}$ (GeV)	ϵ (inclusive) [%]	ϵ (non-radiative) [%]
188.6	61.4 ± 0.3	75.4 ± 0.3
191.6	60.8 ± 0.8	71.1 ± 1.1
195.5	59.1 ± 0.8	71.1 ± 1.1
199.6	59.0 ± 0.8	70.5 ± 1.1
201.9	59.5 ± 0.8	74.0 ± 1.0
205.0	61.1 ± 0.6	76.1 ± 0.7
206.5	62.1 ± 0.6	76.4 ± 0.7
208.0	61.5 ± 0.8	77.7 ± 0.9

Table 6.2: Selection efficiencies for the different data taking periods. The efficiencies for the inclusive and non-radiative sample are shown. The numbers include all corrections.

6.3 Background

After the described selection cuts most of the backgrounds, shown in section 4.2, are separated from the signal. As shown in the following, additional backgrounds must be taken into account.

6.3.1 Background from cosmic radiation

Assuming a flat distribution for muons coming from cosmic radiation, their rate may be estimated from the sidebands of the DCA and scintillator distributions.

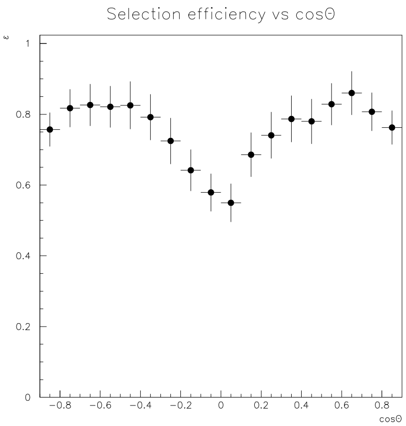

(a)

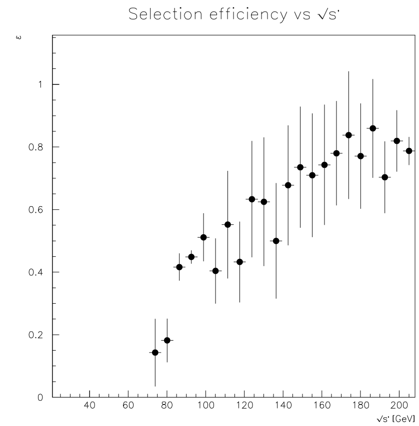

(b)

Figure 6.1: Selection efficiency plotted as a function of $cos\theta$ (a) and $\sqrt{s'}$(b) at $\sqrt{s}$= 208 GeV. The efficiency drops at the very boundary of the muon spectrometer ($|cos\theta| \geq 0.9$) and close to 90°, where no chambers are present (plot a). As a result of the boost of the muons with hard initial state radiation the efficiency in the region $\sqrt{s'} < 0.85\sqrt{s}$ is also depleted (plot b).

For these distribution the number of events, N_{sb}, from the sidebands in a given interval, Δ_{sb}, is counted. The number of selected background events from cosmic radiation, N_{cosm}, in the data selection interval, Δ_{data}, is then extrapolated:

$$N_{cosm} = N_{sb}\frac{\Delta_{data}}{\Delta_{sb}},\ \Delta N_{cosm} = \sqrt{N_{sb}}\frac{\Delta_{data}}{\Delta_{sb}} \tag{6.5}$$

The weighted average of the number of cosmic estimated from DCA and scintillator distributions is defined to be the number of background events, N_{cosmic}, from cosmic radiation. N_{cosmic} is always less than $\sim 1\%$ at all energies. In particular for the 188.6 GeV data sample the estimated number of cosmics is $N_{cosmic} = 0.49 \pm 0.11$ %, while for the 206.5 GeV data sample it increases to $N_{cosmic} = 1.04 \pm 0.20$ %, due to the different cuts on the scintillators in the forward regions (see section 4.1).

6.3.2 Background from e^+e^-annihilation processes

The number of background events coming from other e^+e^- annihilation processes (see 4.1) are estimated using Monte Carlo. The number of selected events for each process i, $N_i^{bkg-sel}$, is counted and then rescaled to the luminosity delivered, $\mathcal{L}$, to obtain the number of background events, N_i^{bkg}:

$$N_i^{bkg} = \mathcal{L}\sigma_i \frac{N_i^{bkg-sel}}{N_i^{bkg-gen}} \tag{6.6}$$

$$\Delta N_i^{bkg} = \mathcal{L}\sigma_i \sqrt{\frac{N_i^{bkg-sel}(N_i^{bkg-gen} - N_i^{bkg-sel})}{N_i^{bkg-gen}}}$$

where σ_i is the theoretical cross section for the process i and $N_i^{bkg-gen}$ the number of generated events from Monte Carlo simulation.
The total number of background events from other e^+e^- processes, N_{phys}^{bkg}, is then calculated by summing up all the contributions coming from the different processes:

$$N_{phys}^{bkg} = N_{\tau\tau}^{bkg} + N_{ee\mu\mu}^{bkg} + N_{\tau\tau\mu\mu}^{bkg} + N_{WW}^{bkg} + N_{Zee}^{bkg} + N_{ZZ}^{bkg} \tag{6.7}$$

$$\Delta N_{phys}^{bkg} = \sqrt{\sum_i (\Delta N_i^{bkg})^2}$$

6.3.3 ISR contamination

A wrong determination of the effective center-of-mass energy $\sqrt{s'}$ may result in events with a calculated $\sqrt{s'}$ higher than the "true" $\sqrt{s'}$. This effect is important for events when the calculated $\sqrt{s'}$ is higher than the low $\sqrt{s'}$ cut for the given sample ($\sqrt{s'} > 75$ GeV for the inclusive sample and $\sqrt{s'} > 0.85\sqrt{s}$ for the non-radiative sample) but the "true" $\sqrt{s'}$ is below the threshold of the sample definition: such events are referred as *ISR background*.
The number of ISR background events, N_{ISR}^{bkg}, is estimated for both samples from Monte Carlo, counting the selected events with the calculated $\sqrt{s'}$ greater than the generated $\sqrt{s'}$, N_{ISR}^{sel}, and compared with the total number of selected events from MC, N_{MC}^{sel}:

$$N_{ISR}^{bkg} = N_{data}^{sig}\epsilon^{ISR} = N_{data}^{sig}\frac{N_{ISR}^{sel}}{N_{MC}^{sel}} \tag{6.8}$$

$$\Delta N_{ISR}^{bkg} = \sqrt{(\epsilon^{ISR}\Delta N_{data}^{sig})^2 + (N_{data}^{sig}\Delta\epsilon^{ISR})^2}$$

where N_{data}^{sig} is the number of signal selected events for the given data sample.
This kind of background is important for the non-radiative sample but is almost negligible for the inclusive sample (see table 6.3).

$\sqrt{s}$ (GeV)	ISR bkg (inclusive) [%]	ISR bkg (non-radiative) [%]
188.6	0.26 ± 0.03	4.21 ± 0.15
191.6	0.42 ± 0.13	5.62 ± 0.65
195.5	0.25 ± 0.10	3.60 ± 0.52
199.6	0.37 ± 0.13	3.53 ± 0.54
201.9	0.26 ± 0.10	3.89 ± 0.53
205.0	0.36 ± 0.08	3.82 ± 0.22
206.5	0.14 ± 0.05	3.82 ± 0.34
208.0	0.15 ± 0.07	4.28 ± 0.52

Table 6.3: ISR background contamination for the different center-of-mass energies.

6.3.4 ISR-FSR interference

As already mentioned in section 2.3.2, in the presence of the interference term between the initial and final state radiation the variable $\sqrt{s'}$ is no longer well defined. The solution chosen here is to consider an interference-free cross section (see equation 2.23):

$$\sigma = \sigma_{nointf} = \sigma_{meas} - \sigma_{intf} \tag{6.9}$$

where the interference part, σ_{intf} may be expressed as (see equation 2.24):

$$\sigma_{intf} = \frac{1}{\epsilon} \int_{-1}^{1} \int_{\sqrt{s'}_{cut}}^{\sqrt{s}} \epsilon(cos\theta, \sqrt{s'}) \frac{d^2\sigma_{intf}}{dcos\theta \; d\sqrt{s'}} \; dcos\theta \; d\sqrt{s'} \tag{6.10}$$

where $\sqrt{s'}_{cut}$ is the appropriate $\sqrt{s'}$ cutoff for the given sample. The interference contribution to the differential cross section is calculated using ZFITTER and the integration is computed numerically, approximating by a summation.
From table 6.4 one may note that the cross section correction due to the ISR-FSR interference is always less than 0.5% for the inclusive sample and 1.4% for the non-radiative sample, the correction for the non-radiative sample being higher since σ_{intf} is higher for values of $\sqrt{s'}$ close to $\sqrt{s}$.

$\sqrt{s}$ (GeV)	ISR-FSR corr (inclusive) [%]	ISR-FSR corr (non-radiative) [%]
188.6	0.45	1.30
191.6	0.36	1.28
195.5	0.42	1.20
199.6	0.46	1.22
201.9	0.49	1.21
205.0	0.36	1.23
206.5	0.45	1.30
208.0	0.34	1.40

Table 6.4: ISR-FSR cross section corrections. All the corrections are lower than 0.5% for the inclusive sample and 1.4% for the non-radiave sample.

6.3.5 Initial state pairs correction (ISPP)

The Monte Carlo used to generate muon pair events, KK2F [18], does not include the radiative corrections from secondary pairs, which are part of the signal (see section 2.3.2) for the inclusive sample. To include these contribution the selection efficiency is therefore modified, adding the contributions from the four fermion events defined as signal (conversion diagrams only, see figure 2.5).
DIAG36 [19] has been used as Monte Carlo generator for the four fermion events. However since DIAG36 does not include the diagrams with Z exchange, the DIAG36 events have been reweighted using the matrix amplitudes from another four-fermion generator, FERMISV [20], which does contain both γ and Z contributions. The mixture of two different generators has been necessary since FERMISV does not treat correctly the electron masses in the region of phase space where the Z contribution is negligible, while DIAG36 does.
For each event two squared matrix elements (one including the Z exchange, $M_{Z,\gamma}^{FERMISV}$, and one excluding it, $M_{\gamma}^{FERMISV}$) are calculated using FERMISV. The ratio $M_{Z,\gamma}^{FERMISV}/M_{\gamma}^{FERMISV}$, in which no problems with the electron masses treatment occurs, is used to reweight the events coming from DIAG36. The total weight of the event $W_{sig/bkg}$ is then calculated from this ratio and the signal/background weight coming from DIAG36, $W_{sig/bkg}^{DIAG36}$:

$$W_{sig/bkg} = \frac{M_{Z,\gamma}^{FERMISV}}{M_{\gamma}^{FERMISV}} W_{sig/bkg}^{DIAG36} \tag{6.11}$$

The selection efficiency, ϵ_{MC}, is then corrected to include the additional contributions:

$$\epsilon_{MC} = \frac{\epsilon_{\mu\mu} \cdot \sigma_{\mu\mu} + \sum_{ff} \epsilon_{\mu\mu ff} \cdot \sigma_{\mu\mu ff}}{\sigma_{\mu\mu} + \sum_{ff} \sigma_{\mu\mu ff}} \tag{6.12}$$

where ϵ_{MC} is the corrected selection efficiency, $\epsilon_{\mu\mu}$ and $\sigma_{\mu\mu}$ the $e^+e^- \to \mu^+\mu^-$ selection efficiency and cross section, and $\epsilon_{\mu\mu f\bar{f}}$, $\sigma_{\mu\mu ff}$respectively the selection efficiencies and cross sections for the $e^+e^- \to f\bar{f}$ processes.
The correction to the cross section is always less than 0.9% (see table 6.5). The efficiencies shown in table 6.2 include these corrections.

$\sqrt{s}$ (GeV)	ISPP correction [%]
188.6	0.65
191.6	0.66
195.5	0.64
199.6	0.63
201.9	0.67
205.0	0.79
206.5	0.87
208.0	0.55

Table 6.5: ISPP cross section corrections. The corrections given in table are applied to the inclusive cross section only.

6.3.6 Background determination

In table 6.6 a summary of the total background contamination for the different center-of-mass energies is shown. The major contribution arises from the $e^+e^- \to e^+e^-\mu^+\mu^-(\gamma)$ process and is $\sim 11\%$ for the inclusive sample and $\sim 6\%$ for the non-radiative sample.

$\sqrt{s}$ (GeV)	Background (inclusive) [%]	Background (non-radiative) [%]
188.6	16.4 ± 0.8	11.2 ± 0.8
191.6	16.6 ± 1.4	15.9 ± 2.1
195.5	18.6 ± 1.5	13.2 ± 1.6
199.6	17.0 ± 1.6	11.7 ± 1.7
201.9	21.0 ± 1.8	15.3 ± 2.2
205.0	19.5 ± 1.0	14.5 ± 1.3
206.5	24.6 ± 1.3	15.9 ± 1.4
208.0	18.8 ± 1.1	17.0 ± 2.1

Table 6.6: Background contamination for the various energy points.

6.4 Results

In table 6.7 the results of the total cross section measurement are summarized for the different energies. They are given separately for the inclusive (σ^{tot}_{incl}) and non-radiative samples ($\sigma^{tot}_{non-rad}$) and compared to the appropriate expectation from the Standard Model, respectively σ^{tot}_{SMincl} and $\sigma^{tot}_{SMnon-rad}$, calculated using ZFITTER.
The statistical error, $\Delta\sigma^{stat}$, is calculated from the following formula (see equation 6.1):

$$\Delta\sigma^{stat} = \frac{\sqrt{N^{sel}_{data}}}{\mathcal{L}\epsilon_{MC}\epsilon_{trig}} \tag{6.13}$$

The discussion on the systematic errors will be presented in section 6.5.
All results are in good agreement with the theoretical prediction and are determined to an average precision of less than 10%. In all measurements the statistical error, coming from the limited statistics, is dominant over the systematic error.

$\sqrt{s}$ [GeV]	$\sigma^{tot}_{incl} \pm (stat) \pm (syst)$ [pb]	σ^{tot}_{SMincl} [pb]	$\sigma^{tot}_{non-rad} \pm (stat) \pm (syst)$ [pb]	$\sigma^{tot}_{SMnon-rad}$ [pb]
188.6	$7.34 \pm 0.29 \pm 0.19$	7.26	$2.93 \pm 0.16 \pm 0.06$	3.20
191.6	$6.41 \pm 0.67 \pm 0.25$	7.00	$2.54 \pm 0.39 \pm 0.09$	3.10
195.5	$6.53 \pm 0.41 \pm 0.22$	6.69	$3.05 \pm 0.25 \pm 0.10$	2.97
199.6	$6.09 \pm 0.39 \pm 0.24$	6.37	$2.85 \pm 0.24 \pm 0.09$	2.84
201.9	$6.08 \pm 0.58 \pm 0.24$	6.25	$2.94 \pm 0.35 \pm 0.10$	2.77
205.0	$6.56 \pm 0.43 \pm 0.32$	5.97	$2.40 \pm 0.23 \pm 0.08$	2.67
206.5	$5.05 \pm 0.29 \pm 0.17$	5.88	$2.26 \pm 0.17 \pm 0.06$	2.63
208.0	$7.16 \pm 1.33 \pm 0.26$	5.78	$2.21 \pm 0.66 \pm 0.08$	2.59

Table 6.7: The total cross section measurements for various center-of-mass energies and their comparison with the Standard Model prediction. The measurement results for the inclusive sample, σ^{tot}_{incl}, and the non-radiative sample, $\sigma^{tot}_{non-rad}$, are shown with their statistical and systematic errors together with their standard model predictions, respectively σ^{tot}_{SMincl} and $\sigma^{tot}_{SMnon-rad}$.

In figure 6.2 the cross section measurements shown in table 6.7 are plotted against the thery prediction for the appropriate sample.

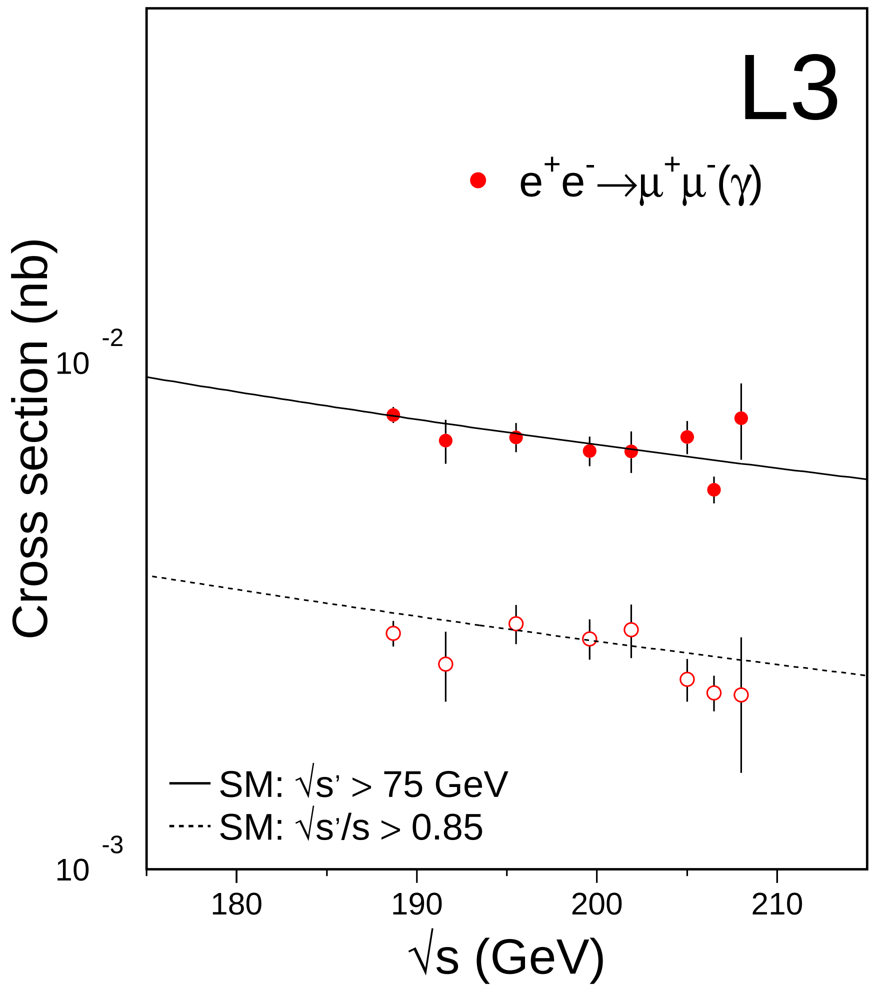

Figure 6.2: Total cross section measurements for 189-208 GeV of center-of-mass energies. The error show is the statistical and systematic combined error.

The differential cross section has been calculated integrating the cross section in bins of $cos\theta$ (see equation 6.2), both for the inclusive and the non-radiative sample. In figure 6.3 the differential cross section for the 205 GeV data sample is compared against the standard model prediction. A good agreement within experimental measure and theory predicition is observed, both for the total and differential cross sections.

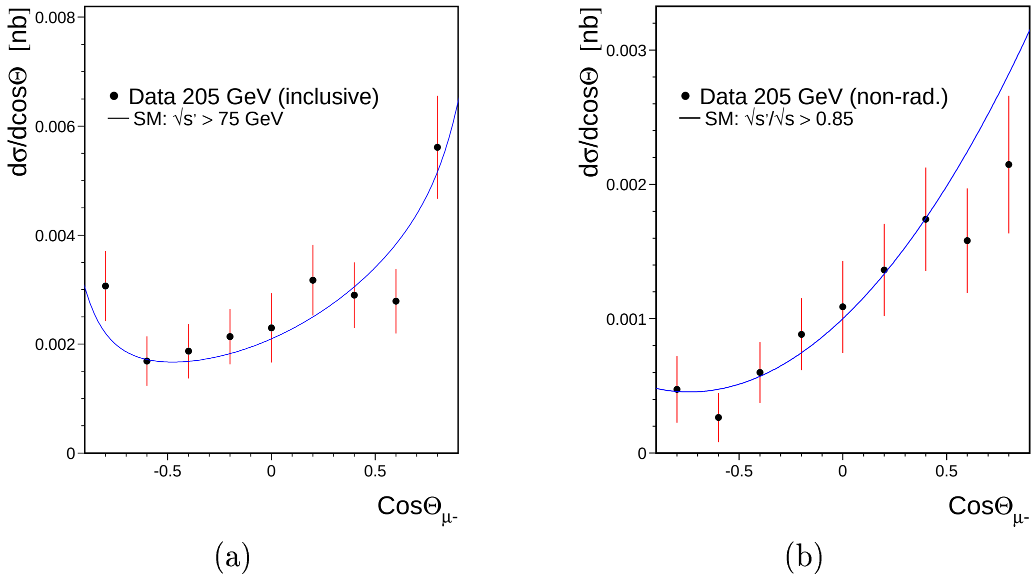

Figure 6.3: Differential cross section for a center-of-mass energyof 205 GeV. The plot (a) refers to the inclusive sample while the plot (b) to the non-radiative sample. The solid line represent the Standard Model prediction.

6.5 Systematic errors

The systematic uncertainties are originating from different sources:

- uncertainty in the placement of the selection cuts;
- uncertainty in the background correction;
- limited knowlegde of the Monte Carlo efficiency;
- uncertainty in the trigger efficiency;
- error on the luminosity measurement.

Other small sources of systematic errors are neglected since the statistical error is always dominating in all measurements.
The total cross section systematic error, $\Delta\sigma^{syst}$, is obtained by summing up all the different contributions (see appendix A, equations A.8-A.13 for the single contribution calculations):

$$\Delta\sigma^{syst} = \sqrt{\Delta\sigma_{cuts}^{syst2} + \Delta\sigma_{bkg}^{syst2} + \Delta\sigma_{MCeff}^{syst\ 2} + \Delta\sigma_{TReff}^{syst\ 2} + \Delta\sigma_{lumi}^{syst\ 2}} \qquad (6.14)$$

The most important source of systematic error is the uncertainty on the placement of the selection cuts. The estimation of this error is obtained by varying

the cuts around the original placement, thus observing the change of the cross section measurement. In figure 6.4 the cut variation for the different variables are shown for the inclusive sample at a center-of-mass energy of 196 GeV. We observe that the most significative cuts are the acceptance cut in $cos\theta$ and the $P_{\max}/E_{beam}$ cut. In this case a systematic error of 0.2% is attributed to the number of clusters cut (ASRC), 0.8% to the muon-muon acollinearity, 0.8% to the muon-mip acollinearity, 1% to the $P_{\max}/E_{beam}$ cut and 2% to the acceptance ($cos\theta$) cut. In the non-radiative sample the error on the acceptance is reduced (figure 6.5) but still is dominant over all the others. The cut variation for the other periods of data taking are similar to the one shown, thus omitted.
A summary of the different contribution to the systematic error on the cross section measurement are shown in table 6.8.

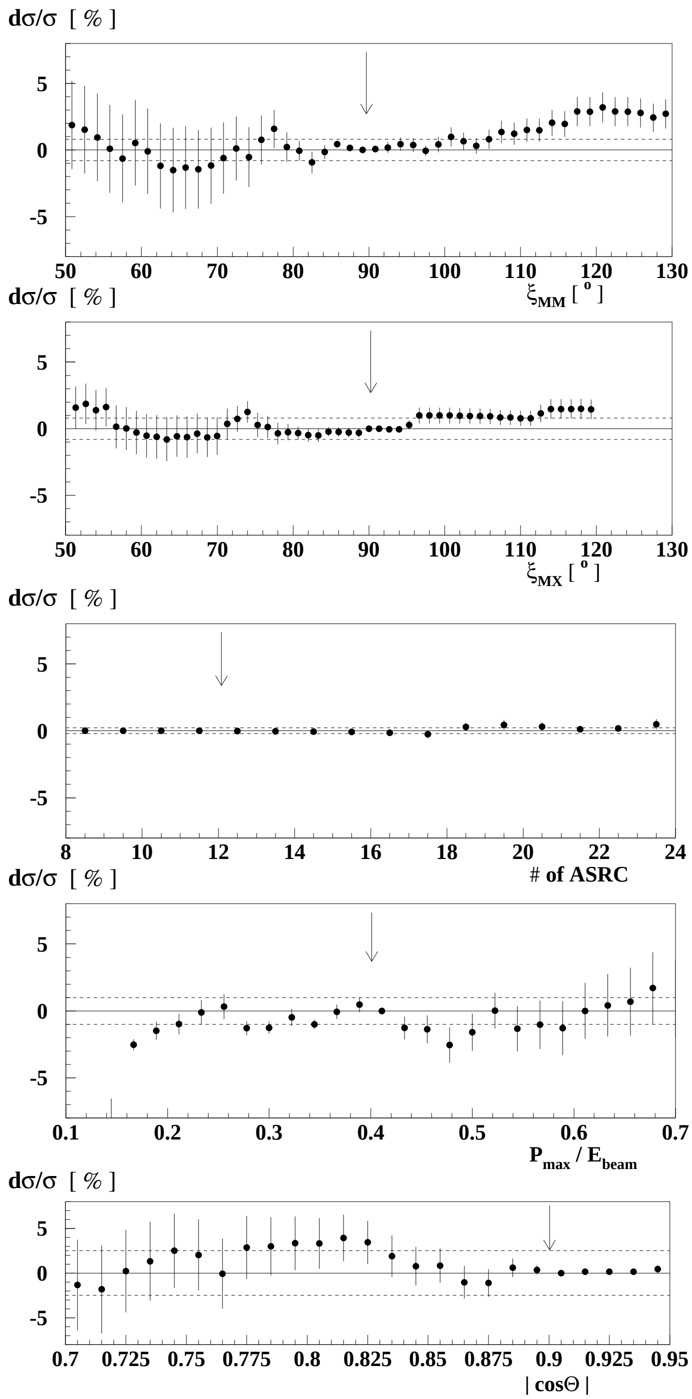

Figure 6.4: Change of cross section measurement arising from a variation of the selection cuts around the original placement point, indicated in the plots by an arrow, for the inclusive sample. The most significant changes are coming from the acceptance ($cos\theta$) cut and the $P_{\max}/E_{beam}$ cut. The plots refer to the 196 GeV data sample.

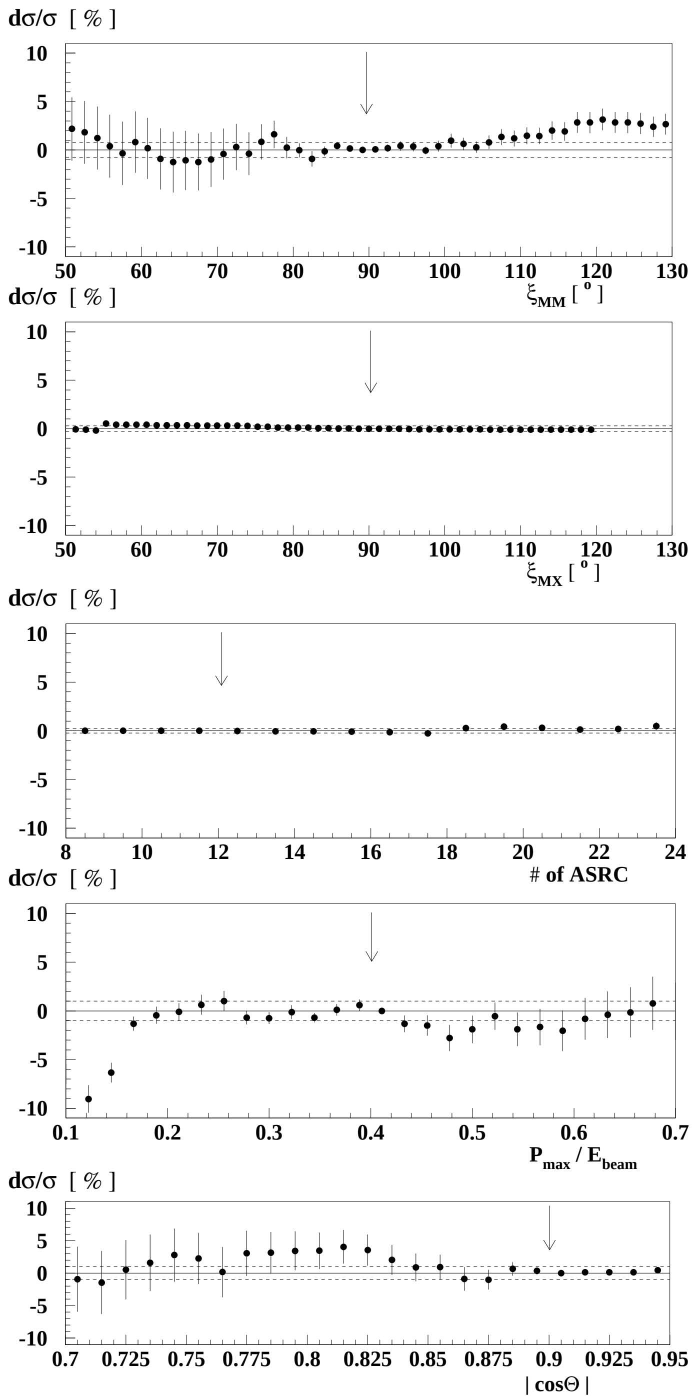

Figure 6.5: Change of cross section measurement arising from a variation of the selection cuts around the original placement point, indicated in the plots by an arrow, for the non-radiative sample. The most significant changes are still coming from the $P_{\max}/E_{beam}$ cut and the acceptance cut, even though reduced with respect to the inclusive sample. The plots refer to the 196 GeV data sample.

$\sqrt{s}$ (GeV)	$\Delta\sigma^{syst}_{cuts}[\%]$	$\Delta\sigma^{syst}_{bkg}[\%]$	$\Delta\sigma^{syst}_{MCeff}[\%]$	$\Delta\sigma^{syst}_{TReff}[\%]$	$\Delta\sigma^{syst}_{lumi}[\%]$	$\Delta\sigma^{syst}[\%]$
188.6 incl.	2.3	0.9	0.4	0.1	0.2	2.5
188.6 non-rad.	1.7	0.9	0.4	0.1	0.2	2.0
191.6 incl.	3.2	1.7	1.3	0.3	0.2	3.9
191.6 non-rad.	2.1	2.6	1.5	0.1	0.2	3.7
195.5 incl.	2.5	1.8	1.4	0.4	0.2	3.4
195.5 non-rad.	2.0	1.9	1.5	0.2	0.2	3.2
199.6 incl.	3.0	1.9	1.4	0.3	0.2	3.9
199.6 non-rad.	2.1	1.9	1.6	0.2	0.2	3.3
201.9 incl.	2.8	2.3	1.4	0.3	0.2	3.9
201.9 non-rad.	1.7	2.6	1.4	0.0	0.2	3.4
205.0 incl.	4.6	1.3	0.9	0.8	0.2	4.9
205.0 non-rad.	2.4	1.6	0.9	0.8	0.2	3.1
206.5 incl.	2.8	1.6	0.9	0.4	0.2	3.4
206.5 non-rad.	2.0	1.6	0.9	0.6	0.2	2.8
208.0 incl.	3.1	1.2	1.3	0.1	0.2	3.6
208.0 non-rad.	2.5	2.5	1.2	0.0	0.2	3.7

Table 6.8: Contributions to the overall systematic error on the cross section calculation, $\Delta\sigma^{syst}$. The errors are given separately for the inclusive and non-radiative samples for the different center-of-mass energies.

Chapter 7

Forward/backward asymmetry

The forward/backward asymmetry, A_{fb}, is defined as:

$$A_{fb} = \frac{\sigma_f - \sigma_b}{\sigma_f + \sigma_b} \tag{7.1}$$

where σ_f and σ_b are, respectively, the integral of the differential cross section for μ^- events going in the same direction of the e^-, $0 < \cos\theta < 1$ (forward region), and in the opposite direction, $-1 < \cos\theta < 0$ (backward region).
The events of the non-radiative sample have always one muon in the forward and one muon in the backward direction, while events of the inclusive sample may be both in the same emisphere, because of the boost from the emission of an initial state photon.

7.1 Charge assignment

The charge of a muon is determined from the bending of the track in the muon chambers. In case the muon is not detected by the muon spectrometer its charge is determined using the inner tracking chamber, TEC.
In case of muons detected in the muon spectrometer the correct charge determination does not only depends on the bending of the trajectory but also on the number of segments reconstructed in the chambers. In particular for muons with only two segments reconstructed in the $r - \phi$ projection (doublets) the reconstructed charge may be ambiguous.
The probability that a muon is assigned the wrong charge, $P_i^{cc_M}$, is calculated using the number of events where both muons are reconstructed in the muon chambers and have the same charge, N_i^{cc}. This calculation is done in different angular regions (barrel, S-region, T-region) and for triplets and doublets, independently.

$$P_i^{ccM} = \frac{N_i^{cc}}{2N_i^{all}} \tag{7.2}$$

where N_i^{all} is the total number of events for the category i of events ($i = 1...5$, corresponding to the triplets in the barrel, S-region, T-region and the doublets in the barrel and endcap regions).
For muons without a track reconstructed in the muon chambers the charge is assigned using the TEC. Two straight lines are fitted, one for each track, and the resulting azimuthal angles ϕ_1 and ϕ_2 from the fit are used to compute the quantity $\Delta\phi = sin(\phi_1 - \phi_2)$, which is considered to be the charge of the first track.
The number of charge confused events for this category (MIPs), N^{cc}, is then calculated selecting an MM sample of events, in which only triplets are present, since the charge confusion for this category of events is very low. The fraction of events from this sub-sample in which the charge assignment from TEC differs from the charge assigned from the muon chambers is N^{cc}. The probability that a MIP is assigned a wrong charge, P_i^{ccX}, is then:

$$P_i^{ccX} = \frac{N_i^{cc}}{2N_i^{all}} \tag{7.3}$$

where $i = 1, 2$, corresponding to the barrel and endcap regions and N_i^{all} is the total number of events in the appropriate sample.
In table 7.1 the probability that a wrong charge is assigned to a single muon is listed for the different categories and topologies for the 196 GeV data sample.

Type	barrel [%]	S-region [%]	T-region [%]
P^{ccM} triplets	0.47 ± 0.94	16.67 ± 13.61	4.55 ± 8.67
P^{ccM} doublets	8.82 ± 9.25	18.75 ± 17.12	
P^{ccX}	6.32 ± 3.56	11.90 ± 9.29	

Table 7.1: Probability that a muon has assigned the wrong charge for different categories and topologies. The results shown are from the 196 GeV data sample.

The probability that both muons have the wrong charge assigned is the product of the single probabilities:

$$P_{\text{cc}} = P_i^{cc} \cdot P_j^{cc} \tag{7.4}$$

The probability of charge confusion, κ, is then calculated from P_{cc} for the different events samples MM and MX:

$$\kappa_{\text{MM}} = \frac{P_i^{ccM} \cdot P_j^{ccM}}{1 - P_i^{ccM} - P_j^{ccM}} \tag{7.5}$$

$$\kappa_{\mathrm{MX}} = \frac{P_i^{ccM} \cdot P_j^{ccX}}{1 - P_i^{ccM} - P_j^{ccX}} \tag{7.6}$$

The weighted average of the MM and MX sample probabilities, κ_{MM} and κ_{MX}, gives the overall probability of charge confusion, κ. The values of κ for the different energy points are always less than 0.8% and are listed in table 7.2.

$\sqrt{s}$ [GeV]	κ (incl. sample) [%]	κ (non-rad. sample) [%]
188.6	0.32 ± 0.03	0.42 ± 0.03
191.6	0.76 ± 0.14	0.18 ± 0.07
195.5	0.30 ± 0.04	0.30 ± 0.06
199.6	0.48 ± 0.06	0.40 ± 0.07
201.9	0.60 ± 0.10	0.28 ± 0.08
205.0	0.57 ± 0.07	0.33 ± 0.07
206.5	0.68 ± 0.06	0.40 ± 0.06
208.0	0.40 ± 0.07	0.48 ± 0.12

Table 7.2: Overall charge confusion probability, κ, for the different center-of-mass energies and for the inclusive and non-radiative samples. All the values at all energies are lower than 0.8%.

7.2 A_{fb} determination

The differential cross section may be approximated at Born level by the following equation:

$$\frac{d\sigma}{d\ cos\theta} \propto \frac{3}{8}(1 + cos^2\theta) + A_{fb}\ cos\theta \tag{7.7}$$

where θ is the polar angle between the emitted μ^- and the incoming e^-. This equation represents well the differential cross section for the non-radiative sample. In the inclusive sample, instead, the emission of initial state photons distorts the measured $cos\theta$ distribution, thus equation 7.7 does not describe the experimental differential cross section anymore.
Two different methods for the A_{fb} calculation are applied, corresponding to the inclusive and non-radiative sample:

1. **inclusive sample:**
   A_{fb} is determined directly from the the forward and backward cross sections, thus assuming nothing on the shape of the differential cross section;

2. **non-radiative sample:**
   A_{fb} is determined using an unbinned maximum likelihood fit, where the likelihood function is defined as the product over the selected events of the differential cross section at Born level, as in equation 7.7.

The reason of the choice of a fit for the A_{fb} determination in the non-radiative sample, instead of the direct calculation, is because the statistical power of the fit method is higher than in the other case, and therefore it yields lower errors on A_{fb}.

7.2.1 A_{fb} determination from the differential cross section

The forward/backward asymmetry, A_{fb}, may be determined directly from the the forward and backward cross sections, as from equation 7.1. By this no assumption on the shape of the differential cross section is made. Therefore this is useful to calculate the asymmetry for the inclusive sample, where the formula 7.7 is no longer correct.
Using the differential cross section measurement, in bins of $cos\theta$ as described in chapter 6, the forward and backward cross sections, σ_f and σ_b, are calculated in the region with $|cos\theta| < 0.9$. The asymmetry obtained is then extrapoled to the full solid angle using the theoretical predictions. An extrapolation factor, C_{ex}, is therefore calculated by the comparison of the asymmetry in the range $|cos\theta| < 0.9$, ${A_{fb}}^{ZF,|cos\theta|<0.9}$, and in the full solid angle, ${A_{fb}}^{ZF,4\pi}$, obtained from ZFITTER:

$$C_{ex} = \frac{{A_{fb}}^{ZF,4\pi}}{{A_{fb}}^{ZF,|cos\theta|<0.9}} \tag{7.8}$$

Since the same extrapolation factor, C_{ex}, calculated using the Monte Carlo agrees at all energies with the one calculated by ZFITTER within 0.5%, the value coming from ZFITTER has been used, assigning to it an error of 0.5%. In table 7.3 the extrapolation factors for the different energy points are listed.
The charge confusion effect on the inclusive sample A_{fb} calculation is very small, compared to the statistical error and the error coming from the background subtraction, therefore its effect on the measurement is neglected.

7.2.2 A_{fb} determination from an unbinned likelihood fit

A_{fb} may be calculated using a likelihood fit of the angular distribution at the Born level approximation: this assumes the validity of the Born approximation, thus it can only be used for the asymmetry caculation of the non-radiative sample. The likelihood for a single event, P_i, is then:

$\sqrt{s}$ [GeV]	C_{ex}
188.6	1.018 ± 0.005
191.6	1.016 ± 0.005
195.5	1.014 ± 0.005
199.6	1.012 ± 0.005
201.9	1.010 ± 0.005
205.0	1.009 ± 0.005
206.5	1.008 ± 0.005
208.0	1.007 ± 0.005

Table 7.3: A_{fb} extrapolation factors for the inclusive sample. The corrections range from 1.018 to 1.007.

$$P_i(A_{fb}^{fit}) = \frac{3}{8}(1+cos^2\theta_i) + A_{fb}^{fit} cos\theta_i \tag{7.9}$$

where θ_i is the polar angle of the i-th event and A_{fb}^{fit} is the fitted A_{fb} value to be determined.
The likelihood function, $\mathcal{L}$, is the product over all the n events in the fit of the single probabilities P_i. The value of A_{fb}^{fit} is determined maximizing the logarithm of the likelihood function:

$$\ln\ \mathcal{L} = \sum_{i=1,n} \ln P_i(A_{fb}^{fit}) = \sum_{i=1,n} \ln\left[\frac{3}{8}(1+cos^2\theta_i) + A_{fb}^{fit} cos\theta_i\right] \tag{7.10}$$

Including the charge confusion effect and the ISR-FSR interference in the fit and assuming a symmetric acceptance in $cos\theta$ (see figure 6.1a), equation 7.10 becomes (see also equation 6.10):

$$\begin{aligned} P_i'(A_{fb}^{fit}) &= P_i(A_{fb}^{fit}) + f_{IFSR}(cos\theta) \\ \ln\ \mathcal{L} &= \sum_{i=1,n} \ln\left[(1-\kappa_i)P_i'(A_{fb}^{fit}) + \kappa_i P_i'(-A_{fb}^{fit})\right] \\ &= \sum_{i=1,n} \ln(1-2\kappa_i)\left[\frac{3}{8}(1+cos^2\theta_i) + A_{fb}^{fit} cos\theta_i + f_{IFSR}(cos\theta)\right] \\ f_{IFSR}(cos\theta) &= \frac{1}{\epsilon(cos\theta)\sigma_{nointf}} \int_{\sqrt{s'}_{cut}}^{\sqrt{s}} \epsilon(cos\theta,\sqrt{s'}) \frac{d^2\sigma_{intf}}{dcos\theta\ d\sqrt{s'}}\ d\sqrt{s'} \end{aligned} \tag{7.11}$$

where κ_i is the charge confusion probability for the event i, f_{IFSR} the additional term coming from the IFSR interference, and $P_i(A_{fb}^{fit})$ the likelihood function modified to include the IFSR term. This fit procedure gives directly the asymmetry in the full solid angle, so that no additional correction has to be applied.

Background subtraction

The background is subtracted using the same fitting procedure as described in the previous section. ISR background is also taken into account, measuring its asymmetry $A_{\mathrm{fb}}^{\mathrm{isr}}$ by counting the number of events in the forward, $N_{\mathrm{f}}^{\mathrm{isr}}$, and backward directions, $N_{\mathrm{b}}^{\mathrm{isr}}$, estimated using Monte Carlo:

$$\begin{aligned} A_{\mathrm{fb}}^{\mathrm{isr}} &= \frac{N_{\mathrm{f}}^{\mathrm{isr}} - N_{\mathrm{b}}^{\mathrm{isr}}}{N_{\mathrm{f}}^{\mathrm{isr}} + N_{\mathrm{b}}^{\mathrm{isr}}} \\ \Delta A_{\mathrm{fb}}^{\mathrm{isr}} &= 2\sqrt{\frac{N_{\mathrm{f}}^{\mathrm{isr}} N_{\mathrm{b}}^{\mathrm{isr}}}{(N_{\mathrm{f}}^{\mathrm{isr}} + N_{\mathrm{b}}^{\mathrm{isr}})^3}} \end{aligned} \tag{7.12}$$

For each background channel i the calculated asymmetry, $A_{fb}^{bkg^i}$, is combined with the others with its weight ω_i. The background corrected asymmetry, A_{fb}^{BkgC}, is then obtained by:

$$A_{fb}^{BkgC} = \frac{A_{fb}^{fit} - \sum_i \omega_i A_{fb}^{bkg^i}}{1 - \sum_i \omega_i} \tag{7.13}$$

The background corrections, C_{bkg}=$A_{fb}^{fit}/A_{fb}^{BkgC}$, are of the order of 1.14±0.05 (see table 7.4).

$\sqrt{s}$ [GeV]	C_{bkg}
188.6	1.10 ± 0.01
191.6	1.19 ± 0.05
195.5	1.13 ± 0.03
199.6	1.10 ± 0.03
201.9	1.17 ± 0.04
205.0	1.14 ± 0.04
206.5	1.14 ± 0.03
208.0	1.16 ± 0.05

Table 7.4: A_{fb} correction factors, C_{bkg}. The corrections refer to the non-radiative sample and are of the order of 1.14 ± 0.05.

7.3 Results

In table 7.5 the results of the A_{fb} measurements are listed for various center-of-mass energies. The results for the inclusive and non-radiative samples are shown

separately, comparing them to the appropriate expectations from the Standard Model, calculated using ZFITTER.
In all measurements the statistical error, coming from the limited statistics, is dominant over the systematic error.

$\sqrt{s}$ [GeV]	N_f	N_b	$A_{fb}^{incl} \pm (stat) \pm (syst)$	A_{fb}^{SM}	N_f	N_b	$A_{fb}^{non-rad} \pm (stat) \pm (syst)$	A_{fb}^{SM}
188.6	508	290	$0.291 \pm 0.044 \pm 0.024$	0.310	323	97	$0.556 \pm^{+0.042}_{-0.044} \pm 0.009$	0.573
191.6	82	49	$0.425 \pm 0.129 \pm 0.086$	0.308	48	13	$0.692 \pm^{+0.107}_{-0.133} \pm 0.065$	0.569
195.5	259	129	$0.329 \pm 0.066 \pm 0.039$	0.306	151	46	$0.532 \pm^{+0.062}_{-0.067} \pm 0.042$	0.564
199.6	226	123	$0.310 \pm 0.066 \pm 0.044$	0.304	126	59	$0.437 \pm^{+0.072}_{-0.077} \pm 0.039$	0.560
201.9	121	54	$0.360 \pm 0.102 \pm 0.053$	0.303	75	24	$0.586 \pm^{+0.089}_{-0.094} \pm 0.024$	0.557
205.0	236	122	$0.340 \pm 0.070 \pm 0.053$	0.302	110	47	$0.481 \pm^{+0.084}_{-0.090} \pm 0.028$	0.554
206.5	346	175	$0.316 \pm 0.060 \pm 0.032$	0.302	189	71	$0.544 \pm^{+0.059}_{-0.063} \pm 0.020$	0.553
208.0	33	11	$0.360 \pm 0.198 \pm 0.101$	0.301	14	3	$0.715 \pm^{+0.110}_{-0.191} \pm 0.041$	0.551

Table 7.5: A_{fb} determinations for various energies and comparison with the Standard Model predictions, A_{fb}^{SM}. The results are given separately for the inclusive, A_{fb}^{incl}, and non-radiative sample, $A_{fb}^{non-rad}$. The statistical and systematic errors are shown.

In figure 7.1 a plot of the A_{fb} measurement results are compared to the Standard Model expectation for both samples. A good agreement between measurements and theoretical prediction is found.

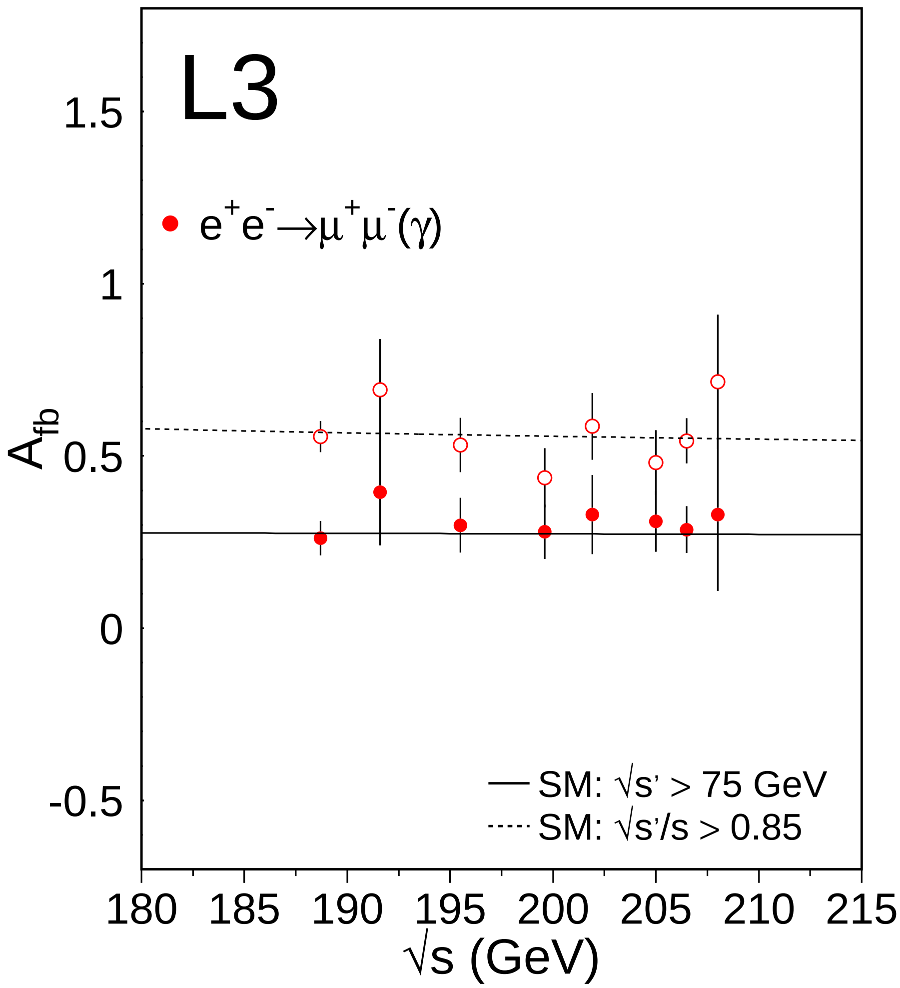

Figure 7.1: A_{fb} measurements for center-of-mass energies from 189 GeV to 208 GeV. The errors quoted in the plot are the statistical and systematic errors combined.

7.4 Systematic errors

The main sources of systematic errors for the A_{fb} measurement are coming from the background subtraction, the acceptance cut in $cos\theta$ and the muon momentum reconstruction. For the inclusive sample only an additional contribution is due to the error on the extrapolation factor, C_{ex}. The charge confusion is included in the systematic errors only for the non-radiative sample, since in the inclusive

sample it is negligible compared to the other contributions and to the statistical error. Other sources of systematic errors are negligible.
The systematic errors coming from the background subtraction are taken from the uncertainty on the background correction from Monte Carlo, for the inclusive sample, and directly from the error on C_{bkg} (see table 7.4), for the non-radiative sample. The contributions from the acceptance cut in $cos\theta$ and on the muon momentum reconstruction are estimated variating respectively the cut on $|cos\theta|$ and on $P_{\max}/E_{beam}$ around the original placement, thus observing the effect on the asymmetry measurement. Furthermore, for the inclusive sample only, the systematics on C_{ex} are estimated directly from its error (see table 7.3). The charge confusion corrections to the asymmetry in the non-radiative sample, $2\kappa A_{fb}^{fit}$, gives also a contribution to the systematics of $2\Delta\kappa A_{fb}^{fit}$. A breakdown of the estimation of the systematic errors for the different energy points and for both inclusive and non-radiative sample is given in table 7.6, together with the overall systematic error. All values are below the corresponding statistical errors.

$\sqrt{s}$ [GeV]	Bkg corr.	Acceptance	Momentum rec.	C_{ex}	Charge conf.	ΔA_{fb}^{syst}
188.6 incl.	0.0160	0.0066	0.0152	0.0050	-	0.0236
188.6 non-rad.	0.0075	0.0025	0.0038	-	0.0002	0.0088
191.6 incl.	0.0549	0.0536	0.0378	0.0050	-	0.0857
191.6 non-rad.	0.0346	0.0429	0.0345	-	0.0005	0.0650
195.5 incl.	0.0316	0.0220	0.0061	0.0050	-	0.0393
195.5 non-rad.	0.0131	0.0276	0.0289	-	0.0003	0.0421
199.6 incl.	0.0334	0.0192	0.0213	0.0050	-	0.0443
199.6 non-rad.	0.0128	0.0242	0.0270	-	0.0007	0.0385
201.9 incl.	0.0481	0.0078	0.0206	0.0050	-	0.0531
201.9 non-rad.	0.0207	0.0029	0.0110	-	0.0009	0.0236
205.0 incl.	0.0489	0.0205	0.0013	0.0050	-	0.0533
205.0 non-rad.	0.0186	0.0196	0.0067	-	0.0007	0.0279
206.5 incl.	0.0295	0.0061	0.0109	0.0050	-	0.0324
206.5 non-rad.	0.0134	0.0054	0.0132	-	0.0007	0.0196
208.0 incl.	0.0894	0.0370	0.0266	0.0050	-	0.1005
208.0 non-rad.	0.0398	0.0022	0.0077	-	0.0017	0.0406

Table 7.6: A breakdown of the A_{fb} systematic error contributions for the different energy points. The estimations are given separately for the inclusive, and non-radiative samples.

Chapter 8

New physics

As has already been stated in section 2.4.1, the results from the muon pair analysis can be used to search for physics beyond the Standard Model. In this chapter the results from the search for contact interactions effects are described.

8.1 Contact interactions

The theory of contact interactions offers a general framework to search for new physics. Contact interactions affect the shape of the differential cross section $d\sigma/dcos\theta$ (see equation 2.30):

$$\frac{d\sigma}{d\ cos\theta} = \frac{d\sigma^{SM}}{d\ cos\theta} + c_2(s, cos\theta)\frac{1}{\Lambda^2} + c_4(s, cos\theta)\frac{1}{\Lambda^4}$$

where σ^{SM} denotes the Standard Model cross section, the term with c_2 denotes the pure contact interaction amplitude and the term with c_4 represents the interference between the Standard Model and the new physics. The contact interactions, therefore, would manifest themselves as a deviation between the measured and SM predicted cross section and forward/backward asymmetries.

To search for these effects the contributions of contact interactions are included in the theory calculations, using ZFITTER. The Standard Model parameters are fixed to $m_Z = 91.190$ GeV (Z boson mass), $\alpha_s(m_Z^2) = 0.119$ (strong interaction constant), $\alpha(m_Z) = 1/128.894$ (hyperfine structure constant), $m_t = 173.8$ GeV (top quark mass) and $m_H = 150$ GeV (Higgs boson mass). The results of the analysis are not sensitive to small changes of these values. The theoretical predictions, as calculated from ZFITTER, are assumed to have an uncertainty below 0.5%.

The contribution of new physics is obtained using a χ^2 fit to all cross section and forward/backward asymmetry measurements obtained at LEP II ($\sqrt{s} > 130$ GeV). For this purpose, assuming that all measurements are independent, the χ^2 is defined as:

$$\chi^2 = \sum_i \left[\frac{(\sigma_i^{exp} - \sigma_i^{th})^2}{\sigma_{xsec,i}^2} + \frac{(A_{fb,i}^{exp} - A_{fb,i}^{th})^2}{\sigma_{A_{fb},i}^2} \right] \tag{8.1}$$

where the sum spans over all the energy points. σ_i^{exp} σ_i^{th}, $\sigma_{xsec,i}^2$ are respectively the experimental cross section, the theoretical cross section and the correspondent variance for the energy point i. $A_{fb,i}^{exp}$, $A_{fb,i}^{th}$ and $\sigma_{A_{fb},i}^2$ are respectively the experimental asymmetry, the theoretical asymmetry and the correspondent variance.
The limits on the Λ values are obtained by minimizing the χ^2 function. The results of the measurements, expressed as one-sided 95% CL limits on the Λ values, are summarized in table 8.1, for each of the various models. In the table Λ_- (destructive interference) and Λ_+ (constructive interference) are the values of Λ, in equation 2.26, corresponding to the upper and lower sign of η_{ij} (see table 2.2). In figure 8.1 the plot of the limits is also shown.
Similar limits have been obtained at HERA [21, 22] and TEVATRON [23, 24], using hadronic final states, while the pure leptonic channel is only accessible at LEP.

Model	Λ_- [TeV]	Λ_+ [TeV]
LL	4.7	10.4
RR	4.4	10.0
LR	2.0	6.8
RL	2.0	6.8
VV	8.2	16.2
AA	7.6	13.6
V0	6.6	14.4
A0	2.1	9.4
LL-RR	4.1	5.1

Table 8.1: One-sided 95% confidence level lower limits on the Λ parameter for contact interactions. The Λ_- and Λ_+ values correspond to the upper and lower sign of η_{ij} (see 2.4.1).

To fit the contact interaction models to the data a new parameter is also introduced, $\epsilon = 1/\Lambda^2$, with $\epsilon = 0$ if there are no contact interactions. In the fit ϵ is allowed to have both positive and negative values.
The results of the estimation of ϵ are given in table 8.2. The values shown are fully compatible with the Standard Model expectation of $\epsilon = 0$, from which we can conclude that no evidence of manifestation of new physics from contact interaction is found. From table 8.1 it can also be seen that at 95% confidence level the lowest estimated energy scale for new physics is $\Lambda_{min} = 2$ TeV, corresponding

to the destructive interference (Λ_-) of the LR and RL models, meaning that if a new heavy particle exists it cannot have a mass of less than 2 TeV.
Using all the leptonic channels from all the LEP experiments the limits can be improved [25]. In figure 8.2 the result of the combination of the data coming from all LEP experiment is shown, assuming lepton universality. With this procedure the lowest limit on the energy scale for LEP has been set to 8.5 TeV.
Under the hypothesis that the fermions are not pointlike, the upper limits on the fermion size, R, may be obtained from the fitted limits on Λ, via the uncertainty principle ($\Delta P \Delta R \sim 1$, using $\hbar = c = 1$, where R is the radius of the fermion, P the momentum of the exchanged particle, $\hbar$ the reduced Planck constant and c the speed of light):

$$\begin{aligned} R_1 \sim & \frac{1}{P} < \frac{1}{\Lambda_{min}} \\ R_2 \sim & \frac{1}{P} < \frac{1}{\Lambda_{max}} \end{aligned} \tag{8.2}$$

where Λ_{max} is the maximum value of the limits on Λ, corresponding to the VV model with positive interference, and Λ_{min} is the minimum value of the limits on Λ, corresponding to the LR/RL models with destructive interference. The upper limits on the radius R range from R_1 to R_2, depending on the model. The L3 limits yield to $R < 1.0 \cdot 10^{-17} \div 1.2 \cdot 10^{-18}$ cm, while using the LEP combined results the upper limit on R becomes $R < 2.3 \cdot 10^{-18} \div 7.6 \cdot 10^{-19}$ cm.

Model	ϵ [TeV^{-2}]
LL	$-0.0248^{+0.0122}_{-0.0107}$
RR	$-0.0289^{+0.0153}_{-0.0105}$
LR	$-0.0100^{+0.0162}_{-0.2242}$
RL	$-0.0100^{+0.0162}_{-0.2242}$
VV	$-0.0077^{+0.0045}_{-0.0037}$
AA	$-0.0095^{+0.0058}_{-0.0040}$
V0	$-0.0121^{+0.0054}_{-0.0056}$
A0	$-0.0049^{+0.0080}_{-0.0072}$
LL-RR	$-0.0156^{+0.0296}_{-0.0255}$

Table 8.2: Fitted values of ϵ. The values are in agreement with the hypothesis of no contact interactions ($\epsilon = 0$).

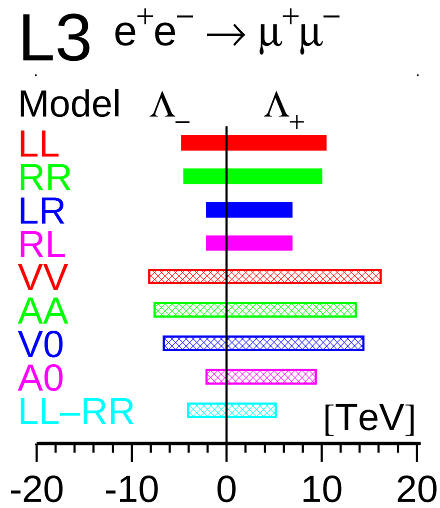

Figure 8.1: One-sided 95% confidence level lower limits on the scales Λ_+ and Λ_- for contact interactions for dimuon pairs. The plot shows the L3 results from all the LEP energy points above 130 GeV combined together.

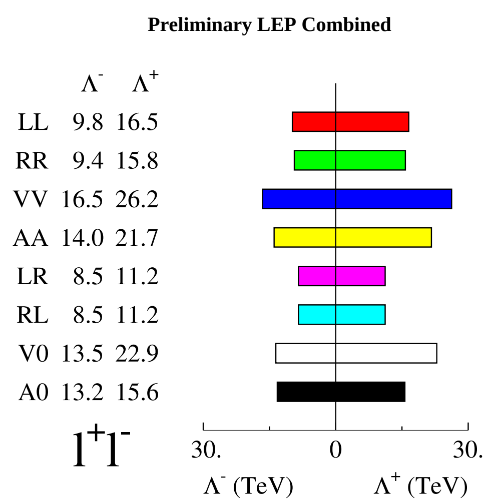

Figure 8.2: One-sided 95% confidence level lower limits on the scales Λ_+ and Λ_- for contact interactions for $e^+e^- \to l^+l^-$, assuming lepton universality. The plot shows the result from the combination of all the LEP experiments and cms energies above 130 GeV.

Chapter 9

Conclusion

The experimental results and the experimental techniques on the measurements of the interaction $e^+e^- \rightarrow \mu^+\mu^-(\gamma)$ have been presented, for center-of-mass energies ranging from 189 GeV up to $\sim$ 208 GeV. The measurements of the cross sections and forward/backward asymmetries have been discussed for 8 different energy points. All measurements are in good agreement with the theoretical predictions coming from the Standard Model. These results improve the previous tests performed with LEP data coming from $\sqrt{s} < 189$ GeV and add more significance to the agreement between the experimental data and the Standard Model. These high precision measurements can be improved only on leptonic machines. Therefore, to obtain more precise results, at higher energies, we have to wait for the next-generation machines, like the linear colliders planned now.
The combination of all the cross section and asymmetry measurements, from 130 GeV on, have then been used to search for new physics, within the framework of the contact interaction model. The dimuon L3 results have also been combined with similar searches from the other LEP experiments. No evidence of new physics has been observed.

Appendix A

Formulae

A.1 Cross section formulae

Error on ϵ_{MC}

$$\Delta\epsilon_{MC} = \frac{\sqrt{\frac{N^{sel}_{MC}\left(N^{tot}_{MC}-N^{sel}_{MC}\right)}{N^{tot}_{MC}}}}{N^{tot}_{MC}} = \frac{\sqrt{\frac{N^{sel}_{MC}N^{tot}_{MC}-N^{sel^2}_{MC}}{N^{tot}_{MC}}}}{N^{tot}_{MC}} = \sqrt{\frac{\frac{N^{sel}_{MC}N^{tot}_{MC}-N^{sel^2}_{MC}}{N^{tot^2}_{MC}}}{N^{tot}_{MC}}}$$
$$= \sqrt{\frac{\frac{N^{sel}_{MC}}{N^{tot}_{MC}} - \frac{N^{sel^2}_{MC}}{N^{tot^2}_{MC}}}{N^{tot}_{MC}}} = \sqrt{\frac{\epsilon_{MC} - \epsilon^2_{\mathrm{MC}}}{N^{tot}_{MC}}} = \sqrt{\frac{\epsilon_{MC}\left(1-\epsilon_{MC}\right)}{N^{tot}_{MC}}} \quad (A.1)$$

Number of background events and error on N^{bkg}

$$N^{bkg}_i = N^{bkg-sel}_i\ f^{MCscal}_i = N^{bkg-sel}_i \frac{\mathcal{L}}{\mathcal{L}_{MC}} = N^{bkg-sel}_i \frac{\mathcal{L}}{\frac{N^{bkg-gen}_i}{\sigma^{MC}}} = N^{bkg-sel}_i \frac{\mathcal{L}\sigma^{MC}}{N^{bkg-gen}_i} \quad (A.2)$$

$$\Delta N^{bkg}_i = N^{gen}_{MC} \times \frac{\sqrt{\frac{N^{bkg-sel}_i\left(N^{gen}_{MC}-N^{bkg-sel}_i\right)}{N^{gen}_{MC}}}}{N^{gen}_{MC}} = \sqrt{\frac{N^{bkg-sel}_i\left(N^{gen}_{MC}-N^{bkg-sel}_i\right)}{N^{gen}_{MC}}} \quad (A.3)$$

Number of Cosmics, N_{cosmic}, and ΔN_{cosmic}

$$N_{cosmic} = \frac{\frac{N^{SCN}_{cos}}{\Delta N^{SCN^2}_{cos}} + \frac{N^{DCA}_{cos}}{\Delta N^{DCA^2}_{cos}}}{\frac{1}{\Delta N^{SCN^2}_{cos}} + \frac{1}{\Delta N^{DCA^2}_{cos}}} \quad (A.4)$$

$$\Delta N_{cosmic} = \sqrt{\frac{1}{\frac{1}{\Delta N_{cos}^{SCN^2}} + \frac{1}{\Delta N_{cos}^{DCA^2}}}} \tag{A.5}$$

Error on ϵ^{ISR}

$$\begin{aligned}\Delta\epsilon^{ISR} &= \frac{\sqrt{\frac{N_{ISR}^{sel}\left(N_{MC}^{sel}-N_{ISR}^{sel}\right)}{N_{MC}^{sel}}}}{N_{MC}^{sel}} = \frac{\sqrt{\frac{N_{ISR}^{sel}N_{MC}^{sel}-N_{MCisr}^{sel^2}}{N_{MC}^{sel}}}}{N_{MC}^{sel}} = \sqrt{\frac{\frac{N_{ISR}^{sel}N_{MC}^{sel}-N_{MCisr}^{sel^2}}{N_{MC}^{sel^2}}}{N_{MC}^{sel}}} \\ &= \sqrt{\frac{\frac{N_{ISR}^{sel}}{N_{MC}^{sel}} - \frac{N_{MCisr}^{sel^2}}{N_{MC}^{sel^2}}}{N_{MC}^{sel}}} = \sqrt{\frac{\epsilon^{ISR} - \epsilon_{\mathrm{isr}}^2}{N_{MC}^{sel}}} = \sqrt{\frac{\epsilon^{ISR}\left(1-\epsilon^{ISR}\right)}{N_{MC}^{sel}}}\end{aligned} \tag{A.6}$$

Error on N_{ISR}^{bkg}

$$\begin{aligned}\Delta N_{ISR}^{bkg} &= \sqrt{\left|\frac{\partial N_{ISR}^{bkg}}{\partial\epsilon^{ISR}}\Delta\epsilon^{ISR}\right|^2 + \left|\frac{\partial N_{ISR}^{bkg}}{\partial N_{data}^{sig}}\Delta N_{data}^{sig}\right|^2} \\ &= \sqrt{\left|N_{data}^{sig}\Delta\epsilon^{ISR}\right|^2 + \left|\epsilon^{ISR}\Delta N_{data}^{sig}\right|^2} = \sqrt{N_{data}^{sig^2}\Delta\epsilon_{\mathrm{isr}}^2 + \epsilon_{\mathrm{isr}}^2\Delta N_{data}^{sig^2}}\end{aligned} \tag{A.7}$$

Systematic error contributions

In this section the formula for the calculation of the systematic errors on the cross section arising from the cut variation, background subtraction, Monte Carlo efficiency, trigger efficiency and luminosity measurements are shown.

$$\Delta\sigma_{cuts}^{syst} = \sigma \times \Delta C^{var}\ [\%] \tag{A.8}$$

$$\Delta C^{var} = \sqrt{\Delta C_{ASRC}^{var\ 2} + \Delta C_{\xi_{MM}}^{var\ 2} + \Delta C_{\xi_{MX}}^{var\ 2} + \Delta C_{P_{max}}^{var\ 2} + \Delta C_{cos\theta}^{var\ 2}} \tag{A.9}$$

$$\begin{aligned}\Delta\sigma_{bkg}^{syst} &= \sqrt{\left(\frac{\partial\sigma}{\partial N^{bkg}}\Delta N^{bkg}\right)^2} = \sqrt{\left(\frac{1}{\mathcal{L}\epsilon_{MC}\epsilon_{trig}}\Delta N^{bkg}\right)^2} \\ &= \frac{\Delta N^{bkg}}{\mathcal{L}\epsilon_{MC}\epsilon_{trig}}\end{aligned} \tag{A.10}$$

$$\begin{aligned}\Delta\sigma_{MCeff}^{syst} &= \sqrt{\left(\frac{\partial\sigma}{\partial\epsilon_{MC}}\Delta\epsilon_{MC}\right)^2} = \sqrt{\left(\frac{N_{data}^{sig}}{\mathcal{L}\epsilon_{\mathrm{MC}}^2\epsilon_{trig}}\Delta\epsilon_{MC}\right)^2} \\ &= \frac{N_{data}^{sig}\Delta\epsilon_{MC}}{\mathcal{L}\epsilon_{\mathrm{MC}}^2\epsilon_{trig}} = \sigma\frac{\Delta\epsilon_{MC}}{\epsilon_{MC}}\end{aligned} \tag{A.11}$$

$$\begin{aligned}\Delta\sigma^{syst}_{TReff} &= \sqrt{\left(\frac{\partial\sigma}{\partial\epsilon_{trig}}\Delta\epsilon_{trig}\right)^2} = \sqrt{\left(\frac{N^{sig}_{data}}{\mathcal{L}{\epsilon_{trig}}^2\epsilon_{trig}}\Delta\epsilon_{trig}\right)^2} \\ &= \frac{N^{sig}_{data}\Delta\epsilon_{trig}}{\mathcal{L}\epsilon_{MC}{\epsilon_{trig}}^2} = \sigma\frac{\Delta\epsilon_{trig}}{\epsilon_{trig}}\end{aligned} \tag{A.12}$$

$$\begin{aligned}\Delta\sigma^{syst}_{lumi} &= \sqrt{\left(\frac{\partial\sigma}{\partial\mathcal{L}}\Delta\mathcal{L}\right)^2} = \sqrt{\left(\frac{N^{sig}_{data}}{\mathcal{L}^2\epsilon_{MC}\epsilon_{trig}}\Delta\mathcal{L}\right)^2} \\ &= \frac{N^{sig}_{data}\Delta\mathcal{L}}{\mathcal{L}^2\epsilon_{MC}\epsilon_{trig}} = \sigma\frac{\Delta\mathcal{L}}{\mathcal{L}}\end{aligned} \tag{A.13}$$

A.2 Formulae for A_{fb} measurement

Error on $P_{\rm cc}$

$$\Delta P_{\rm cc} = \frac{\sqrt{\frac{N_i^{cc}\left(N^{all}-N_i^{cc}\right)}{N^{all}}}}{N^{all}} \tag{A.14}$$

Error on κ

$$\begin{aligned}\Delta\kappa &= \sqrt{\left|\frac{\partial\kappa}{\partial P_i^{cc}}\Delta P_i^{cc}\right|^2 + \left|\frac{\partial\kappa}{\partial P_j^{cc}}\Delta P_j^{cc}\right|^2} \\ &= \sqrt{\left|\frac{(P_j^{cc}-P_j^{cc2})}{(1-P_i^{cc}-P_j^{cc})^2}\Delta P_i^{cc}\right|^2 + \left|\frac{(P_i^{cc}-P_i^{cc2})}{(1-P_i^{cc}-P_j^{cc})^2}\Delta P_j^{cc}\right|^2} \\ &= \frac{1}{(1-P_i^{cc}-P_j^{cc})^2}\sqrt{\left(P_j^{cc}-P_j^{cc2}\right)^2\Delta P_i^{cc2} + \left(P_i^{cc}-P_i^{cc2}\right)^2\Delta P_j^{cc2}}\end{aligned} \tag{A.15}$$

In the case that both muons of an event are from the same category, i.e. $i = j$, equation A.15 reduces to:

$$\begin{aligned}\Delta\kappa &= \sqrt{\left|\frac{\partial\kappa}{\partial P_i^{cc}}\Delta P_i^{cc}\right|^2} = \sqrt{\left|\frac{2P_i^{cc}(1-2P_i^{cc})-(-2)P_i^{cc2}}{(1-2P_i^{cc})^2}\Delta P_i^{cc}\right|^2} \\ &= \left|\frac{2P_i^{cc}-2P_i^{cc2}}{(1-2P_i^{cc})^2}\Delta P_i^{cc}\right| = \left|\frac{2P_i^{cc2}(1-P_i^{cc})}{(1-2P_i^{cc})^2}\frac{\Delta P_i^{cc}}{P_i^{cc}}\right| = \kappa^2(1-P_i^{cc})\frac{\Delta P_i^{cc}}{P_i^{cc}}\end{aligned} \tag{A.16}$$

Error on $A_{\mathrm{fb}}^{\mathrm{isr}}$

$$\begin{aligned}
\Delta A_{\mathrm{fb}}^{\mathrm{isr}} &= \sqrt{\left|\frac{\partial A_{\mathrm{fb}}^{\mathrm{isr}}}{\partial N_{\mathrm{f}}^{\mathrm{isr}}}\Delta N_{\mathrm{f}}^{\mathrm{isr}}\right|^2 + \left|\frac{\partial A_{\mathrm{fb}}^{\mathrm{isr}}}{\partial N_{\mathrm{b}}^{\mathrm{isr}}}\Delta N_{\mathrm{b}}^{\mathrm{isr}}\right|^2} \\
&= \sqrt{\left|\frac{2N_{\mathrm{b}}^{\mathrm{isr}}}{(N_{\mathrm{f}}^{\mathrm{isr}}+N_{\mathrm{b}}^{\mathrm{isr}})^2}\Delta N_{\mathrm{f}}^{\mathrm{isr}}\right|^2 + \left|\frac{-2N_{\mathrm{f}}^{\mathrm{isr}}}{(N_{\mathrm{f}}^{\mathrm{isr}}+N_{\mathrm{b}}^{\mathrm{isr}})^2}\Delta N_{\mathrm{b}}^{\mathrm{isr}}\right|^2} \\
&= \sqrt{\frac{4N_{\mathrm{b}}^{\mathrm{isr}2}N_{\mathrm{f}}^{\mathrm{isr}}}{(N_{\mathrm{f}}^{\mathrm{isr}}+N_{\mathrm{b}}^{\mathrm{isr}})^4} + \frac{4N_{\mathrm{f}}^{\mathrm{isr}2}N_{\mathrm{b}}^{\mathrm{isr}}}{(N_{\mathrm{f}}^{\mathrm{isr}}+N_{\mathrm{b}}^{\mathrm{isr}})^4}} = \sqrt{\frac{4N_{\mathrm{b}}^{\mathrm{isr}}N_{\mathrm{f}}^{\mathrm{isr}}(N_{\mathrm{b}}^{\mathrm{isr}}+N_{\mathrm{f}}^{\mathrm{isr}})}{(N_{\mathrm{f}}^{\mathrm{isr}}+N_{\mathrm{b}}^{\mathrm{isr}})^4}} \\
&= 2\sqrt{\frac{N_{\mathrm{f}}^{\mathrm{isr}}N_{\mathrm{b}}^{\mathrm{isr}}}{(N_{\mathrm{f}}^{\mathrm{isr}}+N_{\mathrm{b}}^{\mathrm{isr}})^3}}
\end{aligned} \tag{A.17}$$

Error on A_{fb}^{BkgC}

$$\begin{aligned}
\Delta A_{fb}^{BkgC} &= \sqrt{\left|\frac{\partial A_{fb}^{BkgC}}{\partial A_{fb}^{fit}}\Delta A_{fb}^{fit}\right|^2 + \left|\frac{\partial A_{fb}^{BkgC}}{\partial(\sum_i\omega_i A_{fb}^{bkg^i})}\Delta(\textstyle\sum_i\omega_i A_{fb}^{bkg^i})\right|^2 + \left|\frac{\partial A_{fb}^{BkgC}}{\partial(\sum_i\omega_i)}\Delta(\textstyle\sum_i\omega_i)\right|^2} \\
&= \sqrt{\frac{\Delta A_{\mathrm{fb}}^{\mathrm{fit}^2}}{(1-\sum_i\omega_i)^2} + \frac{(\Delta(\sum_i\omega_i A_{fb}^{bkg^i}))^2}{(1-\sum_i\omega_i)^2} + \frac{(\sum_i\omega_i A_{fb}^{bkg^i} - A_{fb}^{fit})^2}{(1-\sum_i\omega_i)^4}(\Delta(\textstyle\sum_i\omega_i))^2}
\end{aligned} \tag{A.18}$$

with

$$\Delta(\textstyle\sum_i\omega_i A_{fb}^{bkg^i}) = \sqrt{\displaystyle\sum_i \left|\Delta(\omega_i A_{fb}^{bkg^i})\right|^2} \tag{A.19}$$

$$\begin{aligned}
\Delta(\omega_i A_{fb}^{bkg^i}) &= \sqrt{\left|\frac{\partial(\omega_i A_{fb}^{bkg^i})}{\partial\omega_i}\Delta\omega_i\right|^2 + \left|\frac{\partial(\omega_i A_{fb}^{bkg^i})}{\partial A_{fb}^{bkg^i}}\Delta A_{fb}^{bkg^i}\right|^2} \\
&= \sqrt{\left|A_{fb}^{bkg^i}\Delta\omega_i\right|^2 + \left|\omega_i\Delta A_{fb}^{bkg^i}\right|^2} \\
&= \sqrt{A_{fb}^{bkg^i\,2}\Delta\omega_i^2 + \omega_i^2\Delta A_{fb}^{bkg^i\,2}} = \omega_i A_{fb}^{bkg^i}\sqrt{\frac{\Delta\omega_i^2}{\omega_i^2} + \frac{\Delta A_{fb}^{bkg^i\,2}}{A_{fb}^{bkg^i\,2}}}
\end{aligned} \tag{A.20}$$

$$\Delta(\textstyle\sum_i\omega_i) = \sqrt{\displaystyle\sum_i |\Delta\omega_i|^2} \tag{A.21}$$

Error on C_{bkg}

$$\begin{aligned}
\Delta C_{bkg} &= \omega_{\mathrm{bkgd}} \sqrt{\left| \frac{\partial C_{bkg}}{\partial A_{fb}^{BkgC}} \Delta A_{fb}^{BkgC} \right|^2 + \left| \frac{\partial C_{bkg}}{\partial A_{fb}^{fit}} \Delta A_{fb}^{fit} \right|^2} \\
&= \omega_{\mathrm{bkgd}} \sqrt{\left| \frac{1}{A_{fb}^{fit}} \Delta A_{fb}^{BkgC} \right|^2 + \left| \frac{-A_{fb}^{BkgC}}{A_{\mathrm{fb}}^{\mathrm{fit}^2}} \Delta A_{fb}^{fit} \right|^2} \\
&= \omega_{\mathrm{bkgd}} \sqrt{\frac{\Delta A_{fb}^{BkgC^2}}{A_{\mathrm{fb}}^{\mathrm{fit}^2}} + \frac{A_{fb}^{BkgC^2} \Delta A_{\mathrm{fb}}^{\mathrm{fit}^2}}{A_{\mathrm{fb}}^{\mathrm{fit}^4}}} = \omega_{\mathrm{bkgd}} C_{bkg} \sqrt{\frac{\Delta A_{fb}^{BkgC^2}}{A_{fb}^{BkgC^2}} + \frac{\Delta A_{\mathrm{fb}}^{\mathrm{fit}^2}}{A_{\mathrm{fb}}^{\mathrm{fit}^2}}}
\end{aligned} \tag{A.22}$$

Appendix B

Differential cross sections

$cos\theta$ range	188.6 GeV [pb]	191.6 GeV [pb]	195.5 GeV [pb]	199.6 GeV [pb]
$-0.9 < cos\theta < -0.8$	0.330 ± 0.080	0.000 ± 0.169	0.427 ± 0.121	0.247 ± 0.106
$-0.8 < cos\theta < -0.7$	0.236 ± 0.052	0.187 ± 0.112	0.234 ± 0.064	0.264 ± 0.080
$-0.7 < cos\theta < -0.6$	0.317 ± 0.054	0.053 ± 0.082	0.162 ± 0.059	0.290 ± 0.076
$-0.6 < cos\theta < -0.5$	0.205 ± 0.043	0.012 ± 0.063	0.235 ± 0.073	0.184 ± 0.067
$-0.5 < cos\theta < -0.4$	0.280 ± 0.050	0.184 ± 0.097	0.130 ± 0.051	0.196 ± 0.061
$-0.4 < cos\theta < -0.3$	0.226 ± 0.047	0.293 ± 0.125	0.258 ± 0.069	0.349 ± 0.085
$-0.3 < cos\theta < -0.2$	0.166 ± 0.045	0.096 ± 0.076	0.126 ± 0.057	0.134 ± 0.053
$-0.2 < cos\theta < -0.1$	0.199 ± 0.050	0.283 ± 0.152	0.237 ± 0.072	0.244 ± 0.072
$-0.1 < cos\theta < 0.0$	0.248 ± 0.059	0.107 ± 0.116	0.040 ± 0.063	0.355 ± 0.115
$0.0 < cos\theta < 0.1$	0.211 ± 0.056	0.357 ± 0.176	0.223 ± 0.089	0.185 ± 0.080
$0.1 < cos\theta < 0.2$	0.374 ± 0.062	0.237 ± 0.122	0.214 ± 0.080	0.212 ± 0.074
$0.2 < cos\theta < 0.3$	0.356 ± 0.063	0.476 ± 0.175	0.268 ± 0.091	0.231 ± 0.081
$0.3 < cos\theta < 0.4$	0.324 ± 0.062	0.383 ± 0.141	0.450 ± 0.104	0.271 ± 0.083
$0.4 < cos\theta < 0.5$	0.330 ± 0.059	0.643 ± 0.189	0.470 ± 0.104	0.393 ± 0.097
$0.5 < cos\theta < 0.6$	0.379 ± 0.062	0.324 ± 0.142	0.286 ± 0.085	0.417 ± 0.107
$0.6 < cos\theta < 0.7$	0.563 ± 0.075	0.148 ± 0.125	0.313 ± 0.092	0.300 ± 0.097
$0.7 < cos\theta < 0.8$	0.427 ± 0.075	0.273 ± 0.161	0.456 ± 0.120	0.478 ± 0.123
$0.8 < cos\theta < 0.9$	0.476 ± 0.099	0.613 ± 0.229	0.486 ± 0.151	0.647 ± 0.164

Table B.1: Inclusive sample differential cross sections for $188.6 < \sqrt{s} < 200$ GeV. The values, in pb, for the various energy points are listed in bins of $\Delta cos\theta = 0.1$ in the range $|cos\theta| < 0.9$.

$cos\theta$ range	201.9 GeV [pb]	205.0 GeV [pb]	206.5 GeV [pb]	208.0 GeV [pb]
$-0.9 < cos\theta < -0.8$	0.128 ± 0.128	0.416 ± 0.109	0.207 ± 0.068	0.408 ± 0.312
$-0.8 < cos\theta < -0.7$	0.188 ± 0.082	0.263 ± 0.071	0.187 ± 0.045	0.444 ± 0.272
$-0.7 < cos\theta < -0.6$	0.147 ± 0.081	0.154 ± 0.061	0.207 ± 0.050	0.291 ± 0.224
$-0.6 < cos\theta < -0.5$	0.259 ± 0.105	0.209 ± 0.067	0.160 ± 0.046	0.146 ± 0.159
$-0.5 < cos\theta < -0.4$	0.099 ± 0.065	0.183 ± 0.071	0.088 ± 0.039	0.094 ± 0.180
$-0.4 < cos\theta < -0.3$	0.207 ± 0.087	0.216 ± 0.071	0.167 ± 0.050	0.299 ± 0.231
$-0.3 < cos\theta < -0.2$	0.112 ± 0.078	0.207 ± 0.066	0.110 ± 0.042	0.000 ± 0.000
$-0.2 < cos\theta < -0.1$	0.257 ± 0.100	0.241 ± 0.079	0.118 ± 0.049	0.116 ± 0.231
$-0.1 < cos\theta < 0.0$	0.344 ± 0.174	0.227 ± 0.091	0.295 ± 0.072	0.174 ± 0.235
$0.0 < cos\theta < 0.1$	0.569 ± 0.231	0.235 ± 0.088	0.186 ± 0.056	0.400 ± 0.337
$0.1 < cos\theta < 0.2$	0.235 ± 0.131	0.239 ± 0.090	0.130 ± 0.059	0.066 ± 0.228
$0.2 < cos\theta < 0.3$	0.366 ± 0.138	0.376 ± 0.093	0.188 ± 0.057	0.442 ± 0.305
$0.3 < cos\theta < 0.4$	0.435 ± 0.135	0.109 ± 0.065	0.202 ± 0.061	0.677 ± 0.375
$0.4 < cos\theta < 0.5$	0.319 ± 0.126	0.438 ± 0.103	0.282 ± 0.067	0.237 ± 0.245
$0.5 < cos\theta < 0.6$	0.378 ± 0.140	0.226 ± 0.083	0.233 ± 0.064	0.217 ± 0.227
$0.6 < cos\theta < 0.7$	0.388 ± 0.137	0.246 ± 0.085	0.444 ± 0.081	0.283 ± 0.274
$0.7 < cos\theta < 0.8$	0.262 ± 0.149	0.523 ± 0.121	0.302 ± 0.079	0.735 ± 0.399
$0.8 < cos\theta < 0.9$	0.214 ± 0.190	0.432 ± 0.147	0.365 ± 0.105	0.570 ± 0.457

Table B.2: Inclusive sample differential cross sections for $\sqrt{s} > 200$ GeV. The values, in pb, for the various energy points are listed in bins of $\Delta cos\theta = 0.1$ in the range $|cos\theta| < 0.9$.

$cos\theta$ range	188.6 GeV [pb]	191.6 GeV [pb]	195.5 GeV [pb]	199.6 GeV [pb]
$-0.9 < cos\theta < -0.8$	0.045 ± 0.035	0.029 ± 0.077	0.126 ± 0.056	0.106 ± 0.045
$-0.8 < cos\theta < -0.7$	0.008 ± 0.020	0.017 ± 0.061	0.078 ± 0.036	0.032 ± 0.036
$-0.7 < cos\theta < -0.6$	0.117 ± 0.029	0.003 ± 0.016	0.072 ± 0.027	0.102 ± 0.037
$-0.6 < cos\theta < -0.5$	0.073 ± 0.022	0.000 ± 0.030	0.100 ± 0.043	0.083 ± 0.034
$-0.5 < cos\theta < -0.4$	0.069 ± 0.022	0.092 ± 0.056	0.060 ± 0.028	0.068 ± 0.033
$-0.4 < cos\theta < -0.3$	0.092 ± 0.026	0.177 ± 0.087	0.107 ± 0.040	0.176 ± 0.056
$-0.3 < cos\theta < -0.2$	0.066 ± 0.022	0.052 ± 0.044	0.041 ± 0.027	0.045 ± 0.028
$-0.2 < cos\theta < -0.1$	0.061 ± 0.022	0.045 ± 0.047	0.074 ± 0.035	0.115 ± 0.045
$-0.1 < cos\theta < 0.0$	0.069 ± 0.029	0.052 ± 0.067	0.086 ± 0.045	0.224 ± 0.082
$0.0 < cos\theta < 0.1$	0.129 ± 0.040	0.298 ± 0.153	0.067 ± 0.044	0.123 ± 0.055
$0.1 < cos\theta < 0.2$	0.188 ± 0.039	0.112 ± 0.079	0.094 ± 0.045	0.108 ± 0.048
$0.2 < cos\theta < 0.3$	0.187 ± 0.040	0.238 ± 0.113	0.229 ± 0.068	0.091 ± 0.046
$0.3 < cos\theta < 0.4$	0.142 ± 0.039	0.233 ± 0.106	0.232 ± 0.070	0.111 ± 0.052
$0.4 < cos\theta < 0.5$	0.178 ± 0.041	0.154 ± 0.098	0.242 ± 0.073	0.232 ± 0.074
$0.5 < cos\theta < 0.6$	0.186 ± 0.044	0.178 ± 0.105	0.194 ± 0.068	0.241 ± 0.076
$0.6 < cos\theta < 0.7$	0.223 ± 0.049	0.000 ± 0.079	0.258 ± 0.079	0.175 ± 0.077
$0.7 < cos\theta < 0.8$	0.147 ± 0.049	0.000 ± 0.091	0.144 ± 0.086	0.193 ± 0.087
$0.8 < cos\theta < 0.9$	0.154 ± 0.065	0.108 ± 0.145	0.133 ± 0.090	0.268 ± 0.115

Table B.3: Non-radiative sample differential cross sections for $188.6 < \sqrt{s} < 200$ GeV. The values in pb for the various energy points are listed.

$cos\theta$ range	201.9 GeV [pb]	205.0 GeV [pb]	206.5 GeV [pb]	208.0 GeV [pb]
$-0.9 < cos\theta < -0.8$	0.086 ± 0.081	0.047 ± 0.033	0.061 ± 0.027	0.269 ± 0.213
$-0.8 < cos\theta < -0.7$	0.074 ± 0.045	0.108 ± 0.037	0.038 ± 0.021	0.004 ± 0.046
$-0.7 < cos\theta < -0.6$	0.076 ± 0.041	0.023 ± 0.026	0.067 ± 0.025	0.012 ± 0.045
$-0.6 < cos\theta < -0.5$	0.136 ± 0.066	0.058 ± 0.026	0.043 ± 0.018	0.010 ± 0.026
$-0.5 < cos\theta < -0.4$	0.067 ± 0.042	0.079 ± 0.034	0.048 ± 0.021	0.010 ± 0.021
$-0.4 < cos\theta < -0.3$	0.064 ± 0.043	0.069 ± 0.030	0.076 ± 0.025	0.012 ± 0.019
$-0.3 < cos\theta < -0.2$	0.067 ± 0.044	0.112 ± 0.039	0.051 ± 0.022	0.007 ± 0.025
$-0.2 < cos\theta < -0.1$	0.091 ± 0.051	0.086 ± 0.036	0.097 ± 0.029	0.139 ± 0.140
$-0.1 < cos\theta < 0.0$	0.213 ± 0.106	0.072 ± 0.042	0.061 ± 0.029	0.000 ± 0.028
$0.0 < cos\theta < 0.1$	0.267 ± 0.121	0.149 ± 0.055	0.078 ± 0.029	0.000 ± 0.000
$0.1 < cos\theta < 0.2$	0.093 ± 0.060	0.107 ± 0.045	0.071 ± 0.030	0.103 ± 0.143
$0.2 < cos\theta < 0.3$	0.203 ± 0.085	0.144 ± 0.052	0.104 ± 0.037	0.107 ± 0.137
$0.3 < cos\theta < 0.4$	0.300 ± 0.106	0.063 ± 0.042	0.124 ± 0.040	0.097 ± 0.139
$0.4 < cos\theta < 0.5$	0.096 ± 0.072	0.231 ± 0.065	0.161 ± 0.046	0.085 ± 0.136
$0.5 < cos\theta < 0.6$	0.229 ± 0.100	0.095 ± 0.055	0.064 ± 0.039	0.000 ± 0.000
$0.6 < cos\theta < 0.7$	0.223 ± 0.103	0.110 ± 0.056	0.239 ± 0.058	0.009 ± 0.144
$0.7 < cos\theta < 0.8$	0.066 ± 0.108	0.183 ± 0.075	0.088 ± 0.053	0.364 ± 0.275
$0.8 < cos\theta < 0.9$	0.000 ± 0.105	0.005 ± 0.071	0.088 ± 0.063	0.521 ± 0.354

Table B.4: Non-radiative sample differential cross sections for $\sqrt{s} > 200$ GeV. The values in pb for the various energy points are listed.

Appendix C

Central Error Analyzer

The *Central Error Analyzer* (*CEA*) is a software which is able to handle error conditions. It has been developed by A. De Salvo, M. Della Volpe and C. Luci for the Data Acquisition System (DAQ) of the L3 experiment. Its open architecture makes it suitable to be used in a wide variety of fields and applications/experiments.
The system has a client-server structure and is able to receive error messages from any number of processes and/or machines via a TCP/IP channel. All the error messages received are collected in a database (*Postgresql*), providing a centralization and chronological tracking of all the error situations of a given complex system.
For each error situation the CEA reacts taking actions in order to find a solution to the problem encountered: this is done by using the informations written into the database, using them as a "historical memory of experience".
The architecture of the Central Error Analyzer is completely modular, flexible and easy manageable, since it is based on a relational database running on Unix (Linux) OS and taking advantage of external plugins, fully customizable by the user.
The CEA is completely written in C/C++, with fortran callable functions (to interface with the existing software in the L3 online pool) while the exec modules may be written in several languages as C/C++, perl, shell, etc. The network protocol used is based on the standard TCP/IP IPv4, taking advantage of the standard Unix services. For the L3 experiment in particular, however, the remote execution of VAX programs has been chosen to be done via a custom emulation of rshell, providing more flexibility, security and execution speed with respect to the OpenVMS version of rshell. The CEA kernel uses the Postgresql v6.3 or higher on a Unix machine. The user interface is fully graphical and based on the X11 standard, via the Qt library.
The system has been used in L3, in beta test in 1998 and fully operational in 1999 and 2000, running on an Intel Pentium II (Linux Os version 5.1). Its use allowed to improve the data taking stability by up to 30%, and the DAQ efficiency by up to 2% [26] ($\sim$ 89% in 1998 and $\sim$ 91% in 2000), since several actions have been automatically taken in a few milliseconds and, in case of failure, the experts were informed tempestively on the problem. During three years of use, more than 20000 messages have been collected by the CEA, coming from almost all the subdetectors: this has permitted also to improve the checks on several parts of the apparatus, looking at the frequence of some recurring error topologies.

C.1 The Central Error Analyzer architecture

The Central Error Analizer is made out of several tasks on the server side and on the client side. On the server they are called CEA Server, CEA Main, CEA Manager, CEA Watcher and all the CEA Exec Modules (plugins). The database is supervised by the Postmaster who takes care of the backend managing. On the clients a generic module call S2C (Send To CEA) for generic message passing and a library (Cealib) to embed the CEA message passing into the programs are available. A program called L3_CEA_PC is also provided to easily interact via a console from a client to the server. In figure C.1 a pictorial view of the CEA architecture used in L3 is shown. In the following sections the different subsystems will be explained in detail.

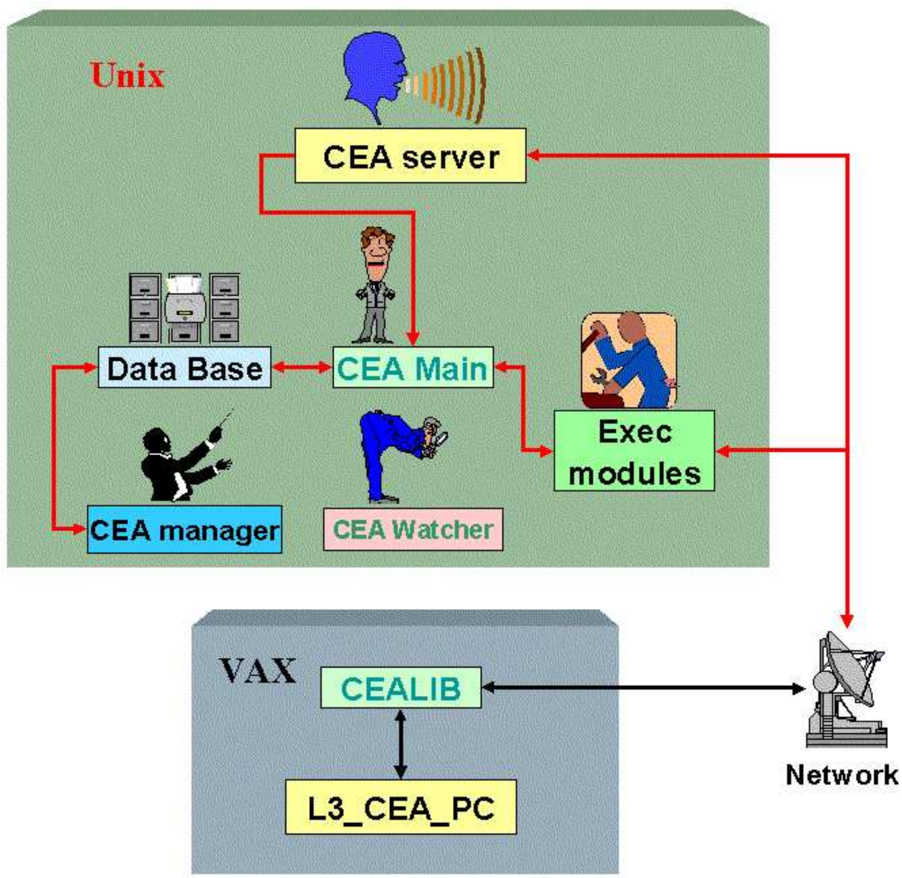

Figure C.1: The Central Error Analyzer architecture. The CEA Server, CEA Main, CEA Manager, CEA Watcher and CEA clients logical interactions are shown. The figure shows the main situation in the L3 experiment, where almost all the clients were running on VAX (OpenVMS) and the server on Unix (Linux).

C.1.1 CEA Server

This process is the main interface with the network and the clients. It waits for incoming TCP/IP connections coming from remote processes (like from the Cealib). When an message is received it is written on disk and the CEA Main is informed of it via a local IPC message queue ($\sim$ 16 Kb). The server can also act as a reflector to bounce data to another machine: an example in L3 is a START or STOP command coming from the VAX online cluster that has been sent to another process running on another machine, like a reconstruction program running online. The CEA server runs in background as a demon and has no access to the database.

C.1.2 CEA Main

This is the CEA main task. It has access to both the database and the messages coming from the network via the server. It reads the database tree structure at startup and creates the so called *CEA tree*. Then it waits for an event, which can be a message from a client, a service request coming from the graphical user interface a DB managing or command execution cancelling request.
When the CEA main is informed of an incoming message it gets the informations on it, stored on disk by the server, and looks into the database to find if it is a known error. If the answer is positive it updates the log table and finds out from the database which is the action to take. If CEA knows which is the action to take it scans the CEA tree to reach the associated object. When it is reached the object action is executed. If the called object has children, unless specified, the actions in each child will be executed, ordered by the object order field. In this way it is possible to build a complex tree using logical operations (AND, OR) between actions. To specify a forced exit of the execution thread after a given Exec Module execution, even if there are some children left, such module must have a return code of 200. If the error is not known the CEA managing team is noticed via gsm sms and/or e-mail.
The GUI is very simple and compact. It gives access to the main operations to manage the DB, to show the commands awaing in queue and to stop a command execution (see figure C.2. A button to reload the CEA tree while running is also provided. Extra functionalities as the speaking subsystem, coupled with the IBM ViaVoice for Linux will not be covered here.

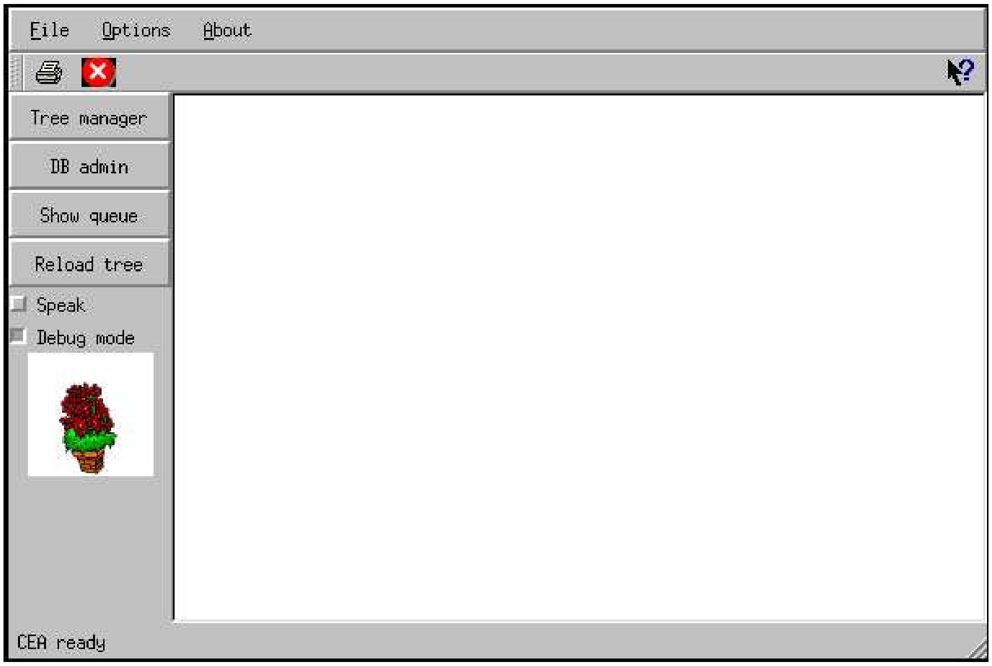

Figure C.2: The Central Error Analyzer main window.

C.1.3 CEA Manager

The CEA manager is a Graphical User Interface to access and manage the database tree structure and all the related tables in a more fashionable way. It can be also used when CEA is running, to modify the structure of the CEA tree, but all the modifications will only be applied when CEA is restarted or when the button "Reload tree" in the CEA main window is pressed. In figure C.3 the GUI is shown.
Each object is inserted via an insertion mask (see figure C.4) which provides a reliable checking on the object name duplication. Object names must be unique but one single message, identified via a message identifier number (message IDs), may be associated to several different objects. If two or more objects with similar functionalities are needed a *link* to a master object can be used. For each link the target actions can anyway be different one from each other.

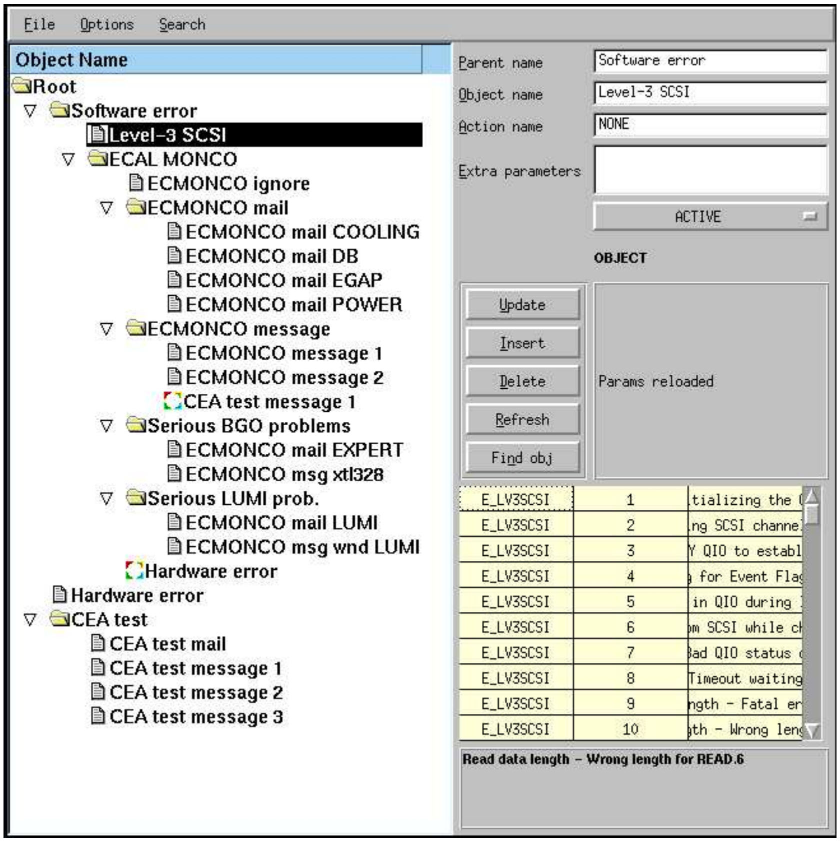

Figure C.3: The Central Error Analyzer manager user interface.

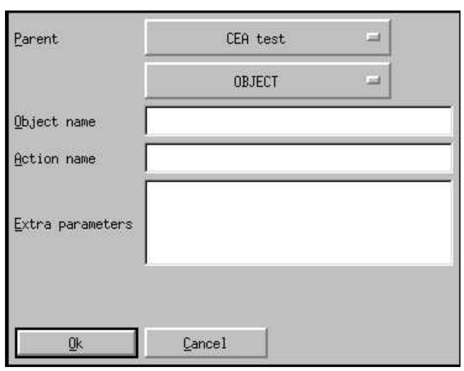

Figure C.4: The Central Error Analyzer interface to insert objects in the database. Each object must have an existing parent, listed in the first field, and an unique name.

C.1.4 CEA Watcher

This process watches the execution of all the other CEA tasks. After CEA is started the first time it stays in wait mode (*supervisor mode*), automatically restarting the processes in case of problems. If a process exits correctly (*slean exit*, return code 0) it is not restarted and no more supervised by the watcher.

C.1.5 CEA Exec Modules

Every time CEA needs to perform an action it launches one or more executable module, which actually performs the action. The executable modules are executable files (scripts, compiled programs, etc.) which have access to the informations coming from CEA, regarding the action to be performed. These modules may execute local as well as remote commands to execute the actions.
A Software Development Kit (*CEA SDK*) is available to easily create such modules.

C.2 The Central Error Analyzer database structure

The CEA database is organized in a tree structure, each item (row) having one parent and one or more children. In figure C.5 the typical database structure is shown. Starting from the top, we see the first object ("DAQ Hangs"), called *root* and the "Sw" (software) and "Hw" (hardware) items, both children of the root item. The tree then develops till the action objects (*leaves*).
The reason of this kind of structure is to make possible the association of one action or a category of them to a given error number, thus permitting CEA to solve specific problems or to tell the management team to instruct it on how to solve an unknown problem.

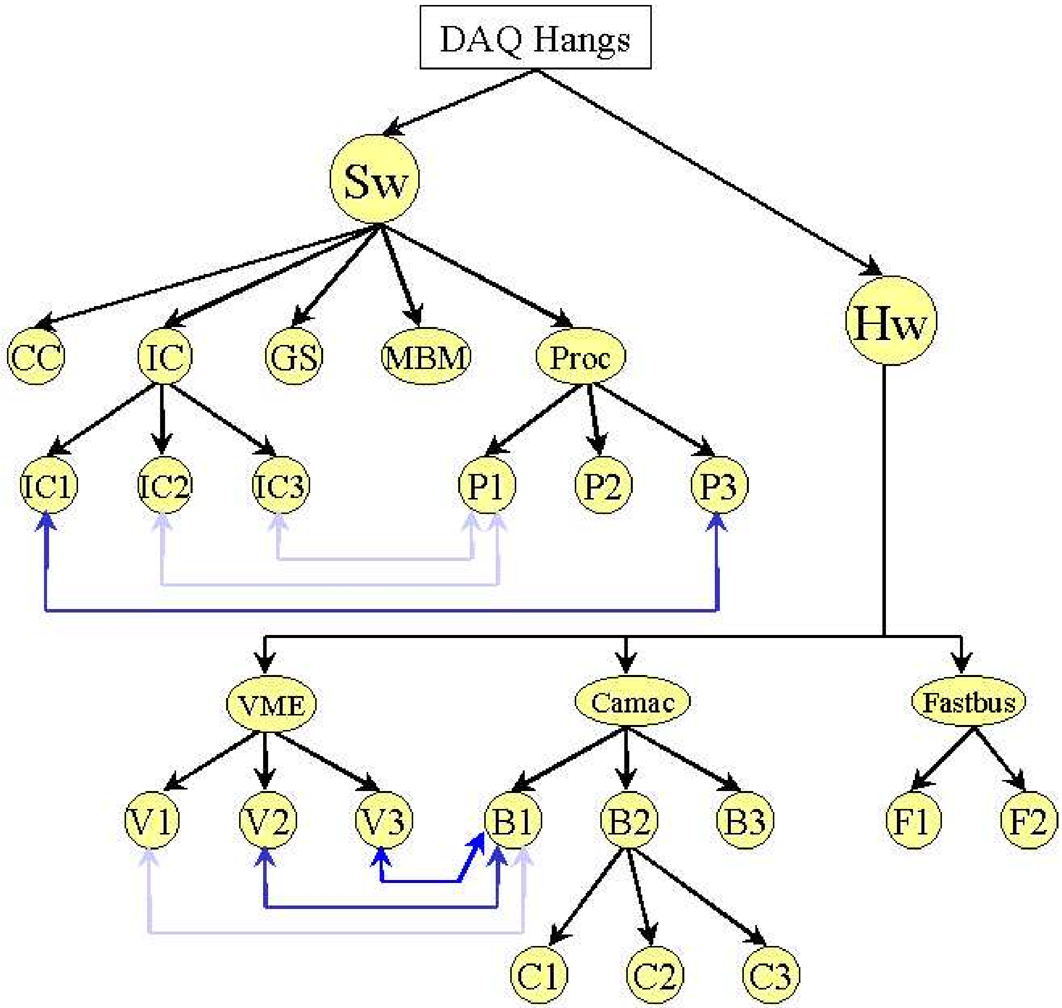

Figure C.5: The Central Error Analyzer database structure. The tree starts with the *root* item (DAQ Hangs) and then develops till the action objects or *leaves*. user interface.

To encapsulate this scheme in a relational database CEA makes use of several correlated tables:

- Tree Structure table;
- Error table;
- Log table;
- Category table.

In figure C.6 the relations among the different tables are shown, together with the key items (identified by a little key on the left). In the following paragraph an overview of all these tables is discussed.

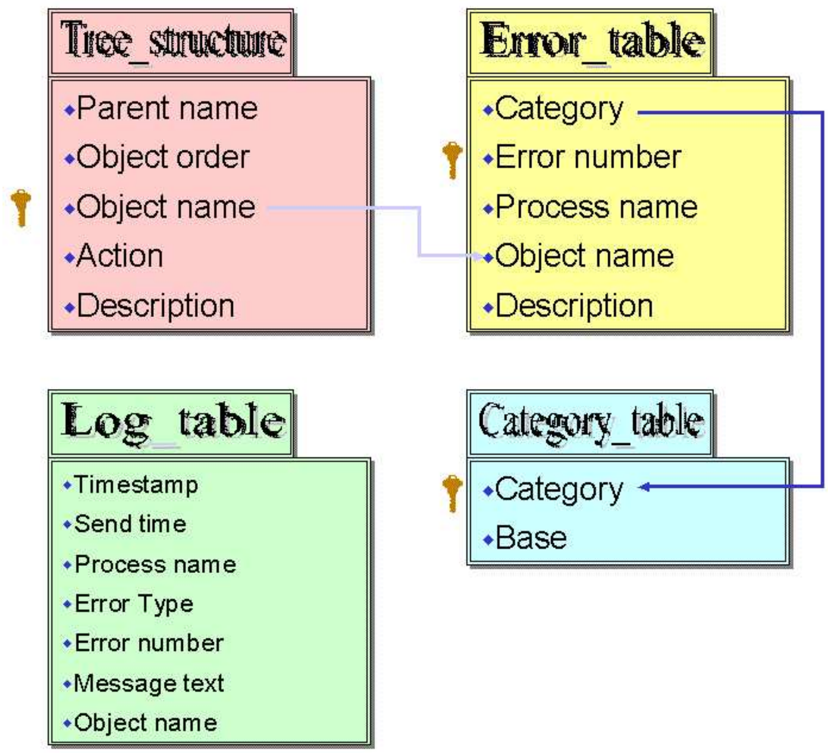

Figure C.6: The Central Error Analyzer database table structure. The different tables are shown together with their relationships. The items identified by a small key are the *key items*.

C.2.1 The Tree Structure table

In this table the entire tree structure is described, starting from the informations contained in the different fields:

- **Parent name**: the name of the parent item (max 20 chars);
- **Object order**: this numerical field is used to order the items belonging to the same parent in an order different from the alphabetical (default) one;
- **Object name**: name of the item; it must be unique (max 20 chars);
- **Action name**: action associated to this item. If it is prefixed with "ext::" CEA will execute a shell command, for example using "ext::dir" the associated action will be the shell command "dir";

- **Parameters**: additional parameters, if needed by the action command (max 255 chars);
- **Description**: description of this item;
- **Status**: numeric field; if 0 it means that this item is INACTIVE (and so skipped by CEA), while if 1 this item is ACTIVE;
- **Type**: it determines if this item is an object (0) or a LINK to an object (1);

C.2.2 The Error table

This table hold all the informations about the error numbers and the associated actions.

- **Category**: name of the category of this error, as from the Category table;
- **Error number**: numerical fields that represents the error number, spanning from 0 to 255. It must be unique;
- **Process name**: name of the process that is allowed to send this error message, if NULL every process is allowed;
- **Object name**: name of the object to call when this specific error is received, in relation to the Tree Structure table;
- **Description**: short description of this error message;

C.2.3 The Log table

All the CEA log messages are contained in a table called *Log table*. This permits a chronologic tracking of all the actions taken during the time.

- **Timestamp**: time at which the error message has been received;
- **Send time**: time at which the error message was sent via TCP/IP from the sender;
- **Process name**: name of the process that sent this message;
- **Error type**: type of the message. Can be "E" for error, "W" for warning or "A" for acknoledgement;
- **Error number**: absolute error number;
- **Message text**: text body of the error message, can be as long as 10 lines of 80 characters each;
- **Object name**: if this error is known in the database this fields is filled with the name of the item associated to this error, otherwise it is "NOT FOUND";

C.2.4 The Category table

Errors are grouped in categories. In this table the list of the different categories is described.

- **Category**: mnemonic name of the error category (max 20 chars);
- **Base**: base number for this category of errors; it is used to convert from relative error numbers within a category (0-255) to the absolute error numbers, uniques for all categories;

Appendix D

Muon barrel calibration

The muon chamber resolution depends on three parameters of the cell map:

1. v_D
   This is the drift velocity of the muons inside the gas under the effect of the applied electrical field.

2. α_L
   Due to the Lorentz force, induced by the magnetic field, the muons will drift along a path with a Lorentz angle α_L with respect to the electrical field.

3. T_0
   This is the global T_0, defined as $T_0 = T_{prop} + t_0$, where T_{prop} is measured time-of-propagation of the signals along the cables and t_0 is an adjustable constant.

The goal of the calibration process is to find a combination of these parameters which gives a better momentum resolution E_{beam}/P_{muon}. In the muon chamber barrel the resolution is parametrized in the following way:

$$\frac{E_{beam}}{P_{muon}} = \phi(v_D, \alpha_L, T_0) = a_1\delta_{v_D}\delta_{T_0} + a_2\delta_{v_D}\delta_{\alpha_L}a_3\delta_{v_D} + a_4\delta_{T_0}a_5\delta_{\alpha_L} + a_6 \tag{D.1}$$

where $\phi(v_D, \alpha_L, T_0)$ is the Taylor expansion of E_{beam}/P_{muon}. The parameters δ_{v_D}, δ_{T_0} and δ_{α_L} are the differences of the corresponding quantities v_D, T_0 and α_L from their central values $v_D^{central}$, $T_0^{central}$ and $\alpha_L^{central}$. The parameters a_k (k = 1...6) are event-dependent constants.
Formula D.1 may be rewritten in a more compact way:

$$\phi(v_D, \alpha_L, T_0) = \sum_{k=1,6} a_k f_k(v_D, \alpha_L, T_0) \tag{D.2}$$

where the f_k functions are obtained by comparison with equation D.1.
To find the best values of the parameters v_D, T_0 and α_L an analysis program has been developed. It considers three variations of each parameter: one negative variation, one positive and one at the nominal value, for a total of $N = 27$ sets of variations. A value

of E_{beam}/P_{muon} is computed for each set. The corresponding constants a_k are then calculated using a least square method:

$$a_k = \sum_{i=1,6} M^{-1}_{k,i} V_i \tag{D.3}$$

where

$$\begin{aligned} M_{k,i} &= \sum_{j=1,N} f_k(v^j_D, \alpha^j_L, T^j_0) f_i(v^j_D, \alpha^j_L, T^j_0) \\ V_i &= \sum_{j=1,N} f_i(v^j_D, \alpha^j_L, T^j_0) \left(\frac{E_{beam}}{P_{muon}}\right)_i \end{aligned} \tag{D.4}$$

and $(E_{beam}/P_{muon})_i$ is the value of E_{beam}/P_{muon} calculated for the value set i. The values of v_D, T_0 and α_L are then obtained by minimizing the resolution, estimated by $\hat{\sigma}$:

$$\hat{\sigma}(v_D, \alpha_L, T_0) = \sqrt{\sum_{i=1,M} \frac{|\phi_i(v_D, \alpha_L, T_0) - \bar{\phi}(v_D, \alpha_L, T_0)|^2}{M-1}} \tag{D.5}$$

where the sum extends over all the muons, M, $\phi_i(v_D, \alpha_L, T_0)$ is the value of $\phi(v_D, \alpha_L, T_0)$ for the muon i and $\bar{\phi}(v_D, \alpha_L, T_0)$ is the average $\phi(v_D, \alpha_L, T_0)$ for all the muons. The minimization is done using the MINUIT package.
The whole process is iterated several times, starting at first with the values of the calibration parameters obtained from the testbeam, until the best resolution is obtained. The events used for the calibration are "golden" dimuons only, coming from the Z-calibration runs ($\sim 2.5\ pb^{-1}$ of integrated luminosity each), when LEP is running at $\sqrt{s} \sim M_Z$. The "golden" dimuons are defined by the following cuts:

- **acollinearity cut**: $\xi < 1.5^\circ$ to reject radiative events;
- **ECAL energy**: the energy in the ECAL must be $E_{ECAL} < 1.5$ GeV, to reduce events with collinear photons;
- **calorimeters**: bremsstrahlung events are removed by requiring a minimum of 3.5 GeV of energy in the calorimeters;
- **calorimeters**: to reject the τ background the sum of the absolute value of the momentum of the muons is required to be greater than 60 GeV;
- **charge confusion**: charge confused events are discarded;
- **event quality**: only events with 3 segments in the P-chambers are selected (triplets).

The result of the first period of calibration for the year 2000 is shown in figure D.1, in comparison with the resolution calculated in 1991. Since the tails of the distributions are non-gaussian the fit is extended from -3σ to $+2\sigma$ around the central value. As one may note from the plots the values of the resolution remained almost unchanged during 10 years of data taking ($\sigma = 2.47 \pm 0.02$ % in 1991 and $\sigma = 2.80 \pm 0.10$ % in 2000), meaning that no apparent sign of detector ageing is present. In figure D.2 the variations of the calibration parameters with time is shown for the year 2000, in which LEP delivered 4 calibration periods. Again the stability of the parameters is very high and no degradation is visible.

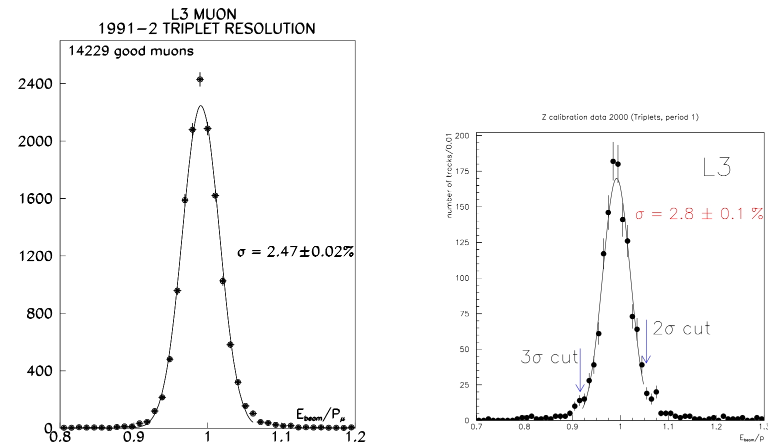

(a) (b)

Figure D.1: Muon barrel resolution in 1991 (a) and 2000 (b). The resolution remained almost unchanged during the years.

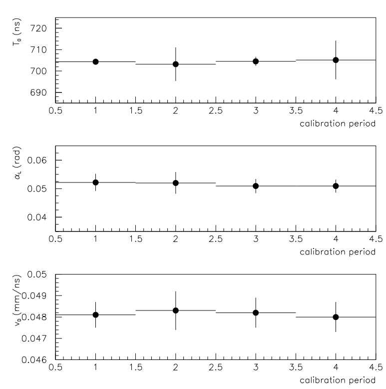

Figure D.2: Stability of the muon barrel calibration parameters for the 4 different calibration periods in 2000 (T_0, α_L, v_d, from top to bottom). All the values remained stable during all the data taking period.

Bibliography

[1] G. Arnison et al. UA1 Collab. *Phys. Rev. Lett. B*, 122:103, 1983.

[2] M. Banner et al. UA2 Collab. *Phys. Rev. Lett. B*, 122:476, 1983.

[3] ALEPH Collab. Aleph: A detector for electron-positron annihilations at lep. *Nucl. Instr. Meth. A*, 294:121, 1990.

[4] DELPHI Collab. The delphi detector at lep. *Nucl. Instr. Meth. A*, 303:233, 1990.

[5] B. Adeva et al. L3 Collab. The construction of the l3 experiment. *Nucl. Instr. Meth. A*, 289:35, 1990.

[6] OPAL Collab. The opal detector at lep. *Nucl. Instr. Meth. A*, 305:275, 1991.

[7] S.L. Glashow. *Nucl. Phys.*, 22:579, 1961.

[8] D. Bardin et al. ZFITTER 6.21. *preprint hep-ph/9908433, Z. Phys*, C(44):493, 1989.

[9] K. Lane E. Eichten and M. Peskin. *Phys. Rev. Lett.*, 50:811, 1983.

[10] M. Acciarri et al. L3 Collab. The l3 silicon microvertex detector. *Nucl. Instr. Meth. A*, 351:300–312, 1994.

[11] H. Akbari et al. L3 Collab. The l3 vertex detector: design and performance. *Nucl. Instr. Meth. A*, 315:161, 1992.

[12] O. Adriani et al. L3 Collab. Hadron calorimetry in the l3 detector. *Nucl. Instr. Meth. A*, 302:53, 1991.

[13] A. Adam et al. L3 Collab. The forward muon detector of l3. *Nucl. Instr. Meth. A*, 383:342, 1996.

[14] Y. Bertsch et al. The second level trigger of the l3 experiment. *Proc. (Mudinich, Castelli, Colavita) World Sci. Singapore*, page 56, 1988.

[15] C. Dionisi et al. The third level trigger system of the l3 experiment at lep. *Nucl. Instr. Meth. A*, 336:78, 1993.

[16] M.Hansroul R. Brun, R. Hagelberg and J.C. Lassalle. Geant: Simulation program for particle physics experiments. user guide and reference manual. *CERN-DD-78-2-REV.*

[17] I.C. Brock et al. L3 Collab. Luminosity measurement in the l3 detector at lep. *Nucl. Instr. Meth. A*, 381:236–266, 1996.

[18] B.F.L. Ward S. Jadach and Z. Was. The precision monte carlo event generator *kk* for two fermion final statesin e^+e^- collisions. *preprint CERN-TH 99-235*, 1999.

[19] P.H. Daverfeldt F.A. Berends and R. Kleiss. *Nucl. Phys. B*, 253:441, 1985.

[20] R. Kleiss J.M. Hilgart and F. Le Diberder. *Comput. Phys. Comm. 75*, page 191, 1993.

[21] J. Breitweg et al. ZEUS Collab. *E. Phys. J. C*, 2000.

[22] C. Adloff et al. H1 Collab. *preprint DESY 00-027, accepted by Phys. Lett. C.*

[23] CDF Collab. F. Abe et al. *Phys. Rev. Lett.*, 79:2198, 1997.

[24] D0 Collab. B. Abbott et al. *Phys. Rev. Lett.*, 82:4769, 1999.

[25] C. Geweniger et al. LEPEWWG $\mathrm{f\bar{f}}$ Subgroup. *preprint LEP2FF-01/02, http://lepewwg.web.cern.ch/LEPEWWG/lep2/summer2001*, 2001.

[26] C. Luci. Private communication.

Acknowledgments

In the period spent at CERN for this thesis I have learned a lot, both from the professional and the human point of view. This has been an invaluable experience of life and occasion to grow up in the fields of the physics.
I would like to thank all the people who supported me, directly or indirectly, who made possible for me to achieve the results shown in the thesis. In particular I would like to thank Dr. Klaus Freudenreich for his invaluable work and suggestions: I appreciated very much what he has done for me, in particular when the things got difficult, when we were working together from two different countries. Then I would like to thank Dr. Dimitri Bourilkov, Dr. Frank Filthaut and Dr. Stephan Wynhoff, for their very important suggestions and help. It has been a real pleasure and honor for me to work with them. Last but now least I thank ETH, and in particular in the person of Prof. Dr. Felicitas Pauss, for the possibility gave me to have a so interesting experience in the High Energy Physics at CERN.
A particular remark is due to Prof. Claudio Luci, Prof. Carlo Dionisi and Dr. Luca Malgeri, the people that have been most involved in my professional life, since my diploma thesis, and, more important, people that for me are real friends and masters of life.
A special word is then for the people who supported me remotely from Italy, in the bad and good times. In particular I would like to express my gratefulness to my parents and Maristella: I don't really know what I would have been without you and your love.
Finally I would like also to thank all the other people that has allowed me to get here and to be what I am now (a thing that can be either positive or negative, the choice is up to the reader...), but I would like to leave the last word to a little half-human being who has a special relevance in my life since its born date in August 1994: my dog LEP.